Astronomy Letters, Vol. 28, No. 6, 2002, pp. 353–365. Translated from Pis'ma v Astronomicheskiĭ Zhurnal, Vol. 28, No. 6, 2002, pp. 403–416.

A Catalog of Cosmic Gamma-Ray Bursts Detected by the PHEBUS Instrument on the Granat Observatory: October 1994–December 1996

A. Yu. Tkachenko[1*], O. V. Terekhov[1], R. A. Sunyaev[1], A. V. Kuznetsov[1], C. Barat[2], J.-P. Dezalay[2], and G. Vedrenne[2]

[1] *Space Research Institute, Russian Academy of Sciences, Profsoyuznaya ul. 84/32, Moscow, 117810 Russia*

[2] *Centre d'Etude Spatiale des Rayonnements, 9 avenue du Colonel Roche, BP 4346, 31028 Toulouse Cedex 4, France*

Received January 17, 2002

Abstract—We present the final part of the catalog of cosmic gamma-ray bursts (GRBs) observed in the PHEBUS experiment on the Granat orbiting astrophysical observatory. The first three parts of the catalog were published by Terekhov *et al.* (1994, 1995a) and Tkachenko *et al.* (1998). The fourth part contains information on 32 events recorded from October 1994 until December 1996. We give burst light curves in the energy range 100 keV to 1.6 MeV, integrated energy spectra, and information on the fluence and energy flux at the luminosity peak for energies above 100 keV. Over the entire period of its operation, the PHEBUS instrument detected 206 cosmic GRBs. The mean $\langle V/V_{\max}\rangle$ was 0.336 ± 0.007. The mean hardness corresponding to the ratio of count numbers in the energy ranges 400–1000 and 100–400 keV is 0.428 ± 0.018 for events with a duration shorter than 2 s and 0.231 ± 0.004 for events with a duration longer than 2 s. © *2002 MAIK "Nauka/Interperiodica".*

Key words: *gamma-ray bursts, catalog*

INTRODUCTION

The PHEBUS instrument was devised at the Centre d'Etude Spatiale des Rayonnements in Toulouse (France) and installed onboard the Granat orbiting astrophysical observatory, which was launched into a high-apogee orbit on December 1, 1989. The instrument was designed to study cosmic gamma-ray bursts (GRBs) and high-energy solar flares in the energy range 100 keV to 100 MeV. It consisted of six bismuth germanate (BGO) detectors surrounded by a plastic anticoincidence shield. The detectors were located on different sides of the Granat observatory. PHEBUS had successfully operated in orbit and recorded burst events until late 1996. A detailed description of the instrument and the modes of its operation can be found in Barat *et al.* (1988).

The previous parts of the catalog contain the results of the PHEBUS observations of cosmic GRBs from December 1989 until September 1994 (Terekhov *et al.* 1994, 1995a; Tkachenko *et al.* 1998). This part presents the results of the GRB observations from October 1994 until December 1996. The data reduction technique and presentation of the results are the same as those in the previous parts of the catalog. In general, the catalog structure was also preserved. Explanations on modifications are given in the text of the catalog.

THE STATISTICS OF RECORDED EVENTS

Since October 1994, the Granat observatory spent most of the time in scanning mode and PHEBUS was not switched off during its passage through the Earth's radiation belts. The number of burst events whose information could be written to the PHEBUS onboard memory was limited; therefore, such a mode of operation resulted in a reduction in the number of detected GRBs. Magnetospheric events accounted for most of the PHEBUS burst cell triggerings.

The total observing time from October 1994 until December 1996 was 164 days. Over this period, 428 PHEBUS burst cell triggerings were recorded. Only 32 of them were related to cosmic GRBs and two were related to X-ray solar flares. The light curves of some high-energy solar flares are similar to those of cosmic GRBs and their energy spectra may extend beyond a few hundred keV and, in some cases, up to several tens of MeV (Terekhov *et al.* 1995b). We selected GRBs from all of the events recorded during the experiment by using the confirmations of the events by other spaceborne observatories. Over the entire period of its operation (December 1989–December 1996), PHEBUS obtained information on 206 cosmic GRBs.

[*] E-mail: ayut@hea.iki.rssi.ru

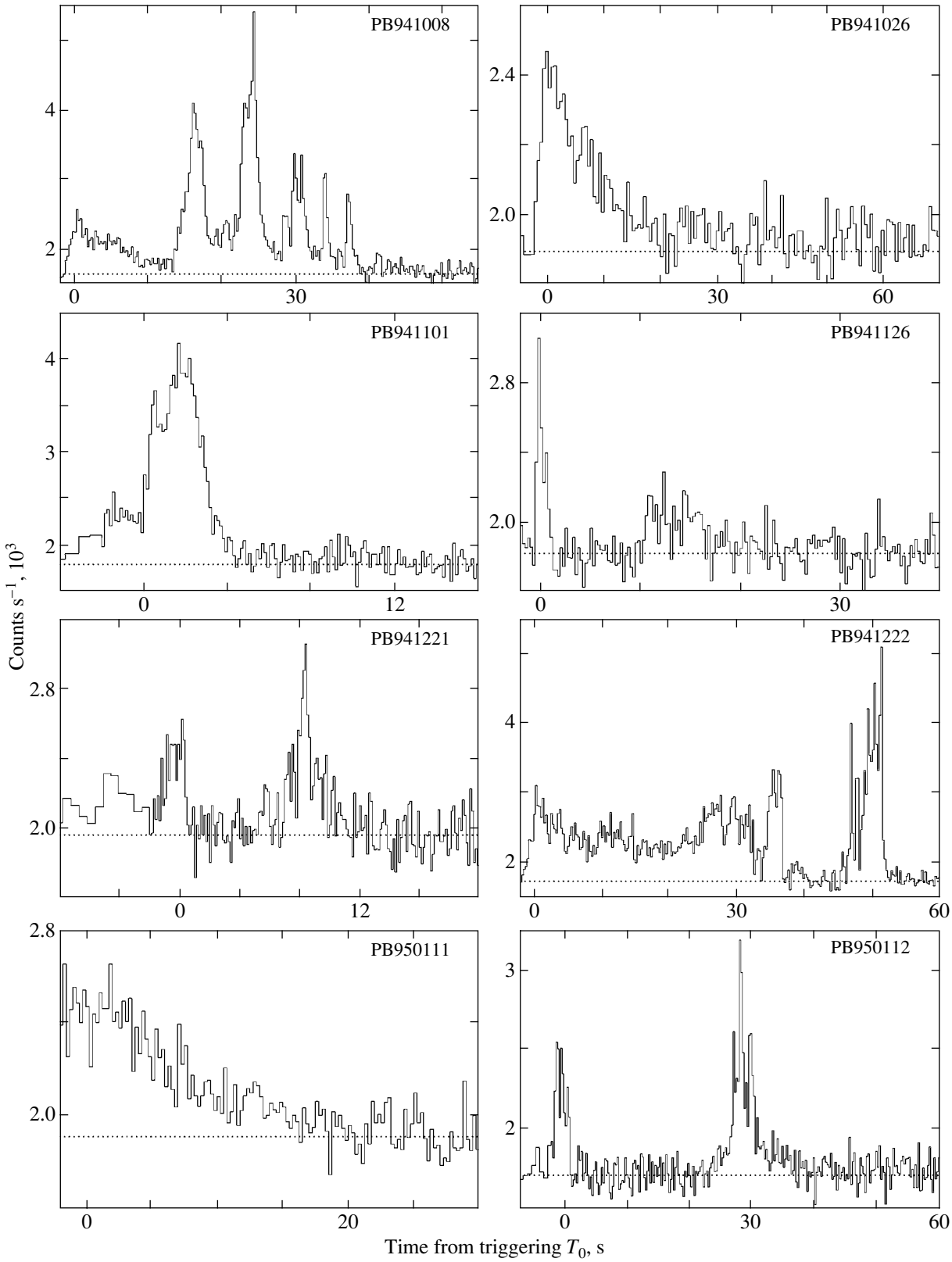

Fig. 1. Light curves of the cosmic GRBs detected by the PHEBUS instrument on the Granat observatory from October 1994 until December 1996 in the energy range 100 keV to 1.6 MeV. The dotted line indicates the PHEBUS detector background levels in a period immediately preceding the burst.

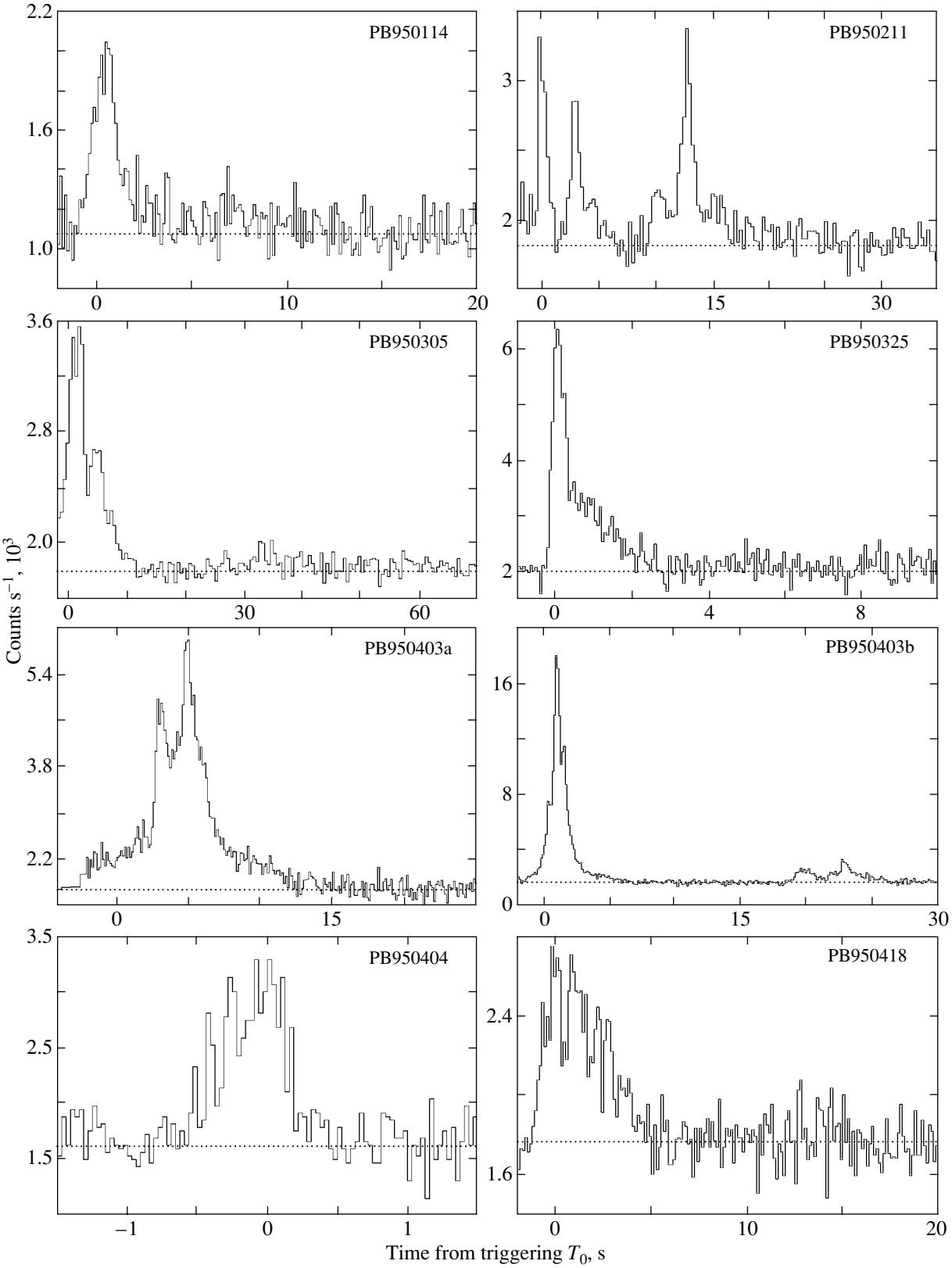
PB950114
PB950211
PB950305
PB950325
PB950403a
PB950403b
PB950404
PB950418
Counts s^{-1}, 10^3
Time from triggering T_0, s

Fig. 1. (Contd.)

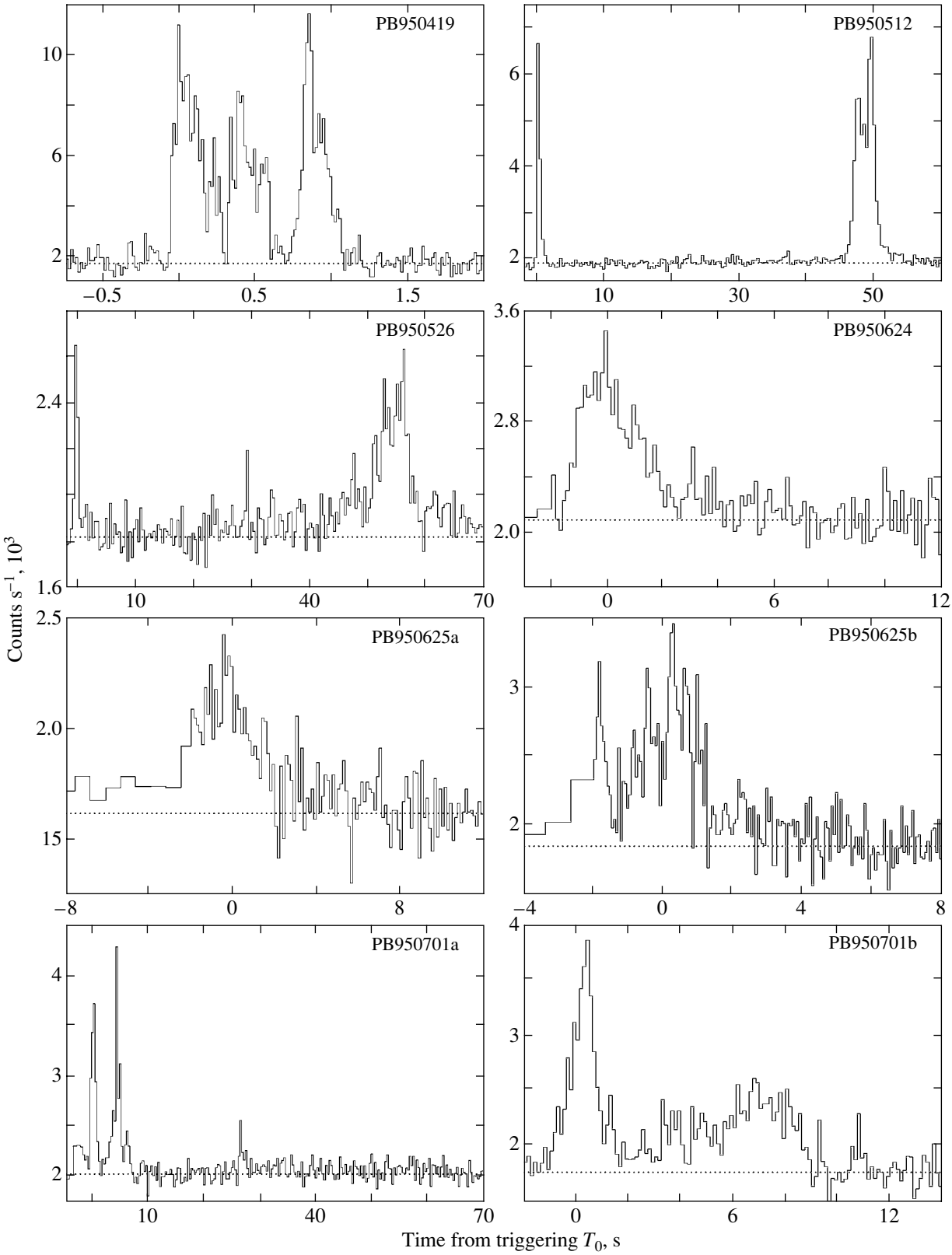
PB950419
PB950512
PB950526
PB950624
PB950625a
PB950625b
PB950701a
PB950701b
Counts s^{-1}, 10^3
Time from triggering T_0, s

Fig. 1. (Contd.)

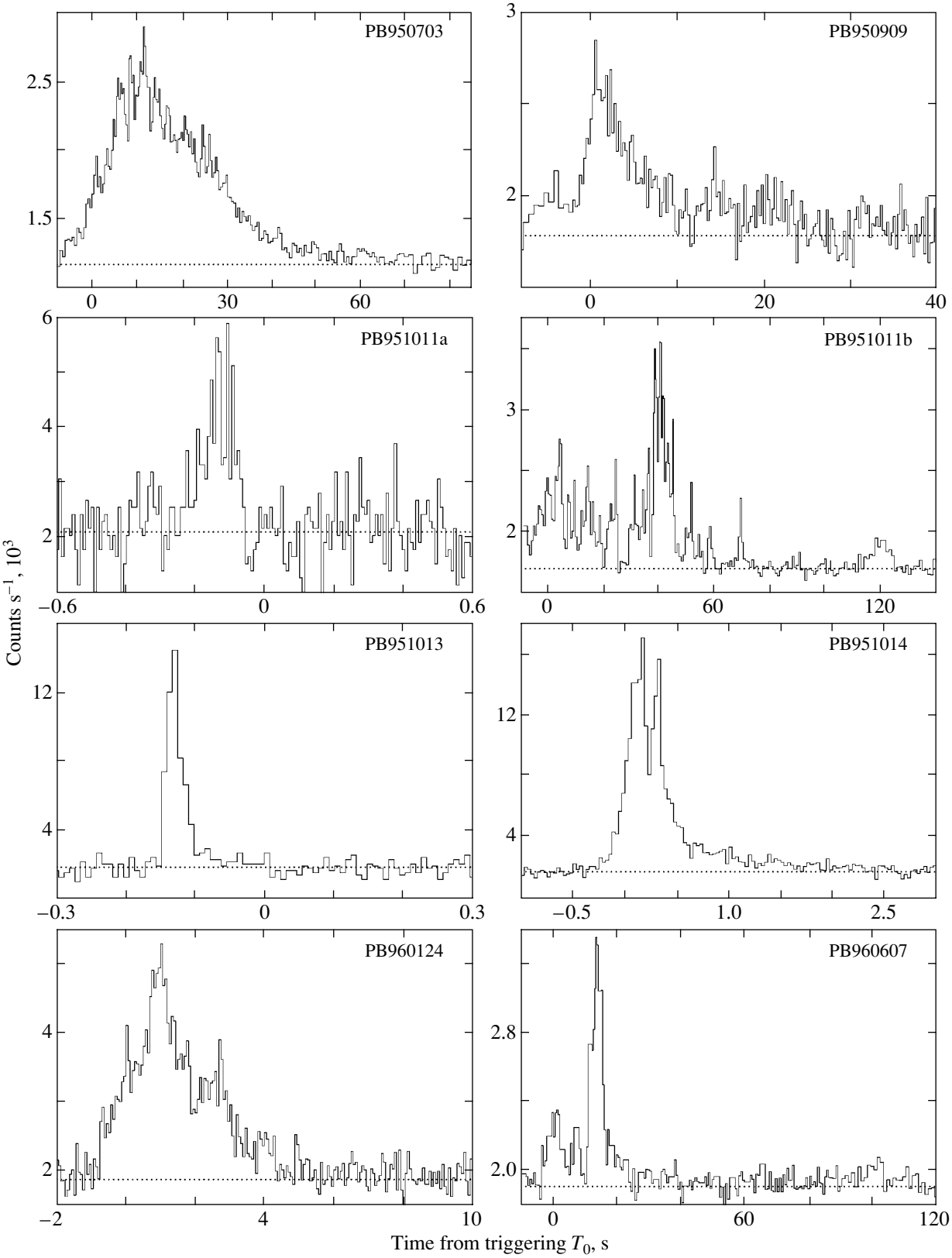
PB950703
PB950909
PB951011a
PB951011b
PB951013
PB951014
PB960124
PB960607
Counts s^{-1}, 10^3
Time from triggering T_0, s

Fig. 1. (Contd.)

Main characteristics of 32 GRBs detected by the PHEBUS instrument (October 1994–December 1996)

Burst name	Session number	Triggering time	Duration T_{90}, s	$C_{\max}/C_{\min}$	Fluence[a], 10^{-5} erg cm^{-2}	Peak flux[a], 10^{-5} erg cm^{-2} s^{-1}	Spectral hardness[b]	Anal. law	Para-meter	χ^2/DOF	Notes[c]
PB941008	805.01	$13^h34^m18^s.685$	36.19 ± 0.32	5.89 ± 0.29	16.07 ± 6.06	4.10 ± 1.80	0.26 ± 0.01	S	2.69	67.19/33	BU
PB941026	807.01	2 52 37 629	58.86 ± 1.10	1.22 ± 0.20	0.62 ± 0.24	0.31 ± 0.14	0.15 ± 0.04	S	1.32	7.17/9	B
PB941101	809.01	6 30 58 595	12.56 ± 1.26	4.70 ± 0.26	3.31 ± 1.28	1.33 ± 0.57	0.15 ± 0.01	P	−1.97	19.68/17	U
PB941126	812.01	0 20 46 130	23.13 ± 0.20	1.24 ± 0.22	1.56 ± 0.71	1.89 ± 0.90	0.60 ± 0.12	P	−1.36	3.00/8	BK
PB941221	819.01	22 14 36 608	11.40 ± 0.48	1.26 ± 0.20	0.74 ± 0.33	0.25 ± 0.10	0.15 ± 0.06	P	−1.52	12.35/8	K
PB941222	819.02	5 36 53 894	49.99 ± 0.22	4.92 ± 0.27	42.22 ± 17.83	3.16 ± 1.25	0.44 ± 0.01	S	6.53	115.77/40	K
PB950111	821.04	12 18 47 790	18.82 ± 1.46	1.29 ± 0.20	1.47 ± 0.56	0.29 ± 0.13	0.27 ± 0.04	S	1.36	6.54/14	BK
PB950112	821.05	7 45 41 212	51.47 ± 0.83	1.97 ± 0.21	2.16 ± 0.86	1.30 ± 0.60	0.15 ± 0.02	P	−1.98	8.11/9	K
PB950114	822.01	13 10 32 276	8.67 ± 0.67	4.04 ± 0.25	0.93 ± 0.35	0.77 ± 0.30	0.09 ± 0.02	P	−2.56	7.24/10	KUT
PB950211	829.01	20 08 20 819	23.45 ± 1.06	2.40 ± 0.22	1.71 ± 0.69	0.71 ± 0.35	0.15 ± 0.02	P	−1.97	18.94/11	BKU
PB950305	835.01	15 05 17 909	58.97 ± 1.00	3.15 ± 0.23	3.08 ± 1.20	0.56 ± 0.22	0.29 ± 0.03	S	2.29	12.91/18	BK
PB950325	837.01	7 10 44 283	6.47 ± 0.84	4.14 ± 0.24	2.07 ± 0.82	2.35 ± 0.95	0.30 ± 0.03	S	3.49	30.99/19	BKU
PB950403a	842.01	13 19 50 238	11.26 ± 0.41	6.66 ± 0.30	9.85 ± 3.76	1.57 ± 0.61	0.19 ± 0.01	P	−2.14	40.42/26	BKUY
PB950403b	842.02	23 33 50 352	23.42 ± 0.19	20.01 ± 0.61	15.72 ± 5.99	12.23 ± 4.73	0.21 ± 0.01	S	2.04	55.80/33	BKUD
PB950404	842.03	3 23 32 240	1.65 ± 0.65	1.68 ± 0.21	0.27 ± 0.13	0.54 ± 0.26	0.24 ± 0.07	P	−1.90	8.32/7	
PB950418	844.01	23 16 35 985	13.67 ± 2.70	1.94 ± 0.21	1.21 ± 0.46	0.42 ± 0.18	0.22 ± 0.03	S	3.05	12.55/14	BK
PB950419	844.02	2 23 46 686	1.04 ± 0.03	9.62 ± 0.38	3.10 ± 1.19	6.13 ± 2.38	0.31 ± 0.02	S	3.59	29.39/28	KU
PB950512	848.01	0 16 48 150	51.25 ± 0.33	9.77 ± 0.33	17.01 ± 7.17	2.96 ± 1.14	0.19 ± 0.01	S	2.78	31.22/21	KUS
PB950526	849.01	4 36 57 281	62.11 ± 0.46	1.45 ± 0.20	1.19 ± 0.51	0.57 ± 0.29	0.32 ± 0.05	P	−1.31	3.28/8	K
PB950624	855.01	23 22 05 401	7.56 ± 0.62	1.74 ± 0.20	1.09 ± 0.47	0.36 ± 0.16	0.20 ± 0.04	P	−1.88	8.28/9	BK
PB950625a	855.02	4 03 42 561	8.31 ± 1.26	1.17 ± 0.20	0.49 ± 0.19	0.23 ± 0.10	0.09 ± 0.04	P	−2.22	1.85/8	BK
PB950625b	855.03	5 19 35 248	5.49 ± 0.61	1.66 ± 0.20	0.70 ± 0.27	0.38 ± 0.15	0.09 ± 0.03	P	−2.48	13.96/9	K
PB950701a	856.03	3 32 41 722	57.26 ± 1.65	2.56 ± 0.22	1.84 ± 0.73	0.73 ± 0.28	0.24 ± 0.03	S	3.64	11.80/16	BKUY
PB950701b	856.04	6 35 37 770	8.83 ± 0.19	2.58 ± 0.22	0.98 ± 0.38	0.43 ± 0.17	0.17 ± 0.03	S	1.98	10.69/11	BKU
PB950703	856.05	5 33 42 000	45.28 ± 1.74	4.15 ± 0.26	21.21 ± 8.01	0.97 ± 0.38	0.22 ± 0.01	B	506.08	58.55/28	KD
PB950909	867.01	23 44 38 894	32.14 ± 5.57	1.79 ± 0.20	2.36 ± 0.95	0.19 ± 0.08	0.32 ± 0.04	S	2.33	14.19/16	BK
PB951011a	876.01	0 44 37 284	0.25 ± 0.06	1.02 ± 0.21	0.12 ± 0.06	0.25 ± 0.11	0.39 ± 0.17	P	−1.37	2.97/4	
PB951011b	876.03	21 34 55 420	119.41 ± 1.55	3.41 ± 0.23	19.48 ± 7.55	1.38 ± 0.58	0.31 ± 0.01	S	2.09	31.95/28	BKD
PB951013	876.04	15 51 37 022	0.09 ± 0.04	1.14 ± 0.21	0.28 ± 0.13	0.66 ± 0.32	0.37 ± 0.12	P	−1.52	0.93/3	K
PB951014	876.05	3 38 26 193	1.58 ± 0.11	12.63 ± 0.62	17.43 ± 9.00	10.06 ± 3.89	0.30 ± 0.02	S	3.88	51.81/32	KTU
PB960124	888.01	0 56 28 045	7.03 ± 0.56	4.05 ± 0.25	4.14 ± 1.58	2.39 ± 1.04	0.20 ± 0.02	P	−1.84	44.60/22	BKUT
PB960607	909.01	21 41 49 791	103.34 ± 1.60	2.55 ± 0.22	3.25 ± 1.32	0.41 ± 0.16	0.21 ± 0.03	P	−2.09	3.76/10	BKU

[a] The fluence and peak flux at energy above 100 keV.

[b] The hardness of the integrated energy spectra defined as the ratio of count numbers in the ranges 400–1000 and 100–400 keV.

[c] The burst was observed by other instruments: (B) BATSE, (K) KONUS/WIND, (T) TGRS/WIND, (U) ULYSSES, (Y) YOHKOH, (D) DMS, (S) SROSS-C.

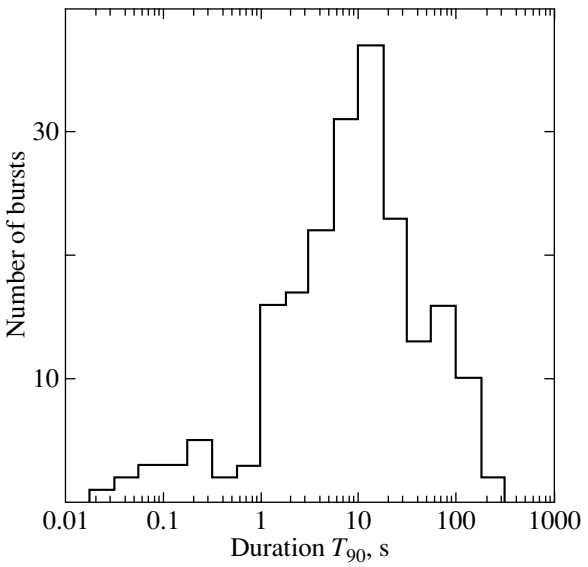

Fig. 2. The T_{90} distribution of 206 GRBs detected over the entire period of PHEBUS operation.

The table lists temporal and spectral characteristics of 32 GRBs detected over the period under consideration. For each event, it gives the burst detection date, the number of the Granat session in which this event was recorded, and the Universal Time T_0 of the PHEBUS burst cell triggering.

The Notes column gives information on the recording of these events by the burst instruments of other satellites: BATSE, KONUS/WIND, TGRS/WIND, ULYSSES, YOHKOH, DMS (Defense Meteorite Satellite Program), and SROSS-C. When compiling the list of confirmations, we used data from the Web page http://ssl.berkeley.edu/ipn3/masterli.txt.

BURST TEMPORAL CHARACTERISTICS

Figure 1 shows the GRB light curves in the energy range 100 keV to 1.6 MeV. The time was measured from the PHEBUS burst cell triggering T_0. The count rate was determined as a sum of the count rates of three detectors in which the count rate was at a maximum. We chose the time interval and time resolution for each event individually, because the burst temporal structure and duration varied widely. Note that because of the Granat high-apogee orbit, the detector background was highly constant and its variations on time scales of the order of the characteristic burst duration (1–100 s) were negligible.

The table lists the burst durations defined by T_{90}. This parameter is the interval between the times when 5 and 95% of the total burst energy was released; it is commonly used to measure the burst durations. Figure 2 presents the T_{90} distribution of 206 GRBs detected over the entire period of PHEBUS operation. Similar to other experiments (Kouveliotou *et al.* 1993), there are two peaks in this distribution. This bimodal pattern in the duration distribution of GRBs may suggest that the sources of short and long events are different in nature.

$\langle V/V_{\max}\rangle$. One of the uniformity criteria for the spatial distribution of GRBs is the $\langle V/V_{\max}\rangle$ ratio, where V is the volume of the minimum sphere containing a burst and $V_{\max}$ is the maximum volume of space accessible to burst detection at a given time (Schmidt *et al.* 1988; Higdon and Schmidt 1990). The value of $V_{\max}$ is determined by the instrument sensitivity. For a spatially uniform distribution of the sources, $\langle V/V_{\max}\rangle$ must be 1/2. If $C_{\max}$ is the maximum count rate recorded during a burst and $C_{\min}$ is the threshold count rate at which the event will be detected, then $V/V_{\max} = (C_{\min}/C_{\max})^{3/2}$.

For the PHEBUS bursts, $C_{\max}/C_{\min}$ was calculated for each of the six detectors. The burst signal could be generated on two time scales (0.25 and 1 s). We computed $C_{\max}/C_{\min}$ on these two scales and then determined on which of them a maximum was reached in a given detector. To determine the mean ratio $\langle V/V_{\max}\rangle$, we used not the maximum value but the second largest value of $C_{\max}/C_{\min}$ among the six detectors on the chosen time scale, because the triggering of the PHEBUS burst detection circuit required that the threshold be exceeded in at least two detectors. The values of $C_{\max}/C_{\min}$ obtained for each burst are given in the table.

For the events recorded by PHEBUS from October 1994 until December 1996, we obtained $\langle V/V_{\max}\rangle = 0.336 \pm 0.018$. The mean value of $V/V_{\max}$ for all of the 206 GRBs detected over the entire period of PHEBUS operation is 0.336 ± 0.007. This value differs from 1/2 expected for a uniform distribution of GRB sources in Euclidean space by more than 23 standard deviations. The derived value is in agreement with the data of other experiments (Hurley 1992; Ogasaka *et al.* 1991; Atteia *et al.* 1991; Mitrofanov *et al.* 1992; Dezalay *et al.* 1994; Meegan *et al.* 1996; Paciesas *et al.* 1999).

GRB SPECTRAL CHARACTERISTICS

For each GRB, the table gives the fluence and peak flux at energy above 100 keV. The errors in the fluxes are not only statistical: we also took into account the uncertainty in the PHEBUS effective area attributable to the unknown position of the GRB source in the sky. Also given in the table is the hardness of the integrated energy spectra, defined as the ratio of count numbers in the energy ranges 400–1000 and 100–400 keV.

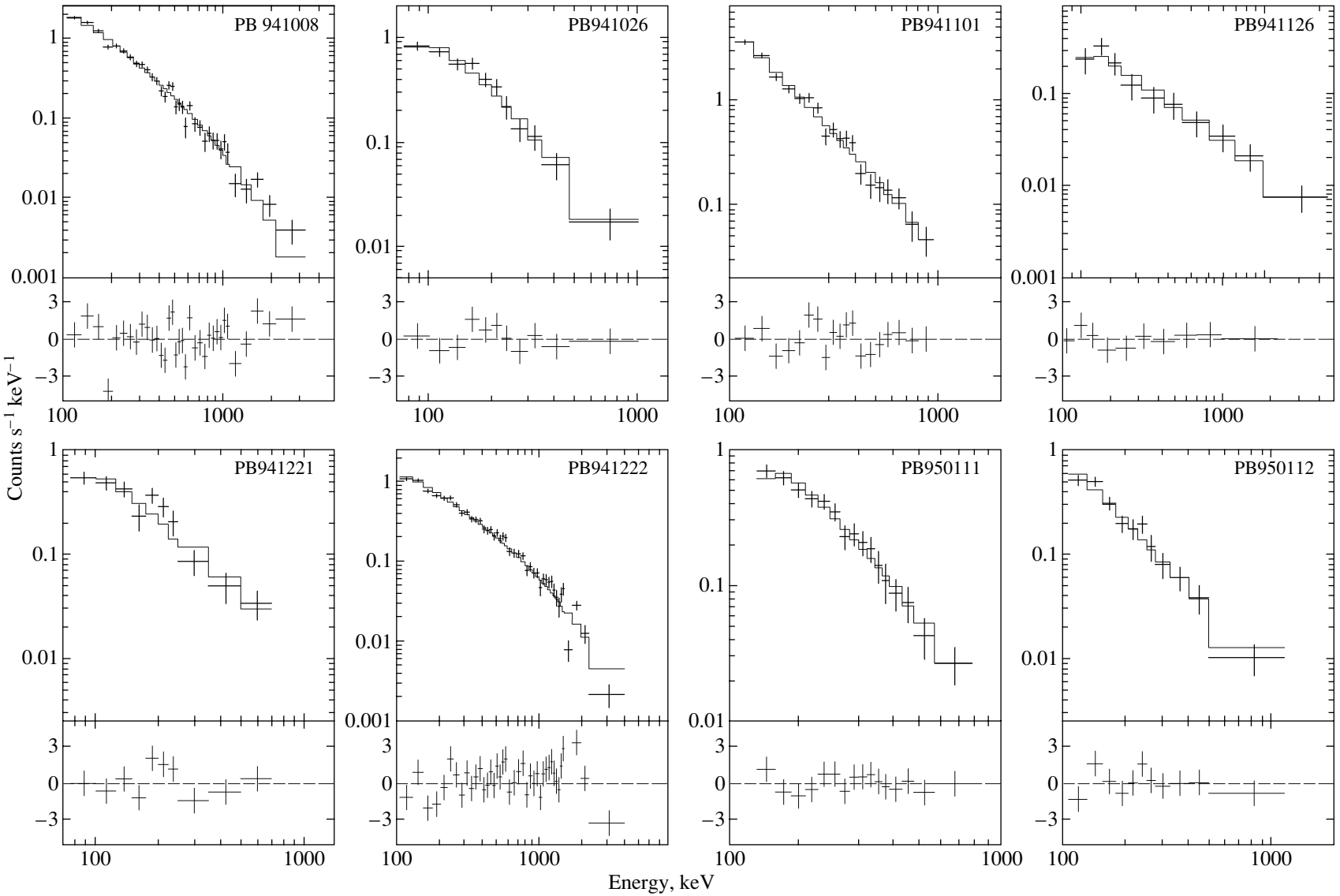

Fig. 3. Time-integrated energy spectra for all 32 GRBs. The broken line represents the best fit to the data (see the text). The lower panel of each figure shows deviations of the experimental data from the analytic curve, in units of standard deviations (σ).

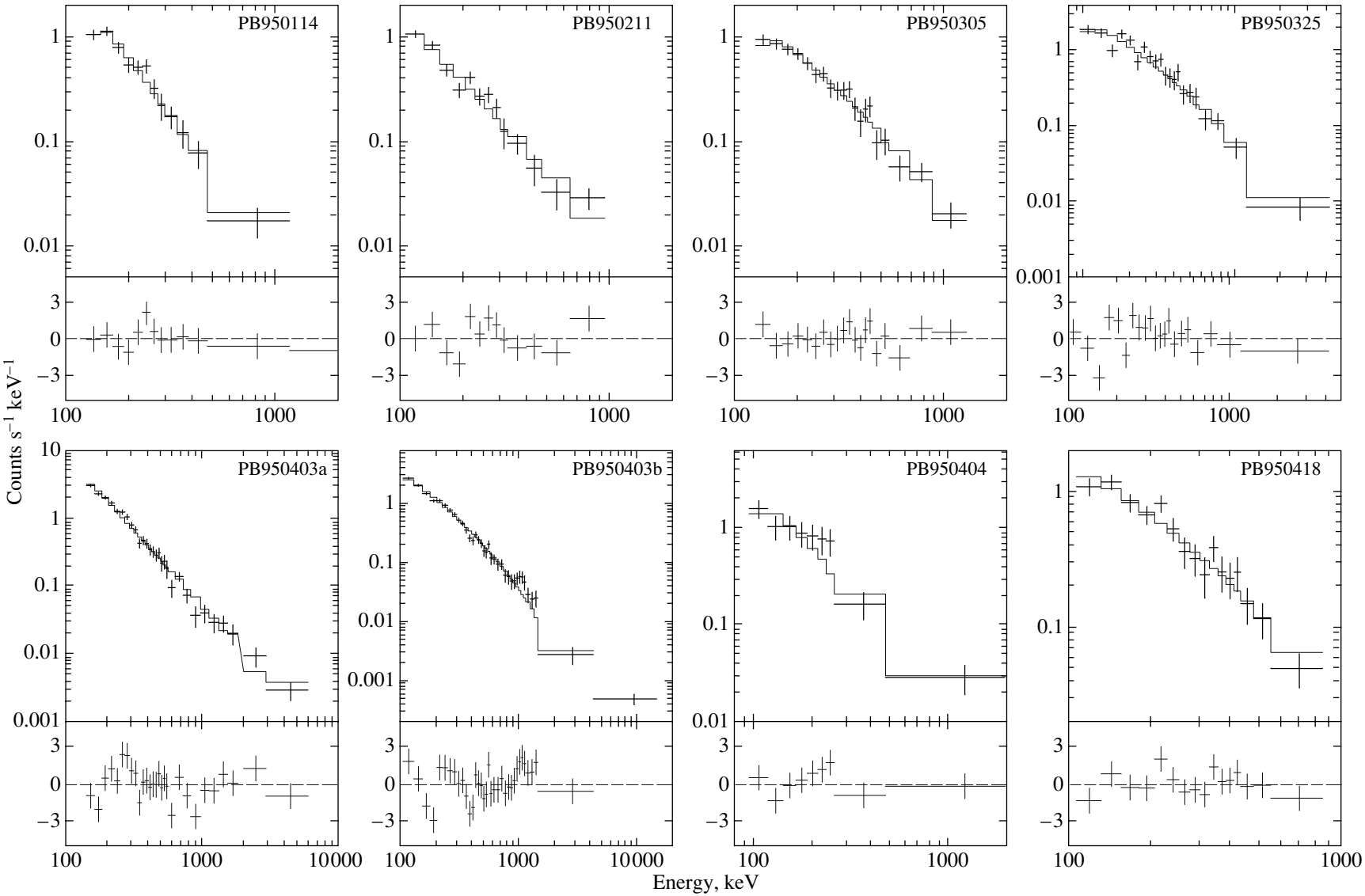
PB950114
PB950211
PB950305
PB950325
PB950403a
PB950403b
PB950404
PB950418
Counts s^{-1} keV^{-1}
Energy, keV

Fig. 3. (Contd.)

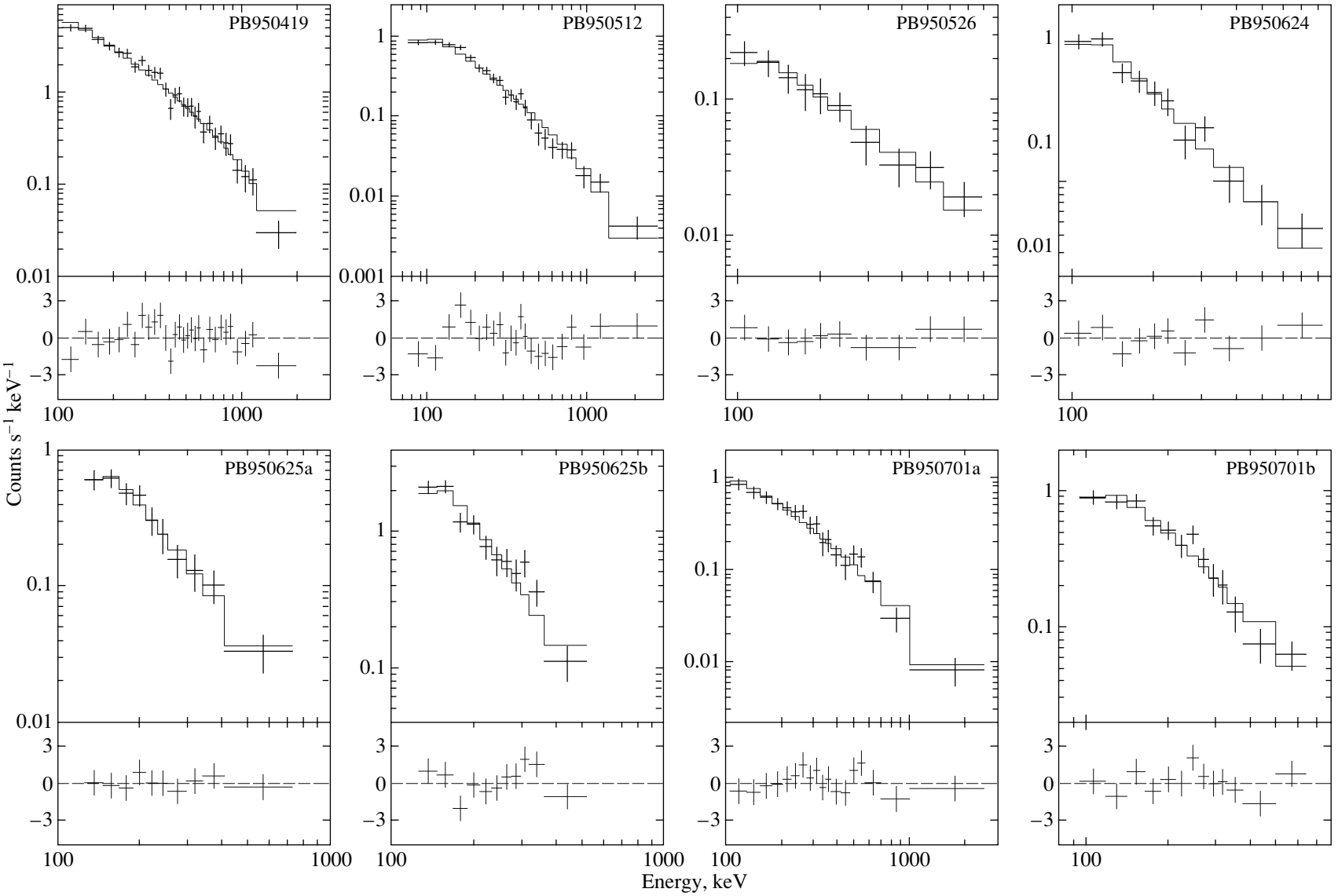
PB950419
PB950512
PB950526
PB950624
PB950625a
PB950625b
PB950701a
PB950701b
Counts s^{-1} keV^{-1}
Energy, keV

Fig. 3. (Contd.)

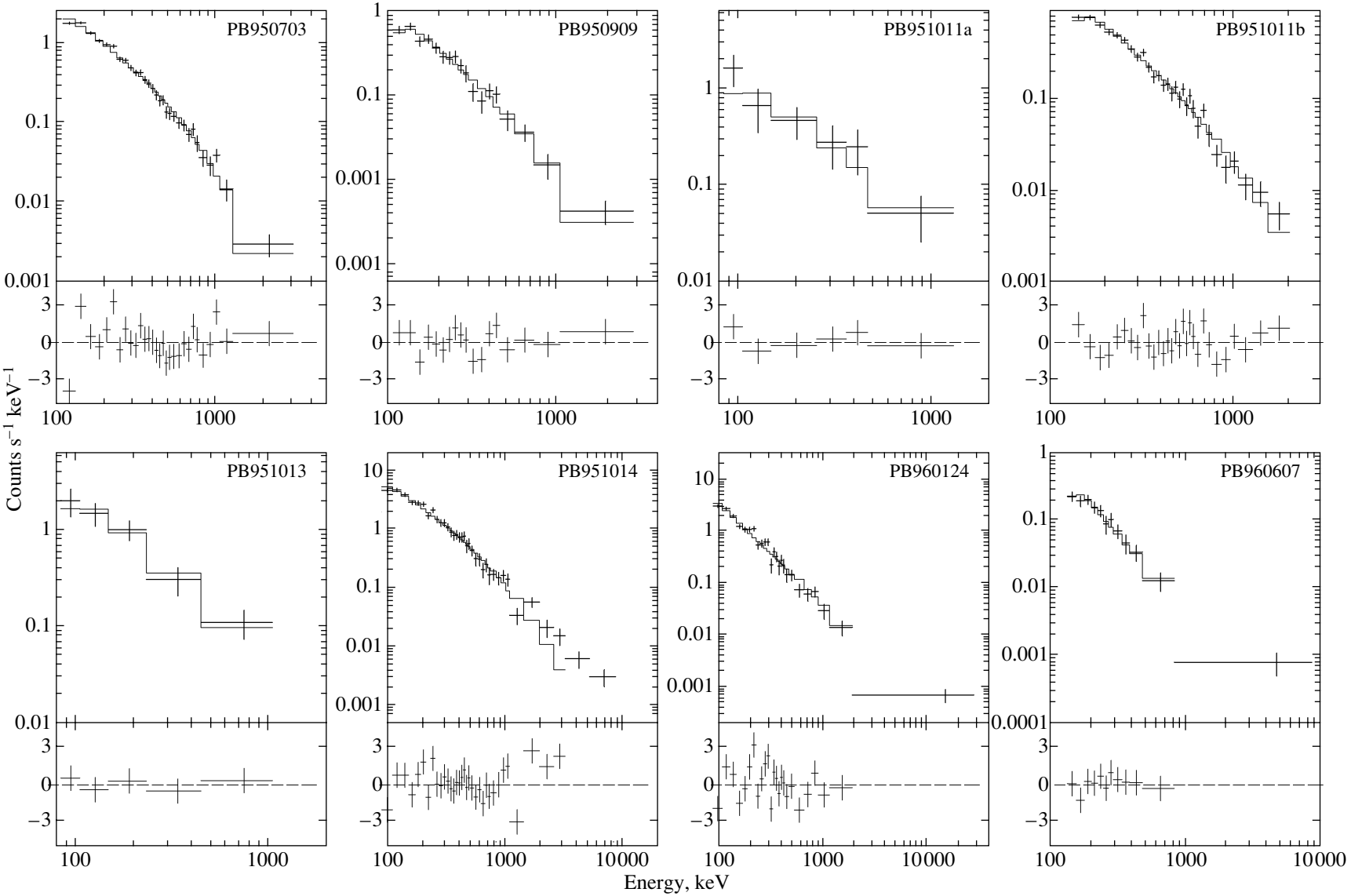
PB950703
PB950909
PB951011a
PB951011b
PB951013
PB951014
PB960124
PB960607
Counts s^{-1} keV^{-1}
Energy, keV

Fig. 3. (Contd.)

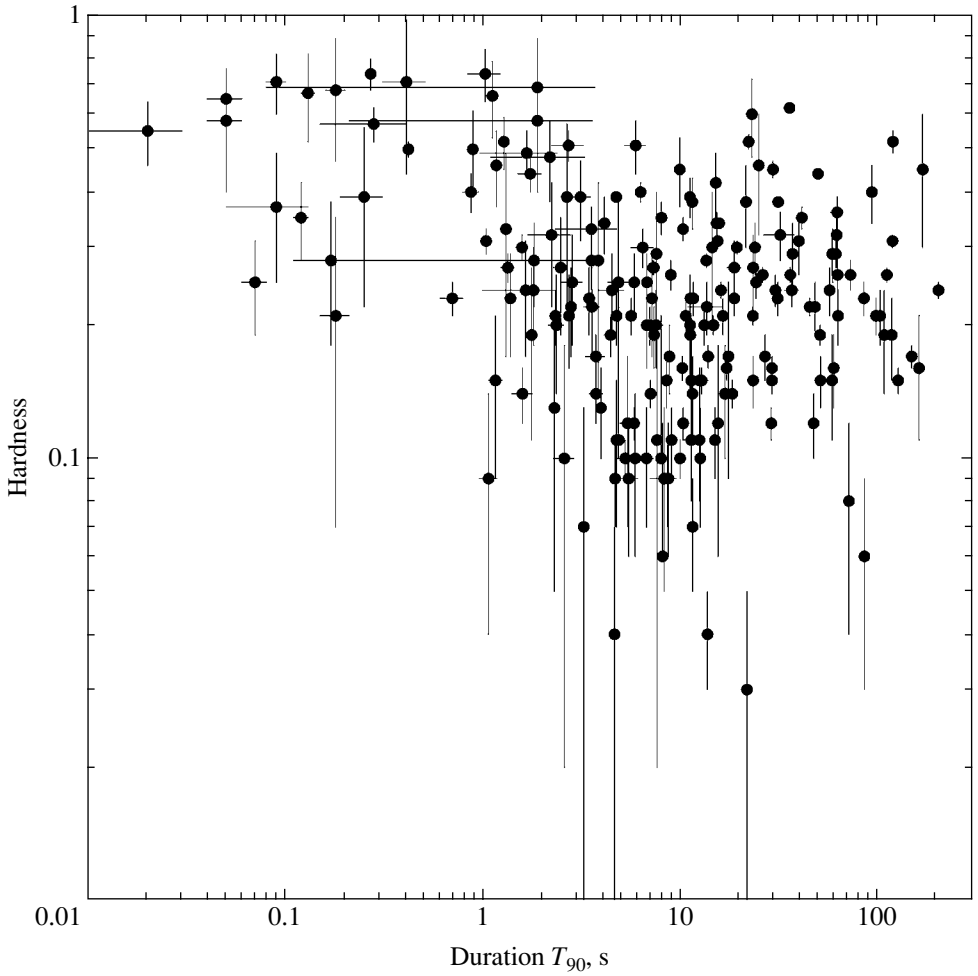

Fig. 4. Burst hardness *versus* burst duration T_{90}. The mean hardness for bursts with durations shorter and longer than 2 s is 0.428 ± 0.018 and 0.231 ± 0.008, respectively.

Figure 3 shows time-integrated energy spectra for the 32 GRBs of this catalog. The integration time is T_{90}. For a convenient comparison of the slopes in the spectra, we chose the scales on the horizontal and vertical axes in all figures in such a way that the diagonal running from the upper left corner to the lower right corner corresponded to a power law with an index of -2. The broken line is the best fit to the data by one of the following functions: the power law $I(E) = AE^p$, where E is the photon energy, p is the exponent; the bremsstrahlung law $I(E) = A\exp(-E/kT)/E$, where T is the characteristic temperature, k is the Boltzmann constant; and the synchrotron radiation law $I(E) = A\exp\{-(E/E_c)^{1/3}\}$, where $E_c = 4.5^{-1}\omega_{\rm H}\sin\Theta(kT/mc^2)^2$, $\omega_{\rm H}$ is the electron gyrofrequency, and Θ is the angle between the direction of photon motion and the magnetic field (Petrosian 1981).

We chose these laws, because they are most commonly used to fit the burst energy spectra in the energy range under study (Mazets and Golenetskiĭ 1987; Petrosian 1981; Schaefer *et al.* 1994).

We determined the best fit and sought for its parameters by using the χ^2 test. The table lists the best fits to the spectral data: the power law (P), the bremsstrahlung law (B), and the synchrotron radiation law (S). The next columns give their parameters: the dimensionless exponent p; the characteristic temperature kT (in keV) or the parameter E_c (in keV), respectively; and the χ^2/DOF ratio that characterizes the spectrum fitting reliability, where DOF is the number of degrees of freedom.

The hardness is one of the parameters used to investigate GRB spectra and to classify events. This parameter carries information on the fraction of the high-energy photons in the burst energy spectrum, although it gives no idea of the spectral shape.

It has already been noted previously (Dezalay *et al.* 1992; Terekhov *et al.* 1994, 1995a; Kouveliotou *et al.* 1993) that the mean hardness of short bursts is higher than that of long bursts. In Fig. 4, burst hardness is plotted against burst duration. The mean hardness for the cosmic GRBs detected by PHEBUS over the entire period of its operation is 0.428 ± 0.018 for events shorter than 2 s and 0.231 ± 0.004 for events longer than 2 s. The result obtained, as well as the bimodal pattern of the GRB distribution in duration, may suggest that the sources of short and long bursts are different in nature.

ACKNOWLEDGMENTS

This study was supported by the Russian Foundation for Basic Research (project no. 00-02-17251), the Program "Astronomy: Nonstationary Astrophysical Objects" of the Russian Academy of Sciences, and the sixth Examination Competition in 1999 and the Science Support Foundation Grant for Talented Young Researchers. We wish to thank the staff of the Lavochkin Research and Production Association, *Radiopribor* Research and Production Association, the Deep Space Communication Center in Eupatoria, B.S. Novikov, V.I. Evgenov, A.N. Bogomolov, N.G. Khavensonthe from the Space Research Institute (Russian Academy of Sciences) who operated the observatory, and the team of A.V. D'yachkov who processed the telemetry information. We are grateful to E.P. Mazets, R.A. Aptekar', and S.V. Golenetskiĭ from the Ioffe Physicotechnical Institute, Russian Academy of Sciences (St. Petersburg) who provided data on the KONUS/WIND confirmation of several GRBs under discussion.

REFERENCES

1. J.-L. Atteia, C. Barat, E. Jourdain, *et al.*, Nature **351**, 296 (1991).
2. C. Barat, F. Cotin, M. Niel, *et al.*, AIP Conf. Proc. **170**, 395 (1998).
3. J.-P. Dezalay, C. Barat, R. Talon, *et al.*, in *Gamma-Ray Bursts,* Ed. by W. S. Paciesas and C. J. Fishman (American Inst. of Physics, New York, 1992), vol. 304.
4. J.-P. Dezalay, J.-L. Atteia, C. Barat, *et al.*, Astron. Astrophys. **286**, 103 (1994).
5. J. C. Higdon and M. Schmidt, Astrophys. J. **355**, 13 (1990).
6. K. Hurley, in *Gamma-Ray Bursts,* Ed. by W. S. Paciesas and G. J. Fishman (American Inst. of Physics, New York, 1992), p. 3.
7. C. Kouveliotou, C. A. Meegan, G. J. Fishman, *et al.*, Astrophys. J. Lett. **413**, L101 (1993).
8. E. P. Mazets and S. V. Golenetskiĭ, Itogi Nauki Tekh., Ser. Astron. **32**, 16 (1987).
9. C. A. Meegan, G. N. Pendleton, M. S. Briggs, *et al.*, Astrophys. J., Suppl. Ser. **106**, 65 (1996).
10. I. Mitrofanov, A. Pozanenko, J.-L. Atteia, *et al.*, in *Bursts Observations, Analyses and Theories,* Ed. by C. Ho *et al.* (Cambridge Univ. Press, Cambridge, 1992), p. 203.
11. Y. Ogasaka, T. Murakami, J. Nishimura, *et al.*, Astrophys. J. Lett. **383**, L61 (1991).
12. W. S. Paciesas, C. A. Meegan, G. N. Pendleton, *et al.*, Astrophys. J., Suppl. Ser. **122**, 465 (1999).
13. V. Petrosian, Astrophys. J. **251**, 727 (1981).
14. B. Schaefer, B. Teegarden, S. Fantasia, *et al.*, Astrophys. J., Suppl. Ser. **92**, 285 (1994).
15. M. Schmidt, J. C. Hueter, and G. Hueter, Astrophys. J. Lett. **329**, L85 (1988).
16. O. V. Terekhov, D. V. Denisenko, V. A. Lobachev, *et al.*, Pis'ma Astron. Zh. **20**, 323 (1994) [Astron. Lett. **20**, 265 (1994)].
17. O. V. Terekhov, D. V. Denisenko, V. A. Lobachev, *et al.*, Pis'ma Astron. Zh. **21**, 83 (1995a) [Astron. Lett. **21**, 73 (1995a)].
18. O. Terekhov, R. Sunyaev, D. Denisenko, *et al.*, in *Proceedings of the IAU Colloquium No. 151 "Flares and Flashes,"* Ed. by J. Gremer, H. W. Duerbeck, and R. E. Gershberg (Springer-Verlag, Berlin, 1995); Lect. Notes Phys. **454**, 353 (1995b).
19. A. Yu. Tkachenko, O. V. Terekhov, R. A. Sunyaev, *et al.*, Pis'ma Astron. Zh. **24**, 833 (1998) [Astron. Lett. **24**, 722 (1998)].

Translated by G. Rudnitskiĭ

Astronomy Letters, Vol. 28, No. 6, 2002, pp. 366–372. Translated from Pis'ma v Astronomicheskiĭ Zhurnal, Vol. 28, No. 6, 2002, pp. 417–424.

Correlation between Baryon Mass and Intergalactic Gas Temperature in Nearby Galaxy Clusters

A. A. Voevodkin*, A. A. Vikhlinin, and M. N. Pavlinsky

Space Research Institute, Russian Academy of Sciences, ul. Profsoyuznaya 84/32, Moscow, 117810 Russia

Received January 4, 2002

Abstract—We measured the correlation between baryon mass and intracluster gas temperature in nearby galaxy clusters selected from the ROSAT All-Sky Survey. The mass of the intracluster gas was determined directly from an analysis of X-ray images. A correlation was found between the gas mass and the mass of the cluster stellar matter, which was used to determine the total baryon mass (i.e., gas + stars). The mass was measured within the radii corresponding to overdensities of 324 and 500 relative to the mean baryon density inferred from the theory of primordial nucleosynthesis. The measured correlation between baryon mass and temperature is close to that predicted by a self-similar theory of cluster formation: $M \propto T^{3/2}$.

Key words: *galaxy clusters, cosmology, large-scale structure of Universe*

INTRODUCTION

Galaxy clusters, the largest gravitationally bound building blocks of the Universe, are among the main objects on which predictions of cosmological models are tested. Observations of galaxy clusters are particularly well suited for testing theoretical studies of the formation of the large-scale structure in the Universe.

The cosmologically most important cluster parameter is its mass, which, however, is difficult to measure. The point is that the hidden mass can be measured only indirectly from its gravitational effect on the cluster baryonic components, which involves large experimental uncertainties.

Simple estimates show that gravitation is a dominant force on cluster scales. Consequently, there is every reason to expect that the relative composition of the various matter components in clusters is the same as that in the Universe as a whole (White *et al.* 1993). In particular, this implies that the baryon mass fraction in the total mass of the cluster, $f_{\rm bar}$, is a universal quantity. This paper opens a series of papers in which the comparatively easily observable baryon mass in clusters is used for various cosmological by assuming $f_{\rm bar}$ to be constant. We describe a sample of clusters, the technique for determining the baryon mass $M_{\rm bar}$, and discuss the correlation between $M_{\rm bar}$ and intracluster gas temperature.

The baryon mass in clusters is dominated by a hot intracluster gas, which shows up in intense X-ray radiation. Therefore, analysis of ROSAT X-ray images for clusters forms an observational basis for our study.

All numerical values were obtained by assuming that the cosmological parameters are $H_0 = 50$ km s^{-1} Mpc^{-1}, $\Omega = 1$, and $\Lambda = 0$.

CLUSTER SELECTION

Systematic studies require a statistically complete sample of objects. In our case, it is desirable that the sample be drawn from all-sky catalogs and that clusters in a wide mass range could be found among the selected objects. Of the observed parameters that are commonly used to detect clusters, the X-ray luminosity correlates most closely with the total mass. Therefore, for cluster selection, we used X-ray catalogs compiled from ROSAT All-Sky Survey data (Ebeling *et al.* 2000; de Grandi *et al.* 1999; Bohringer *et al.* 2000).

The cluster selection criteria were the following:

(1) The absorption-corrected 0.5–2 keV X-ray flux exceeds 1.4×10^{-11} erg s^{-1} cm^{-2}. We used this criterion, because this flux is approximately a factor of 3 higher than the typical sensitivity limit in the ROSAT All-Sky Survey and, hence, we can be sure that the catalogs are complete. In addition, there are no high-quality data for a substantial number of clusters below this flux; at the same time, this limit is low enough for low-mass clusters to be included in the sample.

(2) The redshift lies within the range $0.01 \le z \le 0.1$. We chose this criterion, because the ROSAT

*E-mail: voevodkin@hea.iki.rssi.ru

Table 1. A list of clusters and their properties

Clusters	z	T^a	$f_{\rm X}^b$	$N_{\rm H}^c$	$r_{324}^{{\rm gas}\,d}$	$M_{324}^{{\rm gas}\,e}$	$r_{500}^{{\rm gas}\,d}$	$M_{500}^{{\rm gas}\,e}$	r_{324}^f	M_{324}^g	r_{500}^f	M_{500}^g
2A0335	0.0349	3.60 ± 0.10[1]	6.82	26.00*	2.45	1.23 ± 0.28	1.93	0.93 ± 0.11	2.64	1.53 ± 0.29	2.10	1.20 ± 0.15
A85	0.0556	6.90 ± 0.20[2]	4.41	3.45	2.98	2.35 ± 0.51	2.46	2.04 ± 0.22	3.15	2.77 ± 0.50	2.62	2.45 ± 0.28
A119	0.0442	5.60 ± 0.20[2]	2.46	3.20	3.01	2.35 ± 0.39	2.42	1.87 ± 0.10	3.20	2.80 ± 0.34	2.59	2.30 ± 0.13
A262	0.0163	2.21 ± 0.03[3]	4.56	5.38	1.84	0.48 ± 0.19	1.46	0.37 ± 0.10	2.01	0.63 ± 0.22	1.62	0.51 ± 0.13
A400	0.0238	2.30 ± 0.10[4]	1.65	9.38	1.94	0.58 ± 0.08	1.49	0.41 ± 0.02	2.13	0.77 ± 0.07	1.66	0.57 ± 0.03
A401	0.0739	8.00 ± 0.24[2]	3.17	10.50	3.83	5.23 ± 1.04	3.10	4.30 ± 0.38	4.01	6.03 ± 0.94	3.28	5.05 ± 0.48
A478	0.0882	6.86 ± 0.08[1]	4.54	33.75*	3.63	4.66 ± 0.94	2.98	3.96 ± 0.40	3.81	5.37 ± 0.85	3.14	4.64 ± 0.48
A496	0.0328	4.70 ± 0.10[5]	5.38	4.58	2.58	1.42 ± 0.32	2.07	1.13 ± 0.13	2.76	1.74 ± 0.33	2.23	1.43 ± 0.18
A1367	0.0214	3.70 ± 0.10[6]	4.79	2.31	2.30	0.97 ± 0.29	1.86	0.80 ± 0.16	2.47	1.21 ± 0.31	2.02	1.02 ± 0.20
A1656	0.0231	8.10 ± 0.10[6]	18.62	0.92	3.63	3.84 ± 0.76	2.85	2.89 ± 0.31	3.83	4.53 ± 0.71	3.05	3.52 ± 0.35
A1795	0.0622	6.00 ± 0.10[7]	3.92	1.19	2.88	2.15 ± 0.33	2.37	1.87 ± 0.09	3.04	2.55 ± 0.24	2.53	2.25 ± 0.11
A2029	0.0766	9.10 ± 0.60[2]	4.27	3.05	3.51	4.07 ± 0.92	2.80	3.17 ± 0.40	3.70	4.77 ± 0.89	2.97	3.82 ± 0.49
A2052	0.0353	3.40 ± 0.10[8]	2.94	2.72	2.18	0.70 ± 0.21	1.76	0.57 ± 0.10	2.36	0.89 ± 0.23	1.93	0.75 ± 0.13
A2063	0.0355	3.68 ± 0.11[9]	2.42	2.99	2.20	0.87 ± 0.25	1.77	0.70 ± 0.13	2.38	1.10 ± 0.28	1.93	0.90 ± 0.16
A2142	0.0894	9.30 ± 0.60[10]	3.98	4.20	4.24	7.44 ± 0.98	3.39	5.83 ± 0.19	4.44	8.53 ± 0.43	3.57	6.83 ± 0.22
A2147	0.0353	4.40 ± 0.20[6]	3.21	3.38	3.04	2.39 ± 0.74	2.29	1.57 ± 0.34	3.24	2.90 ± 0.79	2.50	2.04 ± 0.42
A2199	0.0299	4.80 ± 0.10[5]	6.53	0.86	2.51	1.31 ± 0.17	2.02	1.05 ± 0.04	2.70	1.61 ± 0.08	2.19	1.33 ± 0.05
A2256	0.0581	7.30 ± 0.30[2]	3.75	5.00*	3.57	4.07 ± 0.51	2.81	3.07 ± 0.07	3.78	4.80 ± 0.16	3.00	3.72 ± 0.09
A2589	0.0416	3.70 ± 0.70[6]	1.61	4.14	2.03	0.67 ± 0.18	1.65	0.56 ± 0.08	2.23	0.88 ± 0.20	1.77	0.69 ± 0.10
A2634	0.0309	3.40 ± 0.30[6]	1.56	5.07	2.10	0.76 ± 0.16	1.69	0.62 ± 0.06	2.27	0.96 ± 0.16	1.85	0.81 ± 0.09
A2657	0.0400	3.70 ± 0.20[2]	1.72	8.48*	2.17	0.86 ± 0.18	1.78	0.74 ± 0.07	2.33	1.07 ± 0.18	1.93	0.94 ± 0.10
A3112	0.0750	5.30 ± 0.50[2]	1.90	2.62	2.69	1.82 ± 0.50	2.19	1.51 ± 0.26	2.86	2.18 ± 0.53	2.34	1.86 ± 0.32
A3158	0.0591	5.77 ± 0.10[3]	2.29	1.46	2.84	2.05 ± 0.60	2.22	1.51 ± 0.29	3.03	2.48 ± 0.63	2.40	1.92 ± 0.35
A3266	0.0589	8.00 ± 0.31[2]	3.54	1.59	3.53	3.95 ± 0.64	2.90	3.38 ± 0.17	3.71	4.58 ± 0.51	3.07	3.98 ± 0.21
A3376	0.0455	4.00 ± 0.24[2]	1.43	4.85	2.29	1.03 ± 0.22	1.89	0.89 ± 0.08	2.45	1.26 ± 0.23	2.04	1.12 ± 0.12
A3391	0.0514	5.70 ± 0.20[2]	1.55	5.51	2.92	2.19 ± 0.55	2.20	1.43 ± 0.22	3.13	2.67 ± 0.57	2.40	1.87 ± 0.29
A3395	0.0506	5.00 ± 0.30[9]	1.93	6.12	3.29	3.10 ± 0.87	2.51	2.14 ± 0.39	3.50	3.76 ± 0.91	2.71	2.69 ± 0.49
A3667	0.0556	7.00 ± 0.36[2]	4.61	4.73	4.00	5.65 ± 0.93	3.24	4.64 ± 0.22	4.19	6.51 ± 0.76	3.41	5.44 ± 0.27
A4038	0.0292	3.31 ± 0.25[11]	3.55	1.56	2.24	0.82 ± 0.24	1.70	0.56 ± 0.09	2.44	1.05 ± 0.27	1.90	0.77 ± 0.13
A4059	0.0460	4.40 ± 0.18[2]	2.01	1.10	2.27	1.00 ± 0.29	1.79	0.76 ± 0.13	2.46	1.28 ± 0.31	1.93	0.96 ± 0.17
MKW3s	0.0453	3.70 ± 0.10[2]	2.14	3.04	2.16	0.87 ± 0.28	1.67	0.62 ± 0.13	2.35	1.11 ± 0.31	1.85	0.84 ± 0.17
MKW4	0.0198	1.71 ± 0.09[9]	1.52	1.89	1.51	0.30 ± 0.05	1.14	0.20 ± 0.01	1.69	0.43 ± 0.05	1.30	0.30 ± 0.02
NGC507	0.0164	1.26 ± 0.07[9]	1.62	5.24	1.45	0.24 ± 0.04	1.10	0.16 ± 0.01	1.62	0.34 ± 0.04	1.26	0.25 ± 0.02
A S1101	0.0580	2.60 ± 0.10[12]	1.47	1.77	1.80	0.52 ± 0.14	1.52	0.48 ± 0.07	1.95	0.66 ± 0.15	1.64	0.61 ± 0.09

[a] Intracluster gas temperature (keV): 1—our Chandra measurement, 2—Markevitch *et al.* (1998), 3—White (2000), 4—Fukazawa *et al.* (1998), 5—Markevtich *et al.* (1999), 6—David *et al.* (1993), 7—Arnaud *et al.* (2001), 8—Blanton *et al.* (2001), 9—Horner *et al.* (1999), 10—Allen and Fabian (1998), 11—Finoguenov *et al.* (2001), 12—Kaastra *et al.* (2001).

[b] The 0.5–2 keV X-ray flux, in units of 10^{-11} erg s^{-1} cm^{-2}, was measured within a circle of radius $7r_c$ (see text for the determination of r_c).

[c] Absorption column density, 10^{20} cm^{-2}.

[d] The radius corresponding to the gas mass for a given baryon overdensity (Mpc).

[e] The gas mass within the radius of a given overdensity ($10^{14}\ M_\odot$).

[f] The radius corresponding to the total mass of the gas and stars for a given baryon overdensity (Mpc).

[g] The total mass of the gas and stars within the radius of a given overdensity ($10^{14}\ M_\odot$).

* The absorption column density was determined from a fit to the X-ray spectrum rather than from radio surveys.

angular resolution for more distant clusters is generally insufficient for image analysis, while large-scale variations in the X-ray background are too significant for closer clusters. Table 1 lists the selected clusters, measured X-ray fluxes, and such parameters as the temperature and redshift taken from the literature.

ANALYSIS OF X-RAY DATA

Most of the selected clusters have ROSAT PSPC pointed observations. We used these data if the cluster regions that were required to extract useful information fitted into a 1° field of view. Otherwise, we used data adopted from the ROSAT All-Sky Survey.

We analyzed images in the energy range 0.7–2 keV, in which the ROSAT sensitivity (the ratio of cluster surface brightness to background) was highest.

Image Reduction

When using the all-sky survey data, we divided the $6.4° \times 6.4°$ photon image by the exposure map[1] accessible from the data archive. When using individual pointings, we performed a more careful analysis based on the software package described by Snowden *et al.* (1994). This software reveals the periods of a high particle background and the background of solar radiation scattered by the upper atmosphere and performs appropriate data filtering. The exposure map is also computed for the chosen energy range. In the end, we obtain an image with all instrumental defects removed as thoroughly as possible. If several observations were carried out for a cluster, then we first reduced the data for individual observations and then coadded the derived images.

X-ray images contain cluster radiation, numerous point sources, and a diffuse background. Point sources are relatively easy to separate from the cluster radiation, because they are localized in space. At the same time, an accurate background subtraction requires an accurate analysis of the X-ray flux components.

Determining the X-ray Background

In the images obtained in individual pointings, the cluster often fills almost the entire field of view and in these cases, a reference region that could be used to determine the background cannot be selected. The method of measuring the background is based on the assumption that the X-ray brightness profile of the cluster itself at large radii is described by a power function of r and that the background may be considered constant. The brightness profile was constructed by azimuthally averaging the image in concentric rings of equal logarithmic width with a 1.1 step centered on the cluster brightness maximum. The constructed profile was fitted by the so-called β-model (Cavaliere and Fusco-Femiano 1976)

$$S(r) = \frac{S_0}{(1 + r^2/r_c^2)^{3\beta - 0.5}} + S_1, \qquad (1)$$

where the parameters r_c, S_0, and β describe the cluster brightness profile and S_1 is the term responsible for the background. We fixed r_c at the values derived from the established correlation with cluster temperature, $r_c = 0.125\,(T/1\ \mathrm{keV})^{1/2}$ Mpc (Vikhlinin *et al.* 1999). Since two or three portions with different slopes can be singled out in the brightness profile, we chose the portion farthest from the center in which the fitting accuracy is still sufficiently high to determine the background more accurately. Actually, the following approach was applied: if β could be determined with an accuracy better than 13% for $r \geq 4r_c$, then the derived β, S_0, and S_1 were taken; otherwise, the radii $r \geq 3r_c$ were used for fitting.

Determining the Gas Mass in a Cluster

When determining the gas mass in a cluster, we assumed the latter to be spherically symmetric. This assumption allowed the surface brightness profile to be transformed into a three-dimensional plasma emissivity profile by using the deprojection method (Fabian *et al.* 1981). The emissivity can be reliably converted to the electron density using the formula $n_e = K\sqrt{\varepsilon}$, where K can be determined from the model of thermal radiation from optically thin plasma (Raymond and Smith 1977). Given n_e, we can easily determine the intracluster gas density: $\rho_g = 1.15 n_e m_p$, where the numerical coefficient corresponds to a cosmic mixture of hydrogen and helium.

Note that the transformation of the X-ray brightness in a chosen energy range into the gas mass depends weakly on gas temperature and is almost independent of the heavy-element abundance at $T >$ 2 keV (Fabricant *et al.* 1980). However, the cluster asymmetry, which shows up in azimuthal brightness variations, can affect the accuracy of the mass determination. For this reason, we included an additional error of 7% in the uncertainty of the mass measurement. This error is generally a conservative upper limit on the uncertainty of the mass determination due to deviations from spherical symmetry (Vikhlinin *et al.* 1999).

[1] In the ROSAT data reduction system, the exposure map means an image that includes not only variations in observational time but also detector peculiarities.

For comparison with theoretical models, the cluster mass should be measured within the radii characterized by a fixed overdensity $\delta = 3M(r)/4\pi r^3/\langle\rho\rangle$, where $\langle\rho\rangle$ is the mean matter density in the Universe. If the baryon fraction is assumed to be universal, the radius of a given overdensity can be determined from the baryon overdensity. Thus, the masses were measured at the radii corresponding to the baryon overdensities $\delta = 324$ and 500, for which detailed theoretical studies of the cluster mass functions were carried out (Jenkins *et al.* 2001; Evrard *et al.* 1996). We used the mean baryon density $\rho_{\rm bar} = (1+z)^3\,5.55\,M_\odot/{\rm kpc}^3$ (Burles *et al.* 2001) inferred in the theory of primordial nucleosynthesis to calculate the baryon overdensity.

At the radii of the overdensities concerned, the statistical accuracy of measuring the surface brightness is low, because the recorded X-ray background is comparable to the radiation from the cluster. Therefore, to eliminate the artificial noise that appears when measuring the mass by the deprojection technique, we substituted the measured brightness profile at $r \geq 7r_c$ by the best fit based on formula (1) but assigned an error in the actual data to the inferred values. Subsequently, we applied a standard mass measurement procedure to the combined brightness profile.

CORRELATION BETWEEN TEMPERATURE AND BARYON MASS IN A CLUSTER

Table 1 lists the measured intracluster gas masses and the corresponding overdensity radii r_{324} and r_{500}. We see from Fig. 1 that the measured masses correlate well with the cluster temperature. The M–T correlation was fitted by a power function of the form $M = AT^b$. Below, we inferred the best-fit parameters by linear-function fitting in logarithmic coordinates $\log M = a + b\log T$ by using the so-called bisector method described by Akritas and Bershadi (1996). The confidence intervals for the parameters were determined by using bootstrap resampling (Press *et al.* 1992). The derived best-fit parameters are given in Table 2, and the corresponding relations are indicated by the solid line in Fig. 1.

Our sample includes several clusters with highly asymmetric images (A1367, A2142, A2147, A2256, A3266, A3376, A3395, and A3667), because these clusters appear to be in the process of merging of two or more building blocks. Because of the large deviations from spherical symmetry, the mass measurement by the deprojection technique for such clusters yields a fairly unreliable result. Indeed, as we see from Fig. 1, these clusters exhibit larger deviations from the mean $M(T)$ relation than the clusters with azimuthally symmetric images. Therefore, we also determined the parameters of the $M(T)$ correlation without asymmetric clusters. As a result, we obtained a slightly flatter relation than for the complete sample [$M_{324} \propto T^{1.56\,\pm\,0.12}$ compared to $M_{324} \propto T^{1.76\,\pm\,0.13}$, see Table 2 and the dash-dotted lines in Fig. 1].

Table 2. Correlation coefficients in the relation $\log M_\delta[M_\odot] = a + b\log T[{\rm keV}]$

Parameter	δ	a	b
Gas	324	13.0	1.76 ± 0.13
	500	12.8	1.88 ± 0.13
Gas, symmetric clusters	324	13.1	1.59 ± 0.12
	500	12.9	1.74 ± 0.13
Gas + stars	324	13.2	1.66 ± 0.13
	500	13.0	1.74 ± 0.13
Gas + stars, symmetric clusters	324	13.3	1.49 ± 0.11
	500	13.1	1.60 ± 0.13

Table 3. Optical luminosities of the clusters

Cluster	L^a, $10^{13}L_\odot$	Cluster	L^a, $10^{13}L_\odot$
A85	0.78 ± 0.12^1	A2029	1.07 ± 0.21^1
A262	0.18 ± 0.06^2	A2052	0.26 ± 0.06^2
A400	0.22 ± 0.06^1	A2063	0.32 ± 0.05^2
A401	0.88 ± 0.33^1	A2142	1.04 ± 0.16^1
A478	0.65 ± 0.17^2	A2199	0.46 ± 0.07^2
A1367	0.28 ± 0.07^1	A2256	1.06 ± 0.11^1
A1656	1.01 ± 0.22^1	A2634	0.38 ± 0.06^1
A1795	0.47 ± 0.07^2	MKW4	0.10 ± 0.03^3

[a] The cluster optical luminosity within radius r_{324}. 1—The compilation from Arnaud *et al.* (1992), 2—Hradecky *et al.* (2000), 3—Beers *et al.* (1984).

Correlation between Optical Luminosity and Mass

Apart from the intracluster gas, the stellar matter contributes appreciably to the total baryon mass of the cluster. To estimate the mass of the cluster stars, we used the correlation between total optical luminosity and intracluster gas mass found for several clusters with high-quality optical data.

To derive this correlation, we used published $L_{\rm opt}$ measurements (Table 3) and our gas masses M_{324}. Since the published optical luminosities are given in different metric apertures (1 Mpc, 3 Mpc, etc.), we reduced them to the radius r_{324} using the King profile:

$$L(r) = k\left(\ln(x+\sqrt{1+x^2}) - \frac{x}{\sqrt{1+x^2}}\right), \quad (2)$$

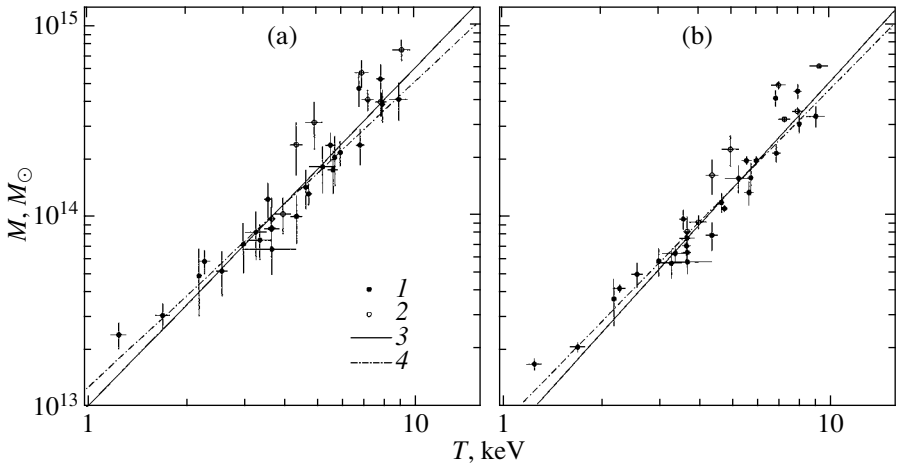

Fig. 1. *1*—Correlation between cluster temperature and gas mass $M_{324}^{\rm gas}$ (a) and $M_{500}^{\rm gas}$ (b), *2*—data for the highly asymmetric clusters A1367, A2142, A2147, A2256, A3266, A3376, A3395, and A3667, *3*—a power-law fit for the complete sample, and *4*—only for symmetric clusters.

where $x = r/r_{\rm core}$ and k is the normalization factor. We took $r_{\rm core}$ to be 250 kpc (Bahcall 1975). Since the interpolation is performed at $r \gg r_{\rm core}$, the exact value of $r_{\rm core}$ is of no importance.

Figure 2 shows the inferred correlation, which can be fitted by the formula

$$\log L[L_\odot] = 2.5 + 0.72 \log M_{324}^{\rm gas}[M_\odot]. \qquad (3)$$

Formula (3) can be used to estimate the optical luminosity of any cluster. Based on the relation $M_* = \alpha L_{\rm opt}$ and the King profile, we can easily determine the mass of stars at any radius. The numerical value of α was taken to be $6M_\odot/L_\odot$, which corresponds to the average stellar population in a typical mixture of elliptical and spiral galaxies in clusters (Arnaud *et al.* 1992).

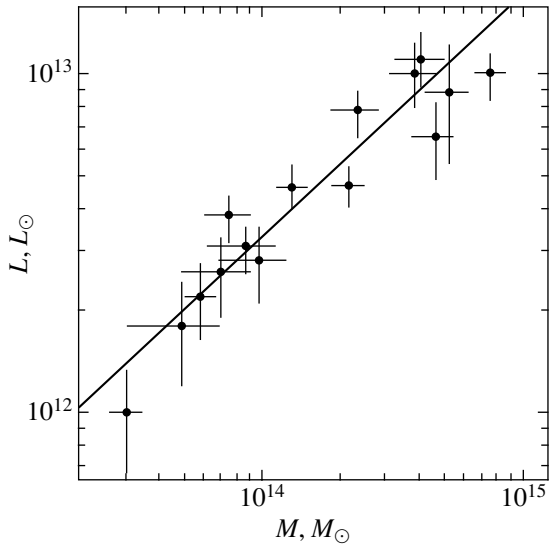

Fig. 2. Correlation between optical luminosity and gas mass M_{324}.

The baryon mass profile was determined by adding up the gas mass profile and the estimated stellar mass profile. We assigned an uncertainty of 30% to the stellar mass, which conservatively includes the uncertainty in α and in the fit (3).

Correlation between Baryon Mass and Temperature

Table 1 lists the baryon masses corresponding to overdensities of 324 and 500 (the corresponding radii r_{324} and r_{500} were recalculated with allowance for the stellar-mass contribution). Figure 3 shows the correlation between baryon mass and cluster temperature and its power-law fit. Table 2 gives numerical values of the best-fit parameters.

As with the $M_{\rm gas}$–T correlation, eliminating asymmetric clusters results in a flatter relation: $M_{324} \propto T^{1.49 \pm 0.11}$ compared to $M_{324} \propto T^{1.66 \pm 0.13}$.

When comparing the measured M–T correlation with theoretical models, a difference arises between the measured temperature and the temperature implied in the theory. More specifically, whereas measurements yield a temperature averaged with plasma emissivity, the theory generally operates with a mass-averaged temperature. Since the emissivity is $\varepsilon \propto \rho^2$, $\langle T_{\rm mass} \rangle$, and $\langle T_{\rm em} \rangle$ are generally not equal for nonisothermal clusters. However, if the temperature profiles are self-similar [observational evidence for similarity of the temperature profiles can be found in Markevitch *et al.* (1999)], then the $T_{\rm mass}/T_{\rm em}$ ratio is constant for clusters and the logarithmic slope of the M–T correlation then does not depend on which

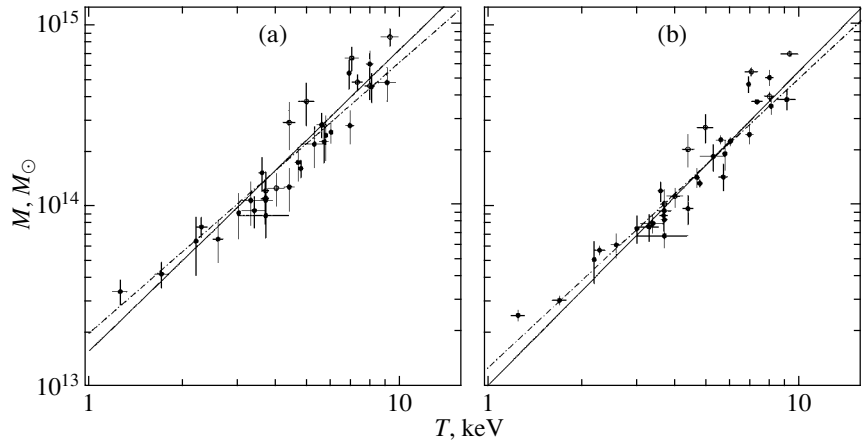

Fig. 3. Correlation between cluster temperature and baryon mass M_{324} (a) and M_{500} (b). The notation is the same as in Fig. 1.

of the temperatures is used. If, alternatively, the temperature profiles are not self-similar, the slope can be different, depending on which of the temperatures is used. Nevertheless, since most present studies of the temperature profiles show that the clusters are either isothermal or self-similar (Markevitch *et al.* 1999; Arnaud *et al.* 2001), the slopes inferred by using $T_{\rm mass}$ and $T_{\rm em}$ cannot differ greatly from each other.

DISCUSSION

The theory of cluster formation predicts the following correlation between total mass and intracluster gas temperature: $M \propto T^{3/2}$ (see, e.g., Lilje 1992). Hence, assuming that $f_{\rm bar}$ is constant and that most of the baryons are concentrated in hot gas, it follows that there is a correlation between X-ray luminosity and cluster temperature in the form $L_x \propto T^2$. However, the observed L_x–T correlation has long been known to be different: $L_x \propto T^3$ (see, e.g., David *et al.* 1993). Therefore, one might also expect deviations from the predicted $M_{\rm gas}$–T correlation (and, possibly, from the baryon mass $M_{\rm bar}$–temperature correlation).

So far, few experimental studies of the $M_{\rm gas}$–T relation have been carried out. The measurements of Mohr *et al.* (1999), $M_{\rm gas} \propto T^{2.0 \pm 0.2}$, and Vikhlinin *et al.* (1999), $M_{\rm gas} \propto T^{1.7 \pm 0.13}$, are statistically most accurate. These actually deviate from the theoretically expected relation. However, our data yield the relations $M_{\rm gas} \propto T^{1.6-1.7}$ and $M_{\rm bar} \propto T^{1.5-1.6}$, in good agreement with the theory. The probable causes of the discrepancy between our results and previous measurements should be discussed:

(1) We used a statistically complete sample of clusters selected from extensive X-ray catalogs by using well-defined restrictions on the observed flux and redshift. In contrast, Vikhlinin *et al.* (1999) selected the cluster only by the quality of the available ROSAT data; the selected clusters must be azimuthally symmetric. The cluster sample in Mohr *et al.* (1999) is more representative. However, it was drawn from the previous cluster catalog by Edge *et al.* (1990) with inaccurate flux measurements and without redshift restrictions.

(2) The cluster mass does not tend to any constant limit for $r \to \infty$. Therefore, the choice of the radius within which the mass is measured is of critical importance. For this purpose, Mohr *et al.* (1999) used the virial radius of the cluster estimated from its observed temperature ($r \propto \sqrt{T}$). Consequently, the mass and temperature in their approach are not completely independent, which can distort the observed M–T correlation. In contrast, our M and T measurements, like those of Vikhlinin *et al.* (1999), are independent. Our exponent in the M–T correlation is closer to that obtained by Vikhlinin *et al.* (1999), suggesting that the hidden relation between M and T actually plays a role in Mohr *et al.* (1999).

(3) Here, we attempted to take into account the contribution of stars to the cluster baryon mass, which was completely ignored in previous studies. Although the stars contribute a mere 10–30% to the total baryon mass, their allowance changes the exponent in the M–T relation, making it very close to the theoretical value.

(4) Finally, note that here, we used more accurate measurements of the cluster temperature, which slightly reduced the observed scatter in the M–T relation.

Presently, there are two major competing hypotheses that explain the deviations of the observed L_x–T relation from the relation predicted by the similarity theory of cluster formation. The first hypothesis postulates that the intracluster medium was heated

up at the epoch preceding gravitational collapse, which results in a reduced baryon fraction in low-mass clusters (see references in Ponman *et al.* 1999). The second hypothesis is based on the fact that a considerable fraction of the cluster intracluster medium turns into stars through radiative cooling and thus ceases to contribute to the X-ray radiation (Bryan 2000; Vojt and Bryan 2001).

These hypotheses predict different relations for the correlation between baryon mass and cluster temperature. Thus, for example, Bryan's model preserves the self-similar prediction $M_{\rm bar} \propto T^{3/2}$, but at the same time predicts a steeper temperature dependence for $M_{\rm gas}$. At the same time, in the model with heating of the intracluster medium, the predicted temperature dependence of $M_{\rm bar}$ changes: $M_{\rm bar} \sim T^2$. Therefore, our results are more consistent with the predictions of the model by Bryan (2000), which is based on radiative cooling of gas in clusters.[2]

In conclusion, note that the match between the measured $M_{\rm bar}$–T relation and the theoretically predicted relation for the *total* mass provides circumstantial evidence that the assumption of constant $f_{\rm bar}$ on which our subsequent studies are based is correct.

ACKNOWLEDGMENTS

This work was supported by the Russian Foundation for Basic Research (project no. 00-02-17124) and the Program "Astronomy: Nonstationary Astronomical Objects" of the Russian Academy of Sciences.

REFERENCES

1. M. Akritas and M. Bershady, Astrophys. J. **470**, 706 (1996).
2. S. Allen and A. Fabian, Mon. Not. R. Astron. Soc. **297**, L57 (1998).
3. M. Arnaud, R. Rothenflug, O. Boulade, *et al.*, Astron. Astrophys. **254**, 49 (1992).
4. M. Arnaud, D. Neumann, N. Aghanim, *et al.*, Astron. Astrophys. **365**, 80 (2001).
5. N. Bahcall, Astrophys. J. **198**, 249 (1975).
6. T. Beers, M. Geller, J. Huchra, *et al.*, Astrophys. J. **283**, 33 (1984).
7. E. Blanton, C. Sarazin, B. McNamara, and M. Wise, Astrophys. J. Lett. **558**, L15 (2001).
8. H. Bohringer, W. Voges, J. Huchra, *et al.*, Astrophys. J., Suppl. Ser. **129**, 435 (2000).
9. G. Bryan, Astrophys. J. Lett. **544**, L1 (2000).
10. S. Burles, K. Nollett, and M. Turner, Astrophys. J. Lett. **552**, L1 (2001).
11. A. Cavaliere and R. Fusco-Femiano, Astron. Astrophys. **49**, 137 (1976).
12. L. David, A. Slyz, C. Jones, *et al.*, Astrophys. J. **412**, 479 (1993).
13. S. de Grandi, H. Bohringer, L. Guzzo, *et al.*, Astrophys. J. **514**, 148 (1999).
14. H. Ebeling, A. Edge, S. Allen, *et al.*, Mon. Not. R. Astron. Soc. **318**, 333 (2000).
15. A. C. Edge, G. C. Stewart, A. C. Fabian, and K. A. Arnaud, Mon. Not. R. Astron. Soc. **245**, 559 (1990).
16. A. Evrard, C. Metzler, and J. Navarro, Astrophys. J. **469**, 494 (1996).
17. A. Fabian, E. Hu, L. Cowie, and J. Grindlay, Astrophys. J. **248**, 47 (1981).
18. D. Fabricant, M. Lecar, and P. Gorenstein, Astrophys. J. **241**, 552 (1980).
19. A. Finoguenov, T. Reiprich, and H. Bohringer, Astron. Astrophys. **368**, 749 (2001).
20. Y. Fukazawa, K. Makishima, T. Tamura, *et al.*, Publ. Astron. Soc. Jpn. **50**, 187 (1998).
21. D. Horner, R. Mushotzky, and C. Scharf, Astrophys. J. **520**, 78 (1999).
22. V. Hradecky, C. Jones, R. Donnelly, *et al.*, Astrophys. J. **543**, 521 (2000).
23. A. Jenkins, C. Frenk, S. White, *et al.*, Mon. Not. R. Astron. Soc. **321**, 372 (2001).
24. J. Kaastra, C. Ferrigno, T. Tamura, *et al.*, Astron. Astrophys. **365**, 99 (2001).
25. P. Lilje, Astrophys. J. Lett. **386**, L33 (1992).
26. M. Markevitch, W. Forman, C. Sarazin, and A. Vikhlinin, Astrophys. J. **503**, 77 (1998).
27. M. Markevitch, A. Vikhlinin, W. Forman, and C. Sarazin, Astrophys. J. **527**, 545 (1999).
28. J. Mohr, B. Mathiesen, and A. Evrard, Astrophys. J. **517**, 627 (1999).
29. T. Ponman, D. Cannon, and J. Navarro, Nature **397**, 135 (1999).
30. W. H. Press, S. A. Teukolsky, W. T. Vetterling, and B. P. Flannery, *Numerical Recipes in FORTRAN* (Cambridge Univ. Press, London, 1992), p. 686.
31. J. Raymond and B. Smith, Astrophys. J., Suppl. Ser. **35**, 419 (1977).
32. C. Snowden, D. McCammon, D. Burrows, and J. Mendenhall, Astrophys. J. **424**, 714 (1994).
33. A. Vikhlinin, W. Forman, and C. Jones, Astrophys. J. **525**, 47 (1999).
34. G. Vojt and G. Bryan, Nature **414**, 425 (2001).
35. S. White, J. Navarro, A. Evrard, and C. Frenk, Nature **366**, 429 (1993).
36. D. White, Mon. Not. R. Astron. Soc. **312**, 663 (2000).

Translated by A. Dambis

[2]Note, nevertheless, that quantitatively, our measurements do not completely agree with Bryan's model: whereas our measured $M_*/M_{\rm gas}$ ratio is 0.l–0.2, Bryan used $M_*/M_{\rm gas} =$ 0.5–1 in his computations.

Astronomy Letters, Vol. 28, No. 6, 2002, pp. 373–385. Translated from Pis'ma v Astronomicheskiĭ Zhurnal, Vol. 28, No. 6, 2002, pp. 425–439.

The Crab Nebula: Interpretation of Chandra Observations

S. V. Bogovalov* and D. V. Khangoulyan

Moscow Institute of Engineering Physics (Technical University), Kashirskoe sh. 31, Moscow, 115409 Russia

Received January 27, 2002

Abstract—We interpret the observed X-ray morphology of the central part of the Crab Nebula (torus + jets) in terms of the standard theory by Kennel and Coroniti (1984). The only new element is the inclusion of anisotropy in the energy flux from the pulsar in the theory. In the standard theory of relativistic winds, the Lorentz factor of the particles in front of the shock that terminates the pulsar relativistic wind depends on the polar angle as $\gamma = \gamma_0 + \gamma_m \sin^2\theta$, where $\gamma_0 \sim 200$ and $\gamma_m \sim 4.5 \times 10^6$. The plasma flow in the wind is isotropic. After the passage of the pulsar wind through the shock, the flow becomes subsonic with a roughly constant (over the plerion volume) pressure $P = \frac{1}{3}n\epsilon$, where n is the plasma particle density and ϵ is the mean particle energy. Since $\epsilon \sim \gamma mc^2$, a low-density region filled with the most energetic electrons is formed near the equator. A bright torus of synchrotron radiation develops here. Jet-like regions are formed along the pulsar rotation axis, where the particle density is almost four orders of magnitude higher than that in the equatorial plane, because the particle energy there is four orders of magnitude lower. The energy of these particles is too low to produce detectable synchrotron radiation. However, these quasi-jets become comparable in brightness to the torus if additional particle acceleration takes place in the plerion. We also present the results of our study of the hydrodynamic interaction between an anisotropic wind and the interstellar medium. We compare the calculated and observed distributions of the volume emissivity of X-ray radiation. © *2002 MAIK "Nauka/Interperiodica".*

Key words: *plasma astrophysics, hydrodynamics and shock waves*

INTRODUCTION

The Crab Nebula is one of the most interesting and best-studied sources in the sky. This object was observed over a wide wavelength range: from radio to gamma-rays with a photon energy of 50 TeV (Aharonian 2000; Hester 1998; Shklovskii 1968). However, advances in observational astronomy provide new data on the Crab Nebula. In the last decade, progress in the technology of X-ray telescopes has allowed the Crab Nebula to be observed with an angular resolution comparable to the angular resolution of ground-based optical telescopes. As would be expected, this gave completely new information on the structure of the central part of the nebula. The data obtained on the Chandra X-ray observatory arouse particular interest.

The Chandra observations show that the central part of the nebula consists of two components in the soft X-ray emission: a toroidal structure surrounding the pulsar PSR 0531 + 21 and two jet-like features located perpendicular to the torus and emerging from the pulsar (Weisskopf *et al.* 2000). Interestingly, such a structure of the plerion central region is also observed in the Vela pulsar (Pavlov *et al.* 2001) and in the supernova remnant G0.9 + 1 (Gaensler 2001). In this paper, we focus our attention on the Crab Nebula primarily because of the parameters of the relativistic plasma flow (pulsar wind) from this pulsar. Weak magnetization of the wind from PSR 0531 + 21 allows the problem of its interaction with the interstellar medium to be simplified to an extent that the intensity distribution of synchrotron radiation in the plerion can be easily estimated and compared with the observed one.

The first impression that arises when studying the Chandra images of the Crab Nebula is that the toroidal structure surrounding the pulsar suggests the presence of an accretion disk around the nebula. However, this interpretation of the observed picture is incorrect for obvious reasons. First, there is no independent evidence for the existence of a second companion and an accretion disk around the Crab pulsar. Second, the characteristic size of the toroidal structure itself, $\sim 10^{18}$ cm, rules out the possibility of the disk interpretation of the observed picture.

The situation with the jet-like features is more complicated. Jets are observed from many Galactic YSOs (Livio 1999), SS 433 (Cherepashchuk 1998), superluminal sources (Mirabel and Rodrigues 1998)

*E-mail: bogoval@axpk40.mephi.ru

and AGNs (Urri and Padovani 1995). A direct analogy between the jets from these objects and those observed in the Crab Nebula suggests itself. The assumption that the pulsar itself ejects collimated plasma flows seems reasonable enough. However, it is most likely incorrect.

The Crab Nebula is a typical plerion—a bubble of relativistic particles frozen in a magnetic field. This bubble is formed when the flow of supersonic relativistic plasma (pulsar wind) ejected by the pulsar interacts with the interstellar medium. Since the wind itself is cold, it remains unobservable thus far (see, however, Bogovalov and Aharonian 2000). After passing through the wind-terminating shock, the particles are isotropized and begin to emit synchrotron photons over a wide electromagnetic spectral range, producing the observed plerion radiation; hence the fundamental difference between the jet-like features observed in the nebula and the actual jet flows observed in the Universe from other objects. The latter are the supersonic collimated flows ejected from the source. They are characterized by termination when interacting with the interstellar medium to produce a shock and the so-called lobes (Ferrari *et al.* 1996). The jet-like features themselves in the Crab Nebula are formed behind the shock that terminates the pulsar wind. The plasma flow in them is definitely subsonic. Therefore, the physics of this phenomenon undoubtedly differs from the physics of the processes that give rise to astrophysical jets.

Since the observed structures in the Crab Nebula result from the interaction of the pulsar wind with the ambient medium, the pattern of this interaction must be studied to understand their nature. The interaction of the wind from the Crab pulsar with the interstellar medium has been analyzed by many authors. Rees and Gunn (1974) and Kennel and Coroniti (1984) first gave important constraints on the parameters of the pulsar wind immediately in front of the shock. The calculated plerion expansion velocity, luminosity, and synchrotron radiation spectrum (from optical wavelengths to X-rays) agree with the observed ones if the wind consists of electrons and positrons with a Lorentz factor of $\sim 3 \times 10^6$ and if almost all of the pulsar rotational losses are transformed into the particle kinetic energy so that the ratio of the electromagnetic energy flux to the particle kinetic energy flux is $\sigma = 3 \times 10^{-3}$. For such wind parameters, we can also naturally explain the gamma-ray emission from the Crab Nebula above 10 GeV, which is generated by the inverse Compton scattering of the same electrons that generate the synchrotron radiation (Atoyan and Aharonian 1996; de Jager and Harding 1992).

The success of the theory by Kennel and Coroniti (1984) was achieved through a significant simplification of the problem. This theory assumes the problem to be spherically symmetric. As long as the analysis was restricted to the integrated characteristics of the radiation from the Crab Nebula (spectra, luminosity), this limitation was not fundamental in nature. However, the observed X-ray morphology of the Crab Nebula cannot be explained in terms of this theory. Clearly, the Crab Nebula is not spherically symmetric. The more realistic pattern of interaction between an anisotropic pulsar wind and the interstellar medium must be considered. Here, we made the first step in solving this problem. At this stage, we do not set the goal of developing a full-blown theory of the interaction between an anisotropic, magnetized pulsar wind and a homogeneous interstellar medium. This is not yet possible. Here, we determine the pattern of pulsar-wind anisotropy by using the results that have been obtained in pulsar physics in recent years. We also perform a semiquantitative analysis of the result of the interaction between such a wind and the interstellar medium, including an estimation of the synchrotron radiation. In the end, we wish to understand whether the level of anisotropy in pulsar winds that follows from the pulsar theory is enough to explain, at least in general terms, the structure of the central part of the Crab Nebula observed on the Chandra observatory.

THE PULSAR WIND FROM PSR 0531 + 21

The integrated characteristics of the Crab Nebula can be naturally explained in terms of the theory by Kennel and Coroniti (1984) if the wind magnetization parameter is $\sigma = 3 \times 10^{-3}$ and the wind Lorenz factor is $\gamma \sim 3 \times 10^6$ immediately in front of the shock (Kennel and Coroniti 1984), although other wind parameters cannot be completely ruled out either (Begelman 1998). The Kennel–Coroniti theory naturally accounts for the source spectrum over an unprecedentedly wide wavelength range, from optical to hard gamma-ray emission (fifteen orders of magnitude in wavelength!). No theory in astrophysics can boast a similar success. However, there is one problem in this theory that spoils the overall picture. It is not yet clear how the pulsar PSR 0531 + 21 produces the relativistic wind with such parameters. This remains one of the key puzzles in the physics of radio pulsars.

The problem is that all the currently available theories of particle acceleration and plasma formation in pulsar magnetospheres [the polar-cap theory (Arons 1983; Daugherty and Harding 1996) or the outer-gap theory (Romani 1996; Cheng *et al.* 2000)] are capable of explaining how the dense $e^{\pm}$ plasma that produces a relativistic particle wind is formed. However, this plasma carries a negligible fraction

($\sim 10^{-4}$) of all rotational losses from the Crab pulsar. The entire energy flux from the pulsar is concentrated in the electromagnetic field carried away by the wind, which corresponds to the wind magnetization parameter $\sigma \sim 10^4$. The wind itself has a modest Lorentz factor $\sim$200 near the radio-pulsar light cylinder (Daugherty and Harding 1996). It is yet to be clarified through which processes almost the entire electromagnetic energy flux is transformed into the wind-particle kinetic energy on the way from the light cylinder to the shock front, although substantial efforts were spared to solve this problem (Coroniti 1990; Lyubarsky and Kirk 2001).

There is no need to know the wind acceleration mechanism to determine the energy-flux distribution in the wind. The fact that the conservation of the energy flux in the wind holds in any case is suffice. The point is that the electromagnetic energy flux in the winds from radio pulsars propagates along streamlines. The plasma kinetic energy flux also propagates along these streamlines. This conclusion is based on MHD models of the winds from axisymmetrically rotating objects (Okamoto 1978). However, it has recently been shown to be also valid for obliquely rotating objects where the flow beyond the light cylinder is concerned (Bogovalov 1999). This ensures that the total energy flux per particle is conserved along a given streamline. The kinetic energy flux per particle, in units of mc^2, is γ. The electromagnetic energy flux per particle, in units of mc^2, is

$$s = \frac{c}{4\pi}[E \times B]/(nvmc^2\gamma), \qquad (1)$$

where E is the electric field, B is the magnetic field, n is the particle density in the intrinsic frame of reference, and v is the wind velocity. The sum $\gamma + s$ depends on the streamline but is conserved along it. It follows from the solution of the problem on the structure of the wind from an oblique rotator (Bogovalov 1999) that the energy flux in the wind sufficiently far from the light cylinder may be considered to be azimuthally symmetric, although the electromagnetic field itself is not azimuthally symmetric in this case (see Bogovalov (1999) for details). In this notation, the magnetization parameter is $\sigma = s/\gamma$. The conservation of the total energy flux ensures that

$$\gamma_0 + s_0 = \gamma + s. \qquad (2)$$

The subscript '0' marks the values near the light cylinder. Since $s \ll \gamma$ in front of the shock that terminates the pulsar wind, the Lorentz factor of the preshock plasma may be assumed to be $\gamma = \gamma_0 + s_0$. Thus, the dependence of the particle energy on the streamline along which the particles move is determined by their initial energy and the initial distribution of the electromagnetic energy flux. We make the only assumption. Assume that the initial distribution of the electromagnetic energy flux does not depend on (or is almost independent of) the wind acceleration. This assumption holds true in all cases if the wind is accelerated sufficiently far from the light cylinder in the supersonic flow region. Then, the field distribution in the magnetosphere and, hence, the initial electromagnetic energy flux do not depend on what happens downstream of the magnetosonic surface. This is because no MHD signal can penetrate from the supersonic flow region into the subsonic flow region and affect the flow in this region. If this is the case, then it will suffice to determine s_0, provided that there is no acceleration.

Numerical and analytical calculations of the relativistic plasma flow show that the plasma magnetic collimation is negligible for Lorentz factors $\gamma >$ 200 (Beskin 1998; Bogovalov and Tsinganos 1999; Bogovalov 2001a). The pulsar wind may be assumed to spread out radially. Since the relation $E = \frac{r\sin\theta\Omega}{c}B_p$ (Mestel 1968), where r is the distance to the pulsar, θ is the polar angle, Ω is the pulsar angular velocity, and B_p is the poloidal magnetic field in the wind, holds between the electric field in the wind and the poloidal magnetic field, the condition for the magnetic field being frozen in the plasma $E + \frac{1}{c}[E \times B] = 0$ takes the form

$$r\sin\theta\Omega B_p + B_\varphi v_p = v_\varphi B_p. \qquad (3)$$

At $r \gg c/\Omega$, the plasma angular velocity tends to zero, because the angular momentum of the plasma particles ($r\sin(\theta)v_\varphi$) is limited above. We then derive a simple expression for the toroidal field in the wind far from the pulsar, $B_\varphi = \frac{r\sin\theta\Omega}{v_p}B_p$. Therefore, the electromagnetic energy flux per particle (in units of mc^2) is

$$s_0 = \sin^2\theta\left(\frac{\Omega r}{v_p}\right)^2\frac{B_p^2}{4\pi n_0 mc^2\gamma_0}. \qquad (4)$$

We see that when the relativistic wind spreads out radially and uniformly, the Lorentz factor γ_1 of the preshock wind particles must have a latitude dependence of the form

$$\gamma_1 = \gamma_0 + \gamma_m\sin^2\theta, \qquad (5)$$

where $\gamma_m = (\frac{\Omega r}{v_p})^2\frac{B_p^2}{4\pi n_0 mc^2\gamma_0}$. This is the maximum Lorentz factor of the preshock wind particles. To be consistent with the theory by Kennel and Coroniti (1984), it must be of the order of 3×10^6.

Note that expression (5) for the particle Lorentz factor immediately follows from the MHD theory of

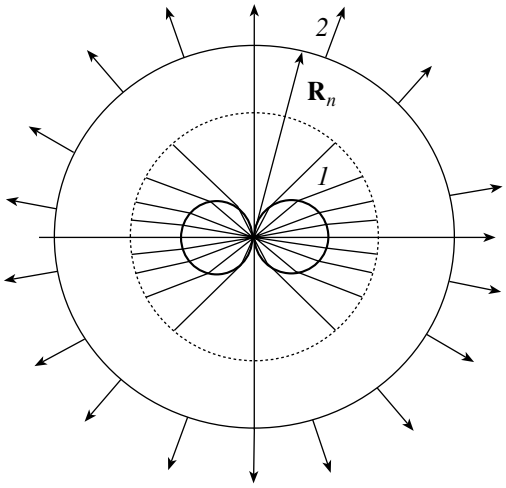

Fig. 1. A schematic image of the interaction between the pulsar wind and the interstellar medium. Because of the increase in the energy flux density in the wind toward the equator, the shock (*1*) takes the form of a torus. The streamlines bend at the shock front and are pressed to the equator. The region between the shock and the contact discontinuity (*2*) is filled with relativistic particles emitting synchrotron radiation. The dotted line marks the $r \ll R_n$ region, where the plasma flow may be considered to be quasi-steady

magnetized winds from rotating objects and is almost model-independent. It only assumes that the particle flux from the pulsar is isotropic. Clearly, this assumption does not severely restrict the range of applicability of our results. For the standard parameters $\gamma_0 = 200$ and $\gamma_m \sim 3 \times 10^6$, the Lorentz factor changes with latitude by four orders of magnitude. Even if the particle flux changes with latitude by several times (or several tens of times), this does not change the overall dependence. Anyway, the most energetic particles will be near the equator and their Lorentz factor will be higher than the Lorentz factor of the particles at the rotation axis by several orders of magnitude.

Below, for our calculations, we assume the wind flow to be radial with an isotropic mass flux. The plasma density in the intrinsic frame of reference in such a wind is

$$n_1 = \frac{\dot{N}}{4\pi v_p r^2 \gamma}. \quad (6)$$

Here, $\dot{N}$ is the rate of particle injection into the nebula. The toroidal magnetic field has the distribution

$$B_\varphi = \frac{B_0 r_0 \sin\theta}{r}. \quad (7)$$

The quantity B_0 can be determined from the condition $\sigma = 3 \times 10^{-3}$. We ignore the poloidal magnetic field, because it is much weaker than the toroidal magnetic field ahead of the shock front. The plasma Lorentz factor is given by expression (5). Our objective is to determine (at least qualitatively) how a wind with the above parameters interacts with a homogeneous ambient interstellar medium.

THE APPROXIMATIONS

The problem of the interaction between a highly anisotropic, magnetized relativistic wind and a homogeneous ambient medium has no analytic solution. Even obtaining a numerical solution seems problematic so far. Below, we make two reasonable simplifications that will allow us to answer the questions of interest by using simple mathematics.

(1) *The approximation of a hydrodynamic interaction.* In the special case of the Crab Nebula, as a first approximation, we may disregard the magnetic-field effect on the postshock plasma dynamics. This approximation seems reasonable, because the pulsar wind from PSR 0531 + 21 is weakly magnetized. Recall that the ratio of the preshock Poynting flux to the plasma kinetic energy flux is $\sigma = 3 \times 10^{-3}$. Although the magnetic field increases in strength by a factor of 3 after the shock passage, the ratio of magnetic pressure to plasma pressure is small up to distances approximately equal to five shock radii (see Kennel and Coroniti 1984). Further out, the magnetic pressure is higher than the plasma pressure and it cannot be ignored. However, the region of $5r_{\rm sh}$ completely suits us. It is in this region that the most interesting features of the central part of the Crab Nebula are formed: the X-ray torus and the jet-like features. Therefore, below, the wind interaction is considered as a purely hydrodynamic one. We will determine the magnetic-field evolution from the induction equation with a given distribution of the plasma velocity field. Note that although the magnetic-field effect on the plasma dynamics immediately behind the shock wave is marginal, Lyubarsky (2002) attempts to explain the observed jets in the Crab Nebula as resulting from a magnetic compression of the wind after the shock wave. Below, we show that these jets are formed in the hydrodynamic approximation without any involvement of the magnetic field.

(2) *The quasi-stationary approximation.* Strictly speaking, the interaction of a supersonic wind from the central source with the interstellar medium is not stationary. It is schematically shown in Fig. 1. The source continuously injects new particles into the nebula and the nebula size increases with time. However, in a bounded region of space near the shock, the flow may be considered to be steady, provided that the nebula size is much larger than the characteristic size of the shock. This is easy to understand from simple considerations. Assume that the source injects particles with characteristic

energy ϵ into the nebula at a rate $\dot{N}$. The nebula size R_n at constant external pressure $P_{\rm ext}$ is then determined by the relation $\dot{N}t\epsilon/(4\pi/3R_n^3) = p_{\rm ext}$, where t is the source operation time. We see from this relation that the nebula radius increases as $t^{1/3}$. This means that the velocity of the nebula outer rim decreases with time; therefore, the entire flow may be considered in the limit $t \to \infty$ as steady with the boundary condition at infinity $v \to 0$ for $r \to \infty$ and $P = P_{\rm ext}$. Thus, the condition for applicability of the quasi-stationary approximation is $R_n \gg r_{\rm sh}$, where $r_{\rm sh}$ is the characteristic radius of the shock front. For the Crab Nebula, $R_n \approx 2$ pc and the shock radius is $r_{\rm sh} = 0.1$ pc (Kennel and Coroniti 1984). Consequently, the postshock flow for the Crab Nebula within $5r_{\rm sh}$ may actually be considered to be steady.

THE INTERACTION OF A HIGHLY ANISOTROPIC WIND WITH THE INTERSTELLAR MEDIUM

Basic Simplifications

The problem of the interaction between a supersonic, highly anisotropic plasma flow and a homogeneous medium has no exact solution so far. Therefore, below, to estimate the observed effects that must arise during such an interaction, we proceed as follows: first, we use a highly simplified interaction model to calculate the volume luminosity of the plerion produced by a Crab-type pulsar; subsequently, we qualitatively consider how our simplifications affect the results of our calculations by using, in particular, the results obtained for weak anisotropy in Appendix A.

We use the following simplifications to estimate the volume luminosity of the Crab Nebula:

(1) Since the postshock plasma flow is subsonic, with the plasma velocity tending to zero when moving downstream of the shock, the plasma density along a streamline may be assumed to be constant (Landau and Lifshitz 1986). The subsonic motion also implies an approximate equality of the pressure in the plerion. Previously, Begelman (1992) used this approximation to describe the postshock flow. Let us estimate the accuracy with which these conditions may be considered to be satisfied in our specific case. The pressure variation in the plerion is $\Delta P/P \sim Wu^2/P$. Here, $W = 4P$ and $u \sim 1/\sqrt{8}$, because the plasma velocity is $v = \dfrac{1}{3}c$ immediately behind the shock and then rapidly decreases. Therefore, in the worst case, we have $\Delta P/P \sim 0.5$. This error completely suits us, because below, we are concerned with the variations in mean particle energy ϵ and plasma density n across a streamline, which are four orders of magnitude; the pressure is related to these quantities by $P = \dfrac{1}{3}n\epsilon$. Against the background of such variations, the pressure variations of 50% are of no fundamental importance.

(2) We assume the postshock streamlines to remain radial without bending at the shock and use the conditions for a perpendicular shock to determine the postshock plasma parameters.

The Shape of the Shock Front

To determine the shape of the shock front, we use the shock-adiabat relation (A.18) for an oblique shock wave. After the passage of the shock front, the plasma on each streamline adiabatically decelerates; far from the shock front, its velocity tends to zero and the plasma pressure comes into equilibrium with the external pressure $P_{\rm ext}$. The relationship between the plasma parameters immediately after the shock and $P_{\rm ext}$ is given by the Bernoulli equation for a relativistic plasma

$$4\gamma_2\frac{P_2}{n_2} = 4\frac{P_{\rm ext}}{n_\infty} = \gamma_1 mc^2. \qquad (8)$$

Here, we use the constancy of the Bernoulli integral at the shock front and the relativistic-plasma approximation $e = 3p$, which holds good behind the shock. Below, the subscripts '1' and '2' denote the preshock and postshock quantities, respectively.

It is easy to find from these relations and from the adiabatic flow condition (A.5) that

$$\frac{P_{\rm ext}}{\gamma_1^2 n_1 mc^2} = \frac{3}{2}\left(\frac{3}{\sqrt{8}}\right)^{\frac{\delta}{\delta-1}}\gamma_{||}^{\frac{2-\delta}{\delta-1}}. \qquad (9)$$

The location of the shock front could be determined from this equation if $\gamma_{||}$ were known. Since the problem is azimuthally symmetric, this quantity is known only at points on the equatorial plane and on the rotation axis. The shock front crosses them at a right angle. Below, we consider a simplified case by assuming, for simplicity, that $\gamma_{||} = 1$ everywhere. We then obtain for the shock radius

$$r_{\rm sh} = \sqrt{\frac{3}{2}\left(\frac{3}{\sqrt{8}}\right)^{\frac{\delta}{\delta-1}}\frac{\gamma_1 mc^2\dot{N}}{4\pi P_{\rm ext}c}}. \qquad (10)$$

In the limit $\gamma_m \gg \gamma_0$ of interest, the shock radius may be assumed to be $r_{\rm sh} = r_{\rm eq}|\sin\theta|$ everywhere, except for a narrow interval of angles $\theta < \sqrt{\gamma_0/\gamma_m}$. This implies that the shock front is generally a torus whose cross section is a couple of contacting circumferences with the centers on the equatorial plane in the middle of the distance $r_{\rm eq}$ from the source to the shock.

To estimate the error in using everywhere the approximation $\gamma_{||} = 1$, we must solve the problem

more accurately. Our analysis, which is beyond the scope of this paper, shows that the shock front lies at slightly larger distances than (10). In addition, a system of two shocks is formed near the axis for a highly anisotropic wind. Nevertheless, expression (10) gives an error in the shock radius within 15%. In this paper, such an accuracy is admissible.

The Formation of a Toroidal Structure

As follows from the condition of a constant density along the postshock streamline, the plasma velocity v_p on each streamline behaves as

$$v_p = \frac{1}{3}c\left(\frac{r_{\rm sh}(\theta)}{r}\right)^2, \qquad (11)$$

where $r_{\rm sh}(\theta)$ is the distance from the pulsar to the shock location at a given angle θ. This dependence on r follows from the conservation of mass flux for radial plasma motion.

On a given streamline, the dependence of the magnetic field on r and θ follows from the frozen-in condition. According to this condition, $B/nr = {\rm const}$ on a streamline (Landau and Lifshitz 1982). For the preshock magnetic field, we use the condition

$$\frac{(B_0\frac{r_0}{r_{\rm sh}}\sin\theta)^2}{4\pi n_1 mc^2\gamma_1^2} = \sigma\frac{\gamma_m\sin^2\theta}{\gamma_1}. \qquad (12)$$

It implies that the ratio of the Poynting flux density to the plasma kinetic energy flux density is everywhere equal to the same value σ, except for a narrow region near the rotation axis where the toroidal field must vanish. We inserted the additional factor $\frac{\gamma_m\sin^2\theta}{\gamma}$ in the right-hand part of Eq. (12) to take into account this circumstance. It follows from expression (9) that the preshock magnetic field is

$$B_1 = B_0\frac{r_0}{r_{\rm sh}}\sin\theta = \sqrt{4\sigma\pi\gamma_m\gamma_1 n_1 mc^2}\sin\theta. \quad (13)$$

Given that the magnetic field increases in strength by a factor of 3 after the passage of a strong shock, we obtain

$$B_2 = 3\sqrt{(\frac{4\pi\sigma\gamma_m}{\gamma}\frac{2}{3}\left(\frac{\sqrt{8}}{3}\right)^{\frac{\delta}{\delta-1}}P_{\rm ext})}\sin\theta\frac{r}{r_{\rm sh}}. \quad (14)$$

At angles $\theta \gg \sqrt{\gamma_0/\gamma_m}$, the expression for the magnetic field takes the form

$$B_2 = B_{\rm eq}\frac{r}{r_{\rm sh}}, \qquad (15)$$

where $B_{\rm eq}$ is the postshock equatorial magnetic field. We see that the field immediately behind the shock is everywhere the same, except for a narrow region near the rotation axis. Outside this region, the field more rapidly increases with distance from the pulsar at high latitudes. The field linearly increases until the magnetic energy density becomes equal to the plasma energy density. Subsequently, the field begins to decrease with increasing r (Kennel and Coroniti 1984). The fact that the linear dependence extends to $5r_{\rm sh}$ (Kennel and Coroniti 1984), within which the toroidal structure is formed, will suffice.

To calculate the synchrotron radiation, we assume, as in Kennel and Coroniti (1984), that the following power-law particle spectrum is formed behind the shock:

$$F(\gamma, r = r_{\rm sh}) = A\left(\frac{\gamma}{\gamma_{\rm min}}\right)^{-\alpha} \times \eta(\gamma-\gamma_{\rm min})\eta(\gamma_{\rm max}-\gamma), \qquad (16)$$

where A is the normalization factor determined from the particle injection rate on a given streamline, $\gamma_{\rm min}$ is the minimum particle energy in the spectrum, $\gamma_{\rm max}$ is the maximum particle energy in the spectrum, and $\eta(x)$ is the step function equal to unity at $x \geq 1$ and zero at $x < 1$.

The mean energy of the chaotic particle motion in this spectrum must correspond to the mean postshock particle energy determined from the shock adiabat. It follows from this condition that

$$\gamma_{\rm min} = \frac{\gamma_1(\theta)}{\sqrt{2}}\frac{(\alpha-2)}{(\alpha-1)}. \qquad (17)$$

Here, we use the fact that although the cutoff energy of the spectrum, $\gamma_{\rm max} \approx 5\times10^9$ (Atoyan and Aharonian 1996), is finite, it is much larger than $\gamma_{\rm min} \leq 5\times10^5$.

The plasma moves behind the shock as a whole at velocity (11). The evolution of the particle spectrum during this motion is described by the transport equation

$$v_p\frac{\partial F}{\partial r} = -\frac{\partial}{\partial\gamma}\dot{\gamma}F. \qquad (18)$$

The rate of change in the Lorentz factor of the chaotic particle motion, $\dot{\gamma}$, is generally determined by synchrotron losses and plasma heating through adiabatic compression during the wind deceleration. In our case, the adiabatic changes in particle energy can reach 24% of the particle energy. However, we disregard these changes here, because this is a clear excess of the accuracy under our assumptions about the postchosk plasma dynamics.

The solution of Eq. (18), provided that the distribution function at the shock matches function (16), is

$$f(\gamma, r, \theta) = \frac{(1-\gamma G)^{(\alpha-2)}(\alpha-1)}{\gamma_{\rm min}} \qquad (19)$$

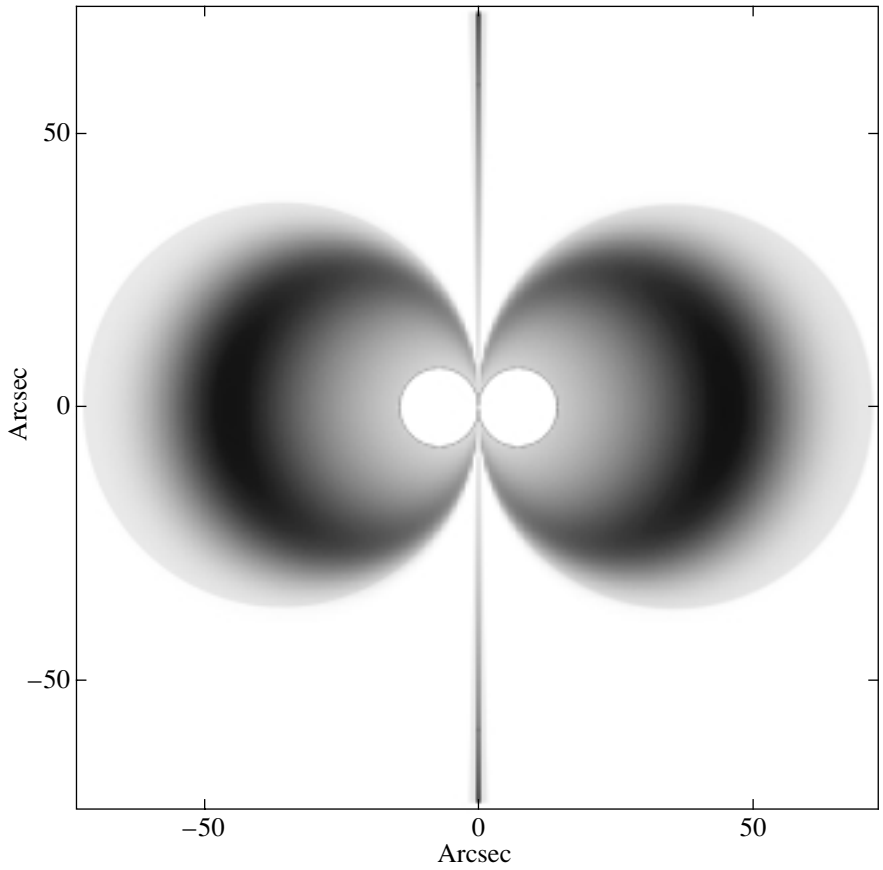

Fig. 2. The distribution of the volume emissivity of synchrotron radiation in the plerion produced by the wind from the pulsar PSR 0531 + 21. The cross section of the shock is similar in shape to two contacting circumferences. The shock location at the equator is taken to be 14″, in accordance with the observed location of the torus inner ring.

$$\times \left(\frac{\gamma}{\gamma_{\min}}\right)^{-\alpha} \eta\left(\frac{\gamma}{1-\gamma G} - \gamma_{\min}\right)$$
$$\times \eta\left(\gamma_{\max} - \frac{\gamma}{(1-\gamma G)}\right) n(r,\theta).$$

In this expression, the function

$$G(r,\theta) = \frac{2}{5} r_{\rm sh}(\theta) \left(\frac{e^2}{mc^2}\right)^2 \times \frac{B_{\rm eq}^2}{mc^2} \left(\left(\frac{r}{r_{\rm sh}(\theta)}\right)^5 - 1\right) \quad (20)$$

describes the degradation of the particle energy through synchrotron losses. The function $n(r,\theta)$ is the emitting-electron density in the observer's frame of reference. The electron density in the plerion on the streamline with θ follows from expression (6):

$$n(r,\theta) = \frac{3\dot{N}}{4\pi c r_{\rm sh}^2(\theta)}. \quad (21)$$

Here, we took into account the fact that the density at the shock increases by a factor of 3. The synchrotron flux is determined by the convolution of spectrum (19) with the spectral distribution of the radiation from an individual electron (Landau and Lifshitz 1973). The input parameters for our calculations are the particle injection rate $\dot{N} = 5 \times 10^{38}$ part. s^{-1}, the maximum Lorentz factor of the wind at the equator $\gamma_m = 4.5 \times 10^6$, and the shock location at the equator; we correlated the latter with the inner ring of the toroidal structure, which is located at $r_{\rm eq} = 4.3 \times 10^{17}$ cm corresponding to a distance of 14″ (Weisskopf *et al.* 2000). Actually, this implies that the external pressure $P_{\rm ext}$ was chosen so that the shock at the equator was located on the inner ring of the toroidal structure.

The results of our calculations are presented in Fig. 2. This figure shows the plerion volume luminosity at photon energy 400 eV, the characteristic energy at which the Chandra observations are carried out (Weisskopf *et al.* 2000). No integration along the line of sight was performed. All geometric sizes were reduced to the pulsar distance, 2 kpc. Here, only the plerion cross section in the poloidal plane is shown. We see that the spatial distribution of the volume

luminosity has the shape of a torus with the characteristic sizes corresponding to the observed ones. The radiation reaches the highest intensity at a distance of $\approx 40''$, where the second outer ring in the Crab Nebula is located. The intensity of the synchrotron radiation behind the shock is known to gradually rise (Kennel and Coroniti 1984). This rise results from a linear increase in the magnetic field behind the shock, which takes place only if the preshock wind was weakly magnetized. The further rapid decline in the radiation at distances $>60''$ is attributable to fast synchrotron electron cooling in the growing magnetic field. We see that although our calculations are definitely incorrect for $r > 5R_{\rm sh}$, this is of no importance. When the electrons reach this region, they have already cooled down to an extent that they do not produce detectable radiation in the Chandra spectral range.

In our calculations, we failed to obtain the bright inner toroidal ring. It may well be that this brightening cannot be explained in terms of magnetic hydrodynamics in principle and that it is attributable to the structure of a collisionless shock, which must be investigates separately (see Gallant 1992).

Across the equatorial plane, the agreement with the observed distribution is slightly worse. The distribution of the calculated brightness across the equator is broader than that of the observed one. It may well be that distributions (5)–(7) do not faithfully describe the preshock wind parameters. The energy and plasma fluxes in the wind may be more concentrated toward the equator than follows from the theory. In our view, however, it is too early to draw this conclusion. The observed disagreement may be entirely attributable to our approximations. We assumed the shock to be perpendicular to the streamline everywhere. This is not true outside the equatorial plane, where the shock inclination to the streamline decreases while $\gamma_{||}$ increases. As the angle of incidence of the shock decreases, the mean energy of the chaotic particle motion after the shock passage also decreases, as is clearly seen from the relation for the shock adiabat of an oblique relativistic shock. Therefore, the volume emissivity must decline with height above the equator faster than in our case.

We disregarded the fact that the streamlines must bend toward the equator at the shock, as is the case for weak anisotropy under consideration. Allowing for this circumstance will cause an increase in the brightness near the equator and its faster decrease under it. Finally, we assumed the streamlines after the shock passage to remain straight. In fact, as our calculations for low anisotropy show, the streamlines continue to approach the equator, at least in some preshock region, even after the shock passage. Thus, all our most important approximations used to estimate the volume luminosity of the plerion produced by the Crab pulsar lead to the same effect: a broader distribution of the radiation intensity than must be in the case of a more accurate calculation. Therefore, so far we have no reason to believe that distributions (5)–(7) inaccurately describe the preshock parameters of the wind from the Crab pulsar.

Jet-like Features

In the model that is a simple generalization of the model by Kennel and Coroniti (1984), we failed to obtain something similar to the bright jet-like features observed in the Crab Nebula. However, noteworthy is one circumstance that has a direct bearing on the observed jets. As we already pointed out above, the plasma pressure in the plerion is roughly the same, because the flow is subsonic. The relativistic-plasma pressure is given by the relation $p = \frac{1}{3}n(r,\theta)\epsilon$, where ϵ is the mean particle energy. Since it is proportional to the Lorentz factor of the preshock plasma γ_1, the plasma density in the plerion is

$$n(r,\theta) = n_{\rm eq}\frac{\gamma_0 + \gamma_m}{\gamma_0 + \gamma_m \sin^2\theta}, \qquad (22)$$

where $n_{\rm eq}$ is the equatorial plasma density. Density (22) appears in expression (19) for the electron spectrum. We see from this expression that $n_{\rm axis}/n_{\rm eq} = \gamma_m/\gamma_0$. In standard models, $\gamma_0 \approx 200$ and $\gamma_m \approx 3\times 10^6$, implying that the plasma density in the plerion near the rotation axis is approximately a factor of 15 000 higher than the equatorial plasma density. It is important to note that this fact is a direct result of the energy distribution in the wind (5) and depends weakly on any other factors. Thus, if the luminosity were simply proportional to the plasma density, then we would observe only an extremely bright jet from the pulsar in the plerion with a barely visible torus against its background. However, this is not the case. The increase in density toward the rotation axis causes no brightening, because this increase is accompanied by the simultaneous decrease in particle energy. As a result, the volume emissivity decreases toward the rotation axis.

Thus, the formation of dense but relatively cold jet-like features in the plerion along the rotation axis necessarily follows from the theory of the interaction between the Crab pulsar anisotropic wind and the interstellar medium. There is only one problem: through which processes these features can become bright enough to be observable. A possible solution could be the assumption that some particle acceleration takes place not only at the shock but also in the entire volume of the plerion. This assumption seems reasonable (Begelman 1998) and is supported by the detection of gamma-rays with energy above 50 TeV

from the Crab Nebula (Tanimori *et al.* 1998). If we assume that an additional weak particle acceleration takes place in the entire volume of the nebula, the spectral shape of the accelerated particles is the same everywhere, and the number of accelerated particles is proportional to the plasma density in the plerion, then a second radiation component proportional to the particle density in the nebula emerges. We see from Fig. 2 that in this case, the second radiation component manifests itself in the form of bright jets, with the fraction of the accelerated particles being 2×10^{-8} of their local density.

CONCLUSIONS

Based on the standard theory by Kennel and Coroniti (1984), we have shown that the principal features of the observed X-ray structure in the Crab Nebula can be naturally explained by taking into account anisotropy of the energy flux in the winds from radio pulsars. For our calculations, we used the fact that the energy flux density in the pulsar wind is proportional to $\sin^2\theta$. This dependence follows from the expression for the Poynting flux P_y for axisymmetric winds, $P_y \sim r^2 \sin^2\theta B_p^2$, provided that the poloidal magnetic field B_p pulled by the wind from the source is isotropic. Such a dependence remains valid even for an obliquely rotating source with a uniform magnetic field, although, in general, the flow is not steady and axisymmetric in this case (Bogovalov 1999). For a nonuniform (in θ) poloidal magnetic field, the θ dependence of the energy flux density can change. However, it is easy to understand that the energy flux density is at a minimum on the rotation axis and reaches a maximum at the equator, irrespective of the rotation angle and at any reasonable distribution of the poloidal magnetic field in θ. This is because the Poynting flux density is proportional to the toroidal magnetic field B_φ. However, $B_\varphi = 0$ always on the axis. Therefore, $P_y = 0$ on the rotation axis and P_y can only increase when moving away from the axis.

The breakdown of azimuthal uniformity of the poloidal magnetic field leads to the additional generation of magnetosonic waves (but not magnetodipole radiation) in the wind. However, the energy flux in them is also proportional to the combination $r^2 \sin^2\theta \langle B_p^2 \rangle$ (at least for a small wave amplitude; Bogovalov 2001b). Therefore, irrespective of the rotation angle, P_y always reaches a maximum at the equator, except for the exotic case where B_p decreases toward the equator faster than $\sin^{-1}\theta$. In other words, the concentration of the energy flux density toward the equator is apparently a common property of the pulsar winds.

The formation of a bright X-ray torus is a direct result of this common property of the pulsar winds. The interaction between a wind with such anisotropy and the interstellar medium also inevitably gives rise to cold subsonic (jet-like) flows in the plerion along the rotation axis whose density is almost four orders of magnitude higher than the equatorial density. In the standard theory, these flows are invisible in X-rays, because the particle energy is too low to produce detectable synchrotron radiation. However, if we assume the additional acceleration of a mere 10^{-8} fraction of the particles at each point of the plerion, then the radiation from the jet-like features becomes comparable in intensity to the the torus radiation and the overall morphology of the plerion becomes similar to that observed on the Chandra observatory. It would be natural to assume that similar features detected around the Vela pulsar (Pavlov *et al.* 2001) and in the supernova remnant G $0.9 + 01$ (Gaensler 2001) can be explained in a similar way, because the anisotropy in the pulsar wind of the type discussed here must be formed in all pulsars.

ACKNOWLEDGMENTS

This study was supported in part by the joint INTAS–ESA grant no. 99-120 and as part of the project "Universities of Russia–Basic Science" (registration no. 015.02.01.007).

APPENDIX
A WEAKLY ANISOTROPIC WIND

The actual pulsar wind has a strong latitudinal dependence of the particle energy. The ratio γ_m/γ_0 is of the order of 10^4. However, for a qualitative understanding of the interaction between an anisotropic wind and the ambient medium, it is of interest to consider this interaction for a weak anisotropy. This problem is valuable in that its solution can be obtained analytically.

As was already pointed out above, the approximation of a hydrodynamic interaction is invoked to describe the plasma flow. In addition, the problem is axisymmetric. Let us introduce the stream function ψ. It is related to the physical quantities by

$$nu_r = \frac{1}{r\sin\theta}\frac{\partial\psi}{r\partial\theta}, \qquad (A.1)$$

$$nu_\theta = -\frac{1}{r\sin\theta}\frac{\partial\psi}{\partial r}, \qquad (A.2)$$

where n is the intrinsic particle number density and u_r, u_θ are the corresponding components of the four-velocity. It is convenient to use the equations for

the stream function in spherical coordinates (Beskin 1997)

$$(u_s^2-u_r^2)\psi_{rr}+(u_s^2-u_\theta^2)\frac{\psi_{\theta\theta}}{r^2}-2u_ru_\theta\frac{\psi_{r\theta}}{r} \quad (A.3)$$
$$-u_s^2nu_r\cos\theta+nu_\theta\sin\theta(2u_r^2+u_\theta^2)=(nr\sin\theta)^2$$
$$\times\left[u_s^2\gamma^2\frac{d\ln A}{d\psi}+\frac{\delta-1}{\delta}(u_s^2-u_r^2)\frac{d\ln S}{d\psi}\right],$$

where $u_s^2=\dfrac{\delta-1}{2-\delta}$ and $\delta=4/3$ is the polytropic index of the relativistic plasma,

$$S(\psi)=\frac{p}{n^\delta}. \quad (A.4)$$

Since the motion is adiabatic, S is conserved along a streamline and depends only on ψ. The ratio of the Bernoulli integral and S is

$$A=\frac{\delta}{\delta-1}\frac{\gamma w}{nS(\psi)}. \quad (A.5)$$

It is also conserved along a streamline. Here, w is the thermal function per particle in the intrinsic coordinate system and p is the intrinsic pressure. In the ultrarelativistic case, w and p are related by the equation of state $w=\dfrac{\delta}{\delta-1}p$. For weak anisotropy, we solve Eq. (A.3) using the perturbation theory by assuming that the Lorentz factor of the wind depends on the polar angle as

$$\gamma=\gamma_w(1+\alpha\sin^2\theta), \quad (A.6)$$

where α is a small dimensionless parameter and γ_w is the Lorentz factor of the wind.

In the zero approximation, the flow is spherically symmetric, $u_\theta=0$, and the following identities hold: $\dfrac{dA}{d\psi}=0$ and $\dfrac{dS}{d\psi}=0$. The right-hand side of Eq. (A.3) becomes zero and it takes the form

$$u_s^2\psi_{0\theta\theta}-u_s^2nu_r\cos\theta=0. \quad (A.7)$$

The solution of Eq. (A.7) is

$$\psi_0=n_{\rm sh}u_{\rm sh}r_{\rm sh,0}^2(1-\cos\theta), \quad (A.8)$$

where $r_{\rm sh,0}$ is the radius of the spherical shock wave and $n_{\rm sh}, u_{\rm sh}$ are the density and the radial component of the four-vector immediately behind the shock. According to Landau and Lifshitz (1986), $u_{\rm sh}=\dfrac{c}{\sqrt{8}}$. To solve the equation in the first order of the perturbation theory, we represent the stream function as

$$\psi=n_{\rm sh}u_{\rm sh}r_{\rm sh,0}^2\left(1-\cos\theta+\alpha f(r,\theta)\right), \quad (A.9)$$

where $f(r,\theta)$ is the correction to the first approximation. The equation for it is

$$(u_s^2-u_0^2)f_{rr}+\frac{1-\eta^2}{r^2}u_s^2f_{\eta\eta} \quad (A.10)$$
$$-2\frac{u_0^2}{r}f_r=-\frac{(n_0r)^2}{\left(n_{\rm sh}r_{\rm sh}^2u_{\rm sh}\right)^2}(1-\eta^2)$$
$$\times\left[u_s^2\gamma^2\frac{d\ln A(\psi)}{d\eta}+\frac{\delta-1}{\delta}(u_s^2-u_0^2)\frac{d\ln S(\psi)}{d\eta}\right],$$

where $\eta=cos\theta$ and u_0, n_0, γ are the solution behind the shock in the zero approximation.

To determine A and S, we use the shock-adiabat relations for an oblique relativistic shock wave. These are derived from Landau and Lifshitz (1986) using the Lorentz transformations

$$v_{1,\perp}=\sqrt{1-v_\parallel^2}\left[\frac{(p_2-p_1)(e_2+p_1)}{(e_2-e_1)(e_1+p_2)}\right]^{1/2}, \quad (A.11)$$

$$v_{2,\perp}=\sqrt{1-v_\parallel^2}\left[\frac{(p_2-p_1)(e_1+p_2)}{(e_2-e_1)(e_2+p_1)}\right]^{1/2}, \quad (A.12)$$

where p is the pressure and e is the internal energy. The quantities with the subscripts 1 and 2 describe the preshock and postshock states of the wind, respectively. $v_\parallel$ and $v_\perp$ are the tangential and normal velocity components, respectively.

Since the thermodynamic state of the matter in the preshock region corresponds to a zero temperature,

$$p_1=0, e_1=mc^2n_1. \quad (A.13)$$

According to (21, A.6), the density can be represented as

$$n_1=(1-\alpha\sin^2\theta)\frac{n_w}{r^2}, \quad (A.14)$$
$$n_w=\frac{\dot N}{4\pi v_p\gamma_w}.$$

The function $r_{\rm sh}(\theta)$ can be represented as a series of Legendre polynomials P_m,

$$r_{\rm sh}(\theta)=r_{\rm sh,0}\left(1+\alpha\sum_m R_mP_m(\cos\theta)\right). \quad (A.15)$$

In front of the shock, we then have

$$n_1=\frac{n_w}{r_{\rm sh,0}^2} \quad (A.16)$$
$$\times\left(1-\alpha\sin^2\theta-2\alpha\sum_m R_mP_m(\cos\theta)\right),$$

$$e_1=\frac{mc^2n_w}{r_{\rm sh,0}^2} \quad (A.17)$$
$$\times\left(1-\alpha\sin^2\theta-2\alpha\sum_m R_mP_m(\cos\theta)\right).$$

In the ultrarelativistic case, the following relations hold: $e_2 \gg e_1$ and $p_2 \gg e_1$. They allow (A.11), (A.12) to be simplified. For $\delta = 4/3$, we have

$$p_2 = \frac{2}{3}\frac{\gamma_1^2}{\gamma_\parallel^2}e_1, \quad \gamma_2^2 = \frac{9}{8}\gamma_\parallel^2, \tag{A.18}$$

where $\gamma_\parallel = \dfrac{1}{\sqrt{1-v_\parallel^2}}$.

The postshock plasma density can be calculated by using the Bernoulli integral

$$n_2 = n_1\frac{\gamma_2}{\gamma_1}\frac{\delta}{\delta-1}\frac{p_2}{e_1}. \tag{A.19}$$

For weak anisotropy, $v_\parallel \ll 1$. We see from the geometry shown in Fig. 3 that

$$\frac{1}{\gamma_\parallel} \approx 1 - \frac{1}{2}v_1^2\sin^2\beta \approx 1 - \frac{v_1^2}{2}\left(\frac{r'_{\rm sh}(\theta)}{r_{\rm sh}(\theta)}\right)^2. \tag{A.20}$$

Since $r'_{\rm sh} \sim \alpha$, the first corrections to $\gamma_{||}$ begin with the terms proportional to α^2. In the first order of smallness in α, we may assume that $\gamma_{||} = 1$. The change in the postshock thermodynamic quantities when the flow isotropy breaks down results only from a change in the spatial location of the shock front. To a first approximation, the change in the inclination of the shock surface is negligible.

In that case,

$$p_2 = \frac{2}{3}\frac{n_w}{r_{\rm sh,0}^2}\gamma_w^2 mc^2 \tag{A.21}$$
$$\times\left(1 + \alpha\sin^2\theta - 2\alpha\sum_m R_m P_m(\cos\theta)\right),$$

$$\gamma_2^2 = \frac{9}{8}, \tag{A.22}$$

$$n_2 = 3\gamma_0 n_w\left(1 - 2\alpha\sum_m R_m P_m(\cos\theta)\right). \tag{A.23}$$

Hence, we have for A and S

$$S = S_0\left(1 + \alpha\sin^2\theta\right. \tag{A.24}$$
$$\left. + 2/3\alpha\sum_m R_m P_m(\cos\theta)\right),$$

$$A = A_0\left(1 - 2/3\alpha\sum_m R_m P_m(\cos\theta)\right), \tag{A.25}$$

where A_0 and S_0 are the constants that are of no interest.

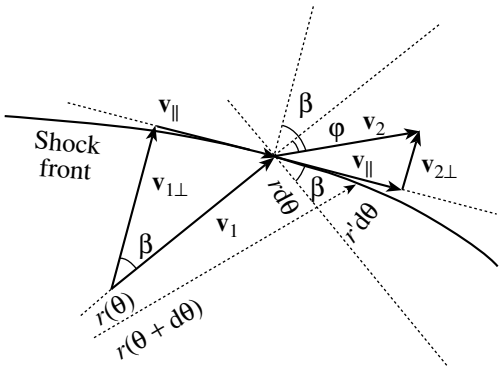

Fig. 3. The flow geometry near the shock front.

Substituting the expressions for A and S in relation (A.10) yields

$$(u_s^2 - u_0^2)f_{rr} + \frac{1-\eta^2}{r^2}f_{\eta\eta} - 2\frac{u_0^2}{r}f_r \tag{A.26}$$
$$= \frac{(n_0 r)^2}{\left(n_{\rm sh}r_{\rm sh}^2 u_{\rm sh}\right)^2}(1-\eta^2)\left[2\eta\frac{u_s^2 - u_0^2}{4}\right.$$
$$\left. - 2/3\left(u_s^2\gamma^2 - \frac{u_s^2 - u_0^2}{4}\right)\sum_m R_m P'_m(\eta)\right].$$

We seek a solution to Eq. (A.26) in the form

$$f(r,\eta) = \sum_n Q_n(\eta)f^{(m)}(r), \tag{A.27}$$

where $Q_m(\eta)$ are the eigenfunctions of the operator

$$(1-\eta^2)Q''_m(\eta) = -m(m+1)Q_m(\eta). \tag{A.28}$$

These are

$$Q_m(\eta) = (1-\eta^2)P'_m(\eta). \tag{A.29}$$

Substituting (A.27) in (A.26) yields

$$(u_s^2 - u_0^2)f_{xx}^{(m)} - \frac{m(m+1)}{x^2}u_s^2 f^{(m)} \tag{A.30}$$
$$- 2\frac{u_0^2}{x}f_x^{(m)} = \frac{1}{u_0^2 x^2}$$
$$\times\left[\frac{2}{3}\delta_{2,m}\frac{u_s^2 + u_0^2}{4} + 2/3\left(u_s^2\gamma^2 - \frac{u_s^2 - u_0^2}{4}\right)R_m\right],$$

where $x = r/r_{\rm sh,0}$.

The function u_0 was numerically determined from the equations for a polytropic, spherically symmetric postshock flow. This function depends only on one variable x. Since the first boundary condition at the shock front is the continuity of ψ,

$$f^{(m)}(1) = 0. \tag{A.31}$$

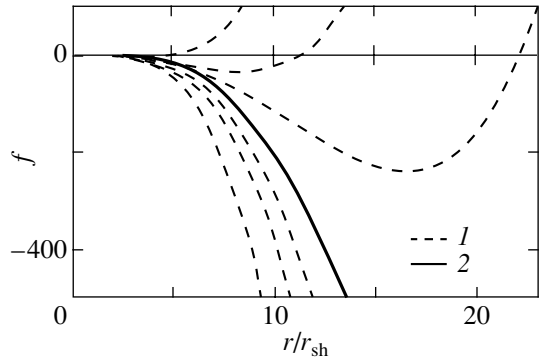

Fig. 4. (*1*) A family of solutions to Eq. (A.30). (*2*) The solid line represents the solution that corresponds to the absence of additional perturbations in the postshock flow.

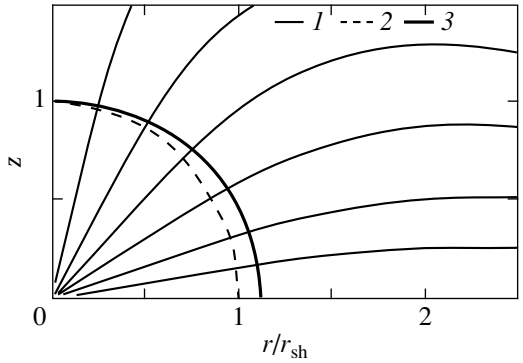

Fig. 5. The distribution of streamlines for a flow with $\alpha = 0.25$. The shock location for isotropic (*dashed line*) and anisotropic (*solid line*) flows. The bending of the streamlines at the shock and the further bending of the flow toward the equator result in the flow compression near the equatorial plane.

The second boundary condition follows from the shock-adiabat relations for an oblique shock wave. Behind the shock,

$$n_2 u_{2\theta} = -\alpha \frac{r_{\rm sh}^2 n_{\rm sh,0} u_{\rm sh}}{r \sin\theta} \frac{\partial f}{\partial r}. \qquad (A.32)$$

We see from Fig. 3 that at $\varphi \ll 1$ and $\beta \ll 1$,

$$\frac{u_{2\theta}}{u_{2r}} = \varphi = -\frac{\alpha}{\sin\theta x} \frac{\partial f}{\partial x}, \quad \varphi + \beta = \frac{v_\parallel}{v_{2\perp}}. \qquad (A.33)$$

In the first order of smallness in α, we have

$$v_{2\perp} = \frac{1}{3}, \quad v_\parallel = \beta = \frac{r'_{\rm sh}(\theta)}{r_{\rm sh}(\theta)}. \qquad (A.34)$$

It follows from (A.33), (A.34) at $x = 1$ that

$$\frac{\partial f}{\partial x} = 2(1-\eta^2) \sum_m R_m \frac{dP_m(\eta)}{d\eta}, \qquad (A.35)$$

and the second boundary condition for $f^{(m)}$ takes the form

$$\frac{\partial f^{(m)}}{\partial x} \mid_{x=1} = 2R_m. \qquad (A.36)$$

The general solution of Eq. (A.30) with the boundary conditions (A.31, A.36) is

$$f^{(m)} = \delta_{m,2} f_1^{(m)} + R_m f_2^{(m)}, \qquad (A.37)$$

where $f_1^{(m)}$ is the solution of the inhomogeneous equation (A.30) with the right-hand side $\frac{1}{u_0^2 x^2}\frac{2}{3} \times \left(u_s^2\gamma^2 - \frac{u_s^2 - u_0^2}{4}\right)$ and the boundary conditions $f_i^{(m)}(1) = 0, \left.\frac{\partial f_i^{(m)}}{\partial x}\right|_{x=1} = 0$. $f_2^{(m)}$ is the solution of the same equation with the right-hand side $\frac{1}{u_0^2 x^2}\frac{2}{3} \times \left(u_s^2\gamma^2 - \frac{u_s^2 - u_0^2}{4}\right)$ and the boundary conditions $f_2^{(m)}(1) = 0, \frac{\partial f_2^{(m)}}{\partial x} = 2$. Since the functions $f_1^{(m)}$ and $f_2^{(m)}$ increase with distance x faster than x^4, $R_m \to 0$ when $x_\infty \to \infty$ under any boundary condition. Therefore, for all $m \neq 0$ and for $m \neq 2$, we may assume that $R_m = 0$. This condition physically means that all obstacles that can be in the flow lie far enough from the shock for their influence on the flow near the shock to be ignored.

Figure 4 shows a family of solutions (A.37) for various R_2. All these solutions satisfy the boundary conditions at the shock. To single out the only solution, we must formulate the boundary conditions far from the shock. It is easy to verify that if there are obstacles in the postshock flow, then the postshock perturbation grows faster than x^4. In this case, the condition that there are no additional obstacles behind the shock in the presence of anisotropy is the requirement that the perturbation should grow with x more slowly than x^4, for example, as x^3. This will take place if the right-hand side of Eq. (A.30) tends to zero as x increases. In turn, it is easy to find that the right-hand side of this equation tends to zero for $R_2 = -\frac{1}{3}$. The solution for this value of R_2 is indicated in Fig. 4 by the solid line. It is the separatrix that separates the solutions tending to $+\infty$ from the solutions tending to $-\infty$ for $x \to \infty$.

Although the expansion of f includes the terms with $m > 1$, we must also determine R_0, because this term appears in the expansion of $r_{\rm sh}$ in terms of Legendre polynomials. This coefficient can be easily determined from the condition for the shock location being constant on the rotation axis. The shock front

then takes the form

$$r_{\rm sh} = r_{\rm sh,0}\left(1+\alpha\left(\frac{1}{3}P_0-\frac{1}{3}P_2\right)\right) \qquad (A.38)$$
$$= r_{\rm sh,0}\left(1+\frac{\alpha}{2}\sin^2\theta\right).$$

In this solution, the postshock pressure p_2 is constant along the front and the density varies as

$$n_2 = 3\gamma_w n_w(1-\alpha\sin^2\theta). \qquad (A.39)$$

Accordingly, the mean energy of the chaotic particle motion behind the shock front $\epsilon_2 = 3p_2/n_2$ is

$$\epsilon_2 = \frac{2}{3}\gamma_w mc^2(1+\alpha\sin^2\theta). \qquad (A.40)$$

Thus, as the energy flux density increases along the equator, the shock front is extended along the equatorial plane; the pressure along the front is constant, to a first approximation. The postshock particle density at the equator is lower and their mean thermal energy is higher than those for the particles along the rotation axis. Figure 5 shows streamlines in the flow for $\alpha = 0.25$. We see that, in addition to this, the increase in the energy flux density along the equator also causes the bending of the streamlines toward the equator. Initially, this takes place at the shock, where, according to the conditions for an oblique shock wave, the streamlines are pressed to the shock. Subsequently, the streamlines continue to be pressed to the equator. Of course, we cannot talk about the behavior of the solutions far from the shock front, where our solution can yield a qualitatively incorrect result. However, we see that there is one tendency at small distances from the shock front: the bending of the streamlines toward the equator behind the shock.

REFERENCES

1. F. A. Aharonian, A. G. Akhperjanian, J. A. Barrio, *et al.*, Astrophys. J. **539**, 317 (2000).
2. J. Arons, Astrophys. J. **266**, 215 (1983).
3. A. M. Atoyan and F. A. Aharonian, Mon. Not. R. Astron. Soc. **278**, 525 (1996).
4. M. C. Begelman and Z.-Y. Li, Astrophys. J. **397**, 187 (1992).
5. M. C. Begelman, Astrophys. J. **493**, 291 (1998).
6. V. S. Beskin, Usp. Fiz. Nauk **167**, 690 (1997) [Phys. Usp. **40**, 659 (1997)].
7. V. S. Beskin, I. V. Kuznetsova, and R. R. Rafikov, Mon. Not. R. Astron. Soc. **299**, 341 (1998).
8. S. V. Bogovalov, Astron. Astrophys. **349**, 1017 (1999).
9. S. V. Bogovalov and K. Tsinganos, Mon. Not. R. Astron. Soc. **305**, 211 (1999).
10. S. V. Bogovalov and F. A. Aharonian, Mon. Not. R. Astron. Soc. **313**, 504 (2000).
11. S. V. Bogovalov, Astron. Astrophys. **371**, 1155 (2001a).
12. S. V. Bogovalov, Astron. Astrophys. **367**, 159 (2001b).
13. K. S. Cheng, M. Ruderman, and L. Zhang, Astrophys. J. **537**, 964 (2000).
14. A. M. Cherepashchuk, Itogi Nauki Tekh., Ser. Astron. **38**, 60 (1988).
15. F. V. Coroniti, Astrophys. J. **349**, 538 (1990).
16. J. K. Daugherty and A. K. Harding, Astrophys. J. **458**, 278 (1996).
17. A. Ferrari, S. Massaglia, G. Bodo, and P. Rossi, in *Solar and Astrophysical Magnetohydrodynamic Flows,* Ed. by K. Tsinganos (Kluwer, Dordrecht, 1996), p. 607.
18. B. M. Gaensler, M. J. Pivovaroff, and G. P. Garmire, Astrophys. J. Lett. **556**, L107 (2001).
19. Y. Gallant, M. Hoshino, A. B. Langdon, *et al.*, Astrophys. J. **391**, 73 (1992).
20. J. J. Hester, in *Proceedings of the International Conference "Neutron Stars and Pulsars: Thirty Years after the Discovery," Tokyo, 1997,* Ed. by N. Shibazaki *et al.*, p. 431.
21. O. C. de Jager and A. K. Harding, Astrophys. J. **396**, 161 (1992).
22. C. F. Kennel and F. V. Coroniti, Astrophys. J. **283**, 710 (1984).
23. L. D. Landau and E. M. Lifshitz, *Course of Theoretical Physics,* Vol. 2: *The Classical Theory of Fields* (Nauka, Moscow, 1973; Pergamon, Oxford, 1975).
24. L. D. Landau and E. M. Lifshitz, *Course of Theoretical Physics,* Vol. 8: *Electrodynamics of Continuous Media* (Nauka, Moscow, 1982; Pergamon, New York, 1984).
25. L. D. Landau and E. M. Lifshitz, *Course of Theoretical Physics,* Vol. 6: *Fluid Mechanics* (Nauka, Moscow, 1986; Pergamon, New York, 1987).
26. M. Livio, Phys. Rep. **311**, 225 (1999).
27. Y. Lyubarsky and J. G. Kirk, Astrophys. J. **547**, 437 (2001).
28. Y. E. Lyubarsky, Mon. Not. R. Astron. Soc. **329**, L34 (2002).
29. L. Mestel, Mon. Not. R. Astron. Soc. **138**, 359 (1968).
30. I. F. Mirabel and L. F. Rodríguez, Nature **392**, 673 (1998).
31. I. Okamoto, Mon. Not. R. Astron. Soc. **185**, 69 (1978).
32. G. G. Pavlov, O. Y. Kargaltsev, D. Sanwall, and G. P. Garmire, Astrophys. J. Lett. **554**, L189 (2001).
33. M. J. Rees and F. E. Gunn, Mon. Not. R. Astron. Soc. **167**, 1 (1974).
34. R. W. Romani, Astrophys. J. **470**, 469 (1996).
35. I. S. Shklovskii, *Supernovae* (Wiley, New York, 1968).
36. T. Tanimori, K. Sakurazawa, S. A. Dazeley, *et al.*, Astrophys. J. Lett. **492**, L33 (1998).
37. C. M. Urri and P. Padovani, Publ. Astron. Soc. Pac. **107**, 803 (1995).
38. M. C. Weisskopf, J. J. Hester, F. A. Tenant, *et al.*, Astrophys. J. Lett. **536**, L81 (2000).

Translated by V. Astakhov

Astronomy Letters, Vol. 28, No. 6, 2002, pp. 386–392. Translated from Pis'ma v Astronomicheskiĭ Zhurnal, Vol. 28, No. 6, 2002, pp. 440–447.

Ionization Freeze-out and Hydrogen Excitation in the SN IIP Atmosphere

V. P. Utrobin[1] and N. N. Chugai[2]*

[1] *Institute of Theoretical and Experimental Physics, ul. Bol'shaya Cheremushkinskaya 25, Moscow, 117259 Russia*

[2] *Institute of Astronomy, Russian Academy of Sciences, ul. Pyatnitskaya 48, Moscow, 109017 Russia*

Received January 24, 2002

Abstract—We study the nonstationary recombination of hydrogen in the atmosphere of SN 1987A by taking into account ion-molecular processes. The hydrogen excitation due to nonstationary recombination is shown to be enough to explain the observed hydrogen lines in a time interval until day 30 in the absence of additional excitation mechanisms. Thus, the problem of a deficit in the hydrogen excitation that has recently been found in modeling the hydrogen spectrum of SN 1987A at an early photospheric stage by assuming statistical ionization equilibrium is resolved. The mass of the radioactive ^{56}Ni with a spherically symmetric distribution in the outer layers is shown to be close to $10^{-6}\ M_\odot$. Our model predicts the appearance of a blue peak in the Hα profile between days 20 and 30. This peak bears a close similarity to the observed peak known as the Bochum event. The presence of this peak in the model is attributable to nonstationary recombination and to a substantial contribution of hydrogen neutralization involving H^- and H_2. © *2002 MAIK "Nauka/Interperiodica".*

Key words: *supernovae—SN 1987A, stellar atmospheres, molecular processes*

INTRODUCTION

In all of the known cases, the hydrogen synthetic spectra of type-II supernovae with a plateau (SN IIP) at the photospheric stage are computed by assuming statistical ionization equilibrium. Meanwhile, nonstationary ionization or freeze-out can play an important role in the excitation of hydrogen in the atmospheres of these supernovae. Freeze-out implies that the recombination rate in an initially ionized, expanding gas does not keep up with the expansion rate and the residual ionization proves to be finite on long time scales (Zel'dovich and Raizer 1963). The best-known example of this kind of phenomenon is recombination in the expanding Universe with residual ionization $x \sim 10^{-4}$ (Zel'dovich *et al.* 1968).

Previously, a simple kinetic model has been used to show that the presence of the Hα absorption line at high velocities in SN 1987A can be entirely attributed to the second-level population through nonstationary recombination (Chugai 1991a) and that only for $t > 30$ days does the need in additional excitation by radioactivity arises. This implies that ignoring the ionization freeze-out in the model synthetic spectra of SN IIP must lead to an artificial deficit in the hydrogen excitation. Amazingly, when modeling the spectrum of SN 1987A at $t = 4$ days, Mitchell *et al.* (2001) came up against the problem of too low hydrogen excitation in their model. To resolve the contradiction required invoking $10^{-4}\ M_\odot$ of radioactive ^{56}Ni mixed in the outer atmospheric layers. Clearly, these conclusions need to be seriously corrected, because the above authors assumed hydrogen statistical ionization equilibrium. Moreover, the postulated mass of the external ^{56}Ni is two orders of magnitude larger than the estimated mass of $10^{-6}\ M_\odot$ required to account for the additional hydrogen excitation in SN 1987A on day ~40 (Chugai 1991b). The aforesaid serves as a serious reason for a more detailed study of the nonstationary ionization in SN 1987A.

An additional motivation for investigating the nonstationary ionization in SN IIP is the problem of the so-called Bochum event. The latter consists in the emergence of two peaks in the Hα profile for SN 1987A after day 20: blue (B) and red (R) peaks (Hanuschik and Dachs 1988; see also Fig. 2). The Bochum event can be qualitatively explained as resulting from a nonmonotonic distribution of the hydrogen second-level population in the atmosphere with an excitation minimum at ~4000–5000 km s^{-1} (B peak) and local enhanced excitation from asymmetric ^{56}Ni ejection in the far hemisphere (R peak) (Chugai 1991b). Since the amplitude of the Bochum

*E-mail: nchugai@inasan.ru

1063-7737/02/2806-0386$22.00

event is at a maximum in the period of the deepest atmospheric hydrogen recombination (as signaled by the temporary disappearance of the Hβ absorption on day $\sim$40), the nonstationary ionization can be of great importance in understanding the physical essence of this event.

Here, we make the first attempt to analyze in detail the nonstationary ionization in the hydrogen excitation at the photospheric stage of SN IIP. Strictly speaking, such an analysis must be based on a self-consistent model of the continuum and line spectra with allowance made for nonstationarity of both the radiation field and the matter. However, we restrict our analysis to the simpler problem of computing the nonstationary recombination kinetics for a given evolution of the continuum. More specifically, we consider SN 1987A whose photospheric spectrum and photosphere radius are known from observations. This case is also convenient, because, in our view, the ionization freeze-out in SN 1987A is presumed to be more significant than that in other SN IIP. This is supported by the fact that because of the relatively small radius of the supernova progenitor, the adiabatic cooling of radiation in SN 1987A after its explosion was more significant than that in normal SN IIP, and, as a result, the cooling (recombination) wave stage began earlier than usual (Grasberg *et al.* 1987). We consider not only the kinetics of radiative and collisional hydrogen recombination but also the hydrogen neutralization involving H^-, hydrogen molecules, and their ions.

THE MODEL

As SN IIP expands, its photosphere displaces inward relative to the matter. At some time t_0, the corresponding element of gas with the Lagrangian coordinate m crosses the photosphere and falls into the atmosphere, where its ionization and excitation subsequently evolve somehow. The problem is to compute the degree of hydrogen ionization and the hydrogen level populations, as well as the mass fractions of hydrogen molecules and their ions in the atmosphere, as functions of the Lagrangian-particle velocity v and time t. To this end, we solved the system of kinetic equations in a comoving frame for the hydrogen populations with 15 levels and for the mass fractions of atomic and molecular hydrogen and their ions (H^+, H^-, H_2, H_2^+, H_3^+) by taking into account major collisional and radiative processes in the photospheric radiation field. Rate constants for the collisional processes and cross sections of the photoprocesses for the 38 reactions considered were taken from Galli and Palla (1998), Abel *et al.* (1997), Rawlings *et al.* (1993), and Hollenbach and McKee (1979). As the initial conditions for the ionization and excitation of gas at the photosphere, we used the steady-state solution at electron temperature $T_e = q_p T_{eff}$, where the effective temperature T_{eff} was taken from Catchpole *et al.* (1987) and $q_p < 1$ is a free parameter. The distribution of density $\rho(v,t)$ and velocity $v(m,t)$ in the SN 1987A envelope was computed by using a hydrodynamic model (Utrobin 1993). Note that the hydrodynamic model is required not only to fix the density distribution but also because the free-expansion approximation ($v = r/t$) breaks down at an early stage ($t < 1$ day).

Model parameters

Model	t, days	E, 10^{51} erg	q_p	q_a	$M_{Ni,ex}/M_\odot$
D20	20	1.9	0.9	0.7	0
D30	30	1.9	0.9	0.7	0
S30	30	1.9	0.9	0.7	0
M30	30	1.9	0.9	0.7	0
T30	30	1.9	0.9	0.8	0
Q30	30	1.9	0.9	0.65	0
P30	30	1.9	1.0	0.7	0
L30	30	1.5	0.9	0.7	0
E30	30	1.9	0.9	0.7	10^{-6}
A30a	40	1.9	0.8		0
A30b	40	1.9	0.8		10^{-6}

For $t > 1.78$ days, we took the photosphere radius and the continuum from Catchpole *et al.* (1987), while in the ultraviolet we used IUE data (Pun *et al.* 1995). At $\lambda < 1000$ Å, for which no data are available, the flux was assumed to be a factor of 25 lower than the Planck flux at temperature T_{eff}. This factor was taken from the fit to the observed spectrum near $\lambda \approx 1000$ Å. For $t < 1.8$ days, the photosphere radius (R_p) and the photospheric temperature were taken from the hydrodynamic model. The theoretical parameters of the photosphere were smoothly joined with its phenomenological parameters near velocity 14 000 km s^{-1} and $t = 1.8$ days. We ignore the atmospheric effect on the photospheric spectrum, which can in principle take place in the ultraviolet where metal lines and Rayleigh scattering are of great importance.

We considered two electron-temperature distributions in the atmosphere: the radiative one $T_e = q_a W^{0.25} T_{eff}$, where W is the dilution factor, and the adiabatic one $T_e = T_{eff}(t_0/t)^2$. The former implies a relatively close contact between radiation and matter

in the atmosphere, whereas the latter assumes that there is no energy transfer between radiation and matter. Below, the electron temperature is assumed to be equal to the kinetic temperature of the remaining particles.

The kinetic equations include the nonthermal ionization and excitation of hydrogen by fast electrons produced by the absorption of gamma-rays from ^{56}Ni and ^{56}Co decays. The transfer of gamma-ray photons is computed by assuming that the interaction is absorption in nature with the absorption coefficient $k_\gamma = 0.03$ cm^2 g^{-1}. At the stage under consideration, the contribution in the atmosphere of the gamma-ray energy from the bulk of ^{56}Ni distributed in subphotospheric layers (internal nickel-56) is negligible, because these gamma-ray photons are effectively absorbed on the spot. At the same time, a modest amount of external ^{56}Ni with a mass of $\sim 10^{-6}\ M_\odot$ may be present in the outer layers and may contribute appreciably to the ionization and excitation of hydrogen in the atmosphere after day 30 (Chugai 1991a, 1991b).

As the standard model of the density distribution, we take the envelope produced by the explosion of a supernova progenitor (see Utrobin 1993) with radius $R_0 = 47\ R_\odot$ and initial mass 16.3 $M_\odot$ for ejected-envelope mass 15 $M_\odot$. During our preliminary computations, we concluded that the density distribution in the envelope most likely corresponds to an enhanced kinetic energy $E \approx 1.9 \times 10^{51}$ erg, which is taken for the standard model of the envelope. Below, we present the results of our computations of the hydrogen ionization and excitation in the atmosphere of SN 1987A on days 20 and 30 for several models with different sets of major parameters (see the table). All models, except the special case of stationary model S30, were computed in terms of nonstationary kinetics. The electron temperature corresponds to the radiative case, except two models, A30a and A30b, with the adiabatic electron-temperature distribution. We took into account molecules in all models, except M30 in which the molecular processes, including the H^- formation, were completely blocked. Models T30 and Q30 demonstrate the role of electron-temperature variations in the atmosphere, while model P30 demonstrates the electron-temperature effect at the photosphere. Our preliminary computations revealed a noticeable sensitivity of the nonstationary ionization to the density distribution. To demonstrate this effect, we computed a model with a lower energy L30. Models E30 and A30b show the roles of the external ^{56}Ni in the radiative and adiabatic cases, respectively.

RESULTS

The computed hydrogen-level populations for specified parameters of the photosphere allow the Hα profile to be easily constructed. This profile is shown in Fig. 1, in relative intensities, for all the models listed in the table. Let us turn to the central question concerning the role of nonstationary ionization in the hydrogen excitation. Figure 1a demonstrates a dramatic significance of the nonstationarity effect: in the stationary model S30, the Hα line is simply absent, whereas in the nonstationary model D30, we see an intense line similar to that observed in the spectrum of SN 1987A (see Fig. 2). The absence of this line in the stationary case stems from the simple fact that the collisional and radiative excitation of hydrogen for a relatively cool photospheric spectrum and low electron temperature is negligible. On the other hand, as we see, the residual ionization in the nonstationary model provides an acceptable second-level population in the absence of other excitation sources, in agreement with a previous result (Chugai 1991a). The hydrogen excitation through residual ionization decreases with time, as can be seen from a comparison of the profiles on days 20 and 30 (Fig. 1b).

A remarkable feature of the nonstationary model D30 is the presence of a peak in the Hα profile, which can be identified with the B peak of the Bochum event (feature B in Fig. 2). However, it should be immediately emphasized that the similarity is only qualitative, because we did not set the objective to closely fit a model to the observations. Just as in the observations, the B peak is unseen on day 20 (see Figs. 1b and 2). In our model, the B peak reflects the presence of a minimum in the distribution of the Sobolev optical depth in Hα (or a minimum in the hydrogen second-level population) near a velocity of 4000 km s^{-1} (Fig. 3a). The minimum of hydrogen excitation is attributable to a deep local minimum of hydrogen ionization (Fig. 3b), because the excitation is essentially determined by the arrival at this level through recombination ($n_2 \propto x^2 n^2$).

Molecular processes play a crucial role in the formation of a deep ionization minimum. The latter is demonstrated by model M30 (Fig. 1c), in which all molecular processes, including H^- formation, are blocked. This model shows no B peak, although it still exhibits a minimum of hydrogen ionization near 4000 km s^{-1} (Fig. 3b). However, this minimum is an order of magnitude shallower than that in model D30. Analysis of the included ion-molecular processes indicates that the chain of two reactions involving H^-, including the H^- formation in the reaction $H + e \rightarrow H^- + h\nu$ followed by the neutralization $H^+ + H^- \rightarrow 2H$, is a dominant additional

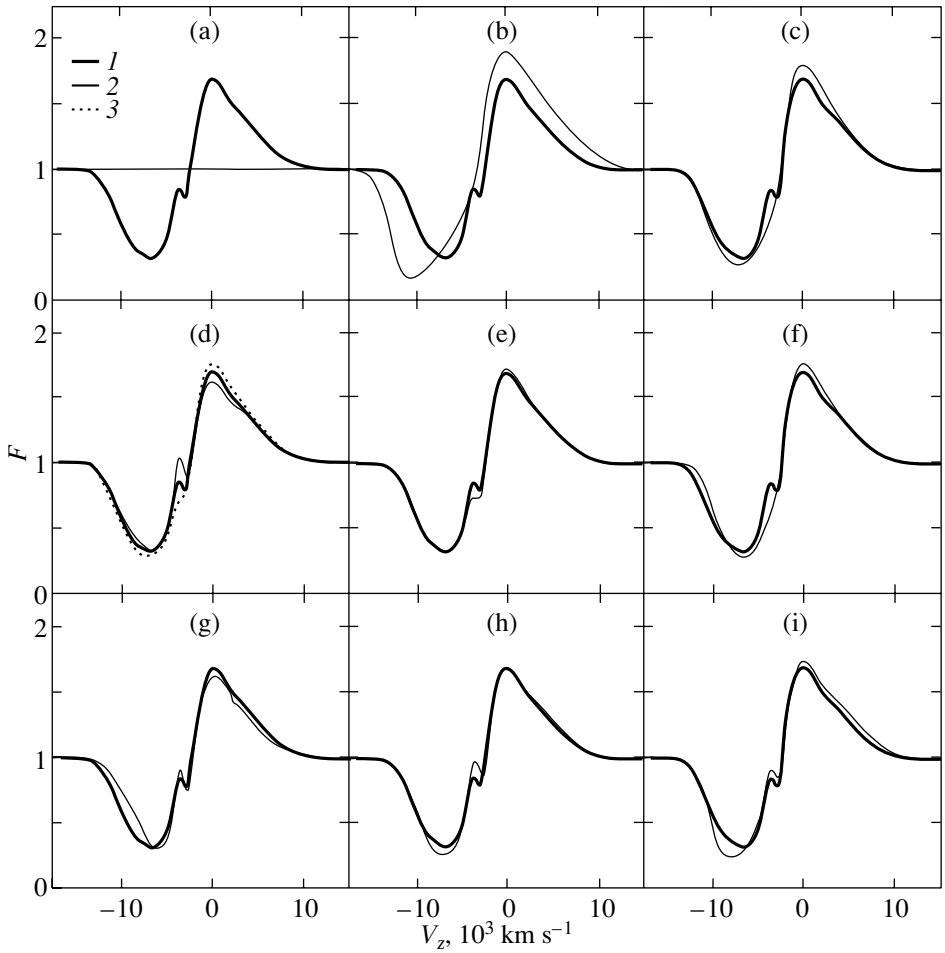

Fig. 1. The theoretical Hα profile in the standard model D30 (*1*) in comparison with the profiles computed under various conditions (see the table). The figure sequentially shows the following: (a) the nonstationarity effect demonstrated by the stationary model S30 (the horizontal line with the Hα line of almost zero intensity) and by the nonstationary model D30 on day 30; (b) the evolution in the nonstationary model between day 20 (D20) and day 30 (D30); (c) the effect of switched-off molecular processes (M30); (d) the effect of a decrease (Q30—*2*) and increase in electron temperature in the atmosphere on the amplitude of the B peak (T30—*3*); (e) the effect of an elevated initial electron temperature at the photosphere on the amplitude of the B peak (P30); (f) the effect of the explosion energy on the profile (L30); (g) the model with an adiabatic decease in electron temperature (A30a); (h) the effect of the external ^{56}Ni on the depth and position of the main absorption minimum in the adiabatic case (A30b); (i) the effect of the external ^{56}Ni in the radiative case (E30).

hydrogen neutralization mechanism. The second most important ion-molecular process of hydrogen neutralization, which is a factor of 3 weaker than the first one, is the chain of three reactions, including the charge exchange reaction $H^+ + H_2 \rightarrow H_2^+ + H$ and the H_3^+ formation ($H_2^+ + H_2 \rightarrow H_3^+ + H$) followed by the dissociative recombination $H_3^+ + e \rightarrow H_2 + H$. In this chain of hydrogen neutralization reactions, H_2 acts a catalyst. Note the significant H_2 abundance, which reaches 2×10^{-3} at maximum ($\approx$4000 km s^{-1}) and exceeds the H^- abundance by nine orders of magnitude (Fig. 3b).

The origin of the ionization minimum can be qualitatively understood in terms of the following simplified analytic treatment. The approximate equation for the electron density with the expansion, photorecombination, neutralization involving H^-, and photoionization of hydrogen from the second level is

$$\frac{dn_e}{dt} = -\frac{3n_e}{t} - \alpha n_e^2 - k_1 n_e n(H^-) + P_2 n_2, \quad (1)$$

where α is the recombination coefficient to excited levels; the meaning of the remaining quantities is clear from the list of included processes. The mass fraction of H^- can be determined from the condition of balance $n(H^-) \approx k_2 n_e n/P$ between the formation through photoattachment ($H + e$) and the destruction through photodetachment at rate P. The second-level population can be derived from the balance between the recombination population, pho-

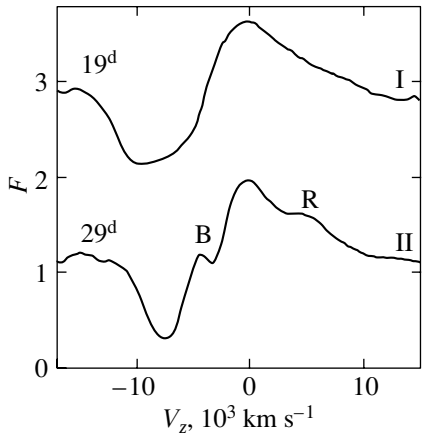

Fig. 2. The Hα profile for SN 1987A on days 19 (I) and 29 (II) (Hanuschik and Dachs 1988), which illustrates the Bochum event.

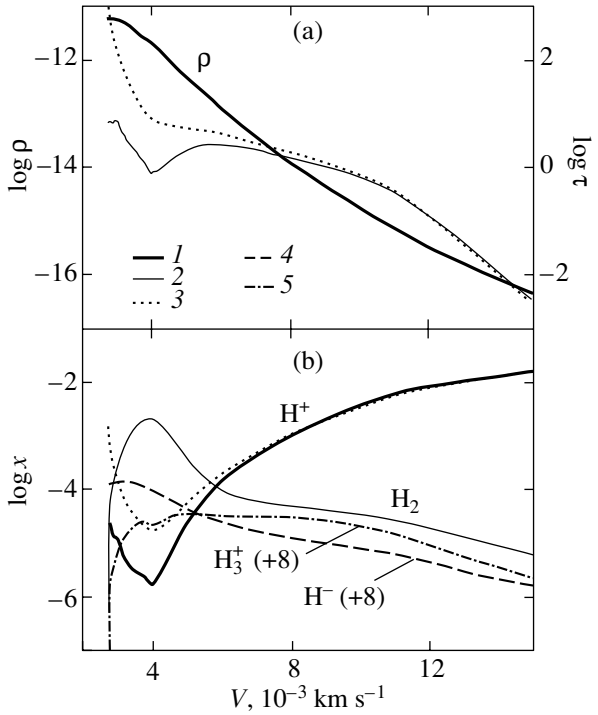

Fig. 3. The behavior of the density and optical depth in Hα in the atmosphere on day 30 (a) in model D30 (*1*, *2*) and in model M30 without molecules (*3*). (b) The mass fraction of H^+ in models D30 (*1*) and M30 (*3*); the mass fraction of H_2, H^- (*4*), and H_3^+ (*5*) in model D30. The latter two curves are displaced upward by eight orders of magnitude.

toionization from the second level, and transitions to the ground level, among which the two-photon $2s-1s$ decay dominates: $n_2(P_2+A_{2q})=\alpha n_e^2$. Substituting $n(H^-)$ and n_2 in Eq. (1), taking into account the fact that $P_2 \gg A_{2q}$, and passing to the degree of ionization x, we obtain the equation

$$\frac{dx}{dt}=-\alpha n x^2\frac{A_{2q}}{P_2}-\frac{k_1k_2n^2x^2}{P}. \qquad (2)$$

The first and second terms on the right-hand side can be represented as $x^2y_r(v)z_r(t)$ and $x^2y_n(v)z_n(t)$, respectively; $y(v)$ are rapidly decreasing functions of velocity (because n decreases), with y_n decreasing much more steeply than y_r, and $z(t)$ are decreasing functions of time. Integrating Eq. (2) at fixed v between the limits t_0 and t (where t_0 is the time at which a given Lagrangian particle emerges from the photosphere) and assuming that $x(t_0)=x_0$, we obtain

$$\frac{1}{x}=\frac{1}{x_0}+y_r(v)Z_r(t_0,t)+y_n(v)Z_n(t_0,t). \qquad (3)$$

The functions $Z_r(t_0,t)$ and $Z_n(t_0,t)$ become zero at $t=t_0$ and increase with the t/t_0 ratio. The velocity at the photospheric level, v_p, is uniquely related to the expansion time, with $v=v_p$ at $t=t_0$ and $t_0(v)$ being a decreasing function of v. This implies that both $Z(v)$ become zero at $v=v_p$ and are increasing functions of velocity. Given these properties of $y(v)$ and $Z(v)$ and assuming that $x_0(v)\approx$ const, it is easy to verify after differentiating $1/x$ with respect to v that the function $1/x$ has a local maximum and that the degree of ionization has a minimum at some velocity $v_{min}>v_p$. It is important to emphasize that x has a minimum if we take into account the recombination alone ($Z_n=0$) and both recombination and neutralization. The question of whether a minimum in the behavior of the electron density $n_e(v)$ (and, hence, in the second-level population) is present will be determined by the rate of increase in x with v for $v>v_{min}$. Since the velocity dependence of the neutralization rate is much steeper than that for the radiative recombination, it is clear why the ionization minimum in the former case is significantly sharper than in the latter case (Fig. 3b) and why there is a minimum of the Hα optical depth near 4000 km s^{-1} in model D30 and no such minimum in model M30 (Fig. 3a).

Thus, although the ionization minimum is also present for ordinary radiative recombination, it produces no distinct minimum in the second-level population ($n_2\propto x^2n^2$). Only the neutralization involving H^- and H_2 gives rise to a minimum in the $n_2(v)$ distribution and, hence, a B peak in the Hα profile. In ordinary SN IIP, whose temperature at the corresponding stage is higher than that of SN 1987A, the formation rate of H^- and H_2 must be lower and, hence, no minimum arises in the $n_2(v)$ distribution.

The amplitude of the B peak is indirectly affected by the electron (kinetic) temperature in the atmosphere, as demonstrated by models T30 and Q30

(Fig. 1d): at a higher electron temperature, the ionization minimum is shallower because of the decrease in the rate of recombination and neutralization; as a result, the hydrogen excitation is higher, causing the B peak to wash out. A similar effect causes the photospheric electron temperature to increase (Fig. 1e). In this case, however, the physical cause is slightly different: the ionization evolution starts at the photosphere from a higher ionization and, hence, the ionization and excitation have no time to decrease in the $v \sim 4000$ km s^{-1} region to low values at which the contrast of the B peak would become higher. The position and amplitude of the excitation minimum in the atmosphere also depend on the density and its distribution in the envelope. This is illustrated by model L30 with a lower explosion energy (Fig. 1f) and, hence, with a lower density in the $v > 3000$ km s^{-1} region. If an appropriate model is available for the electron-temperature distribution, then the amplitude and position of the B peak can be used to diagnose the density distribution in the envelope of SN 1987A.

The case of the adiabatic electron-temperature behavior (model A30a) differs markedly from the radiative case (D30) (see Fig. 1g). This would be expected, because, as we already saw, the result depends on the electron temperature. Note that to obtain a reasonable amplitude of the B peak in model A30a, the photospheric temperature parameter was taken to be $q_\mathrm{p} = 0.8$; at $q_\mathrm{p} = 0.9$, the peak is too weak. The presence in the adiabatic model of $10^{-6}\ M_\odot$ of the external ^{56}Ni distributed in the layer at $v = 10\,000$ km s^{-1} (model A30b) causes the main absorption component of model A30a to be appreciably enhanced at high velocities. The effect of the same amount of ^{56}Ni in the radiative model D30 (E30) is shown in Fig. 1i. A comparison with observations (Fig. 2b) indicates that the shape and position of the main absorption minimum in the models with external ^{56}Ni agree with the observed picture. At the same time, this agreement shows that the amount of symmetrically distributed external ^{56}Ni in the envelope of SN 1987A is close to $10^{-6}\ M_\odot$, which confirms a previous estimate (Chugai 1991b). We emphasize that the ^{56}Ni condensation responsible for the R peak is not considered in the model.

DISCUSSION

Our study of the nonstationary kinetics of hydrogen recombination involving molecular processes in the atmosphere of SN 1987A has lead us to an important conclusion that the hydrogen excitation for $t <$ 40 days is mainly related to nonstationary recombination. This conclusion is consistent with a previous result based on a simple kinetic model of radiative recombination (Chugai 1991a). Thus, the significant deficit of hydrogen excitation in the synthetic model spectra for SN 1987A (Mitchell *et al.* 2001) is an artifact produced by the approximation of statistical equilibrium in the calculations of hydrogen ionization and excitation. We may go even further and assume that the He I 5876 Å absorption line in the early spectra of SN 1987A probably results from to the nonstationary ionization of He I. However, a final conclusion about the nature of the He excitation in the early spectra of SN 1987A can be reached only by analyzing in detail the nonstationary ionization with the inclusion of a multilevel model He atom. We only note that either an enhanced He abundance up to $Y = 0.9$ (Eastman and Kirshner 1989) or excitation by X-ray radiation from the shock generated by the interaction with stellar wind was invoked to explain the He I 5876 Å line in SN 1987A. The conclusion about a significant role of the ionization freeze-out in the hydrogen excitation at the photospheric stage, of course, applies not only to SN 1987A but also to the remaining SN IIP.

Our second important result is that the nonstationary model naturally holds the possibility of the B peak of the Bochum event appearing in the Hα profile. The presence of the B peak in the model is related to the minimum of hydrogen excitation at which the optical depth in Hα at 4000 km s^{-1} is much smaller than unity. As we saw, the nature of the excitation minimum is determined by the combined effect of nonstationary recombination in the expanding atmosphere with an outwardly decreasing density and a significant contribution of the ion-molecular neutralization processes involving H^- and H_2 that enhance the ionization minimum. Note that the appearance of a B peak was previously also attributed to the minimum of hydrogen excitation produced by deep hydrogen recombination (Chugai 1991b), but the physical nature of the deep ionization minimum itself has become clear only now. The significant role of ion-molecular processes in the formation of a sharp, deep ionization minimum accounts for the fact that the appearance of a B peak is not typical of ordinary SN IIP: the temperature in them is higher and the mass fractions of H^- and H_2 in them are considerably lower than those needed for a deep minimum of hydrogen excitation to emerge.

The next important result is an unexpectedly high mass fraction of H_2 molecules in the atmosphere, $n(H_2)/n(H) \sim 2 \times 10^{-3}$. The production of molecular hydrogen in SN 1987A was previously considered in terms of a single-zone model for $t > 50$ days (Culhane and McCray 1995). In the above paper, the H_2 fractional abundance near day 50 is $n(H_2)/n(H) \sim$

2×10^{-7}, which is four orders of magnitude lower than that in model D30 at 4000 km s^{-1}. Such a huge difference stems from the fact that the single-zone model describes the situation only in the mixed core of the SN 1987A envelope and does not consider the atmosphere to which our result refers. Unfortunately, even such a large amount of molecular hydrogen is difficult to detect. We estimated the optical depth in the fundamental-tone vibrational–rotational H_2 lines on day 30 in the range 2.1–2.5 μm to be no larger than 10^{-4}. On the other hand, the Lyman lines of the H_2 electron spectrum lie in the far ultraviolet, <1100 Å and are undetectable by absorption, because the flux of the photospheric radiation is extremely low.

A major drawback of our model is that it does not include a calculation of the electron temperature. However, it is unlikely that a more complete model with the energy equation will radically change our results, because we have already investigated both limiting cases of the electron-temperature behavior. Preliminary reasoning shows that the electron-temperature distribution must actually be close to the adiabatic one, which will be slightly modified by the contribution of radioactive heating.

ACKNOWLEDGMENTS

This study was supported by the Russian Foundation for Basic Research (project no. 01-02-16295).

REFERENCES

1. T. Abel, P. Anninos, and Y. Zhang, and M. Norman, New Astron. **2**, 181 (1997).
2. R. M. Catchpole, J. W. Menzies, A. S. Monk, *et al.*, Mon. Not. R. Astron. Soc. **229**, 15P (1987).
3. N. N. Chugai, in *Supernovae: the Tenth Santa Cruz Workshop in Astronomy and Astrophysics, 1989,* Ed. by S. Woosley (Springer-Verlag, New York, 1991a), p. 286.
4. N. N. Chugai, Pis'ma Astron. Zh. **17**, 942 (1991b) [Sov. Astron. Lett. **17**, 400 (1991b)].
5. M. Culhane and R. McCray, Astrophys. J. **455**, 335 (1995).
6. R. G. Eastman and R. P. Kirshner, Astrophys. J. **347**, 771 (1989).
7. D. Galli and F. Palla, Astron. Astrophys. **335**, 403 (1998).
8. É. K. Grasberg, V. S. Imshennik, and D. K. Nadyozhin, Pis'ma Astron. Zh. **13**, 547 (1987) [Sov. Astron. Lett. **13**, 227 (1987)].
9. R. W. Hanuschik and J. Dachs, Astron. Astrophys. **205**, 135 (1988).
10. D. Hollenbach and C. F. McKee, Astrophys. J., Suppl. Ser. **41**, 555 (1979).
11. R. C. Mitchell, E. Baron, and D. Branch, *et al.*, Astrophys. J. **556**, 979 (2001).
12. C. S. J. Pun, R. P. Kirshner, G. Sonneborn, *et al.*, Astrophys. J., Suppl. Ser. **99**, 223 (1995).
13. J. M. C. Rawlings, J. E. Drew, and M. J. Barlow, Mon. Not. R. Astron. Soc. **265**, 968 (1993).
14. V. P. Utrobin, Astron. Astrophys. **270**, 249 (1993).
15. Ya. B. Zel'dovich and Yu. P. Raizer, *Physics of Shock Waves and High-Temperature Hydrodynamic Phenomena* (Fizmatgiz, Moscow, 1963; Academic, New York, 1966).
16. Ya. B. Zel'dovich, V. G. Kurt, and R. A. Sunyaev, Zh. Éksp. Teor. Fiz. **55**, 278 (1968) [Sov. Phys. JETP **28**, 146 (1969)].

Translated by V. Astakhov

Astronomy Letters, Vol. 28, No. 6, 2002, pp. 393–396. Translated from Pis'ma v Astronomicheskiĭ Zhurnal, Vol. 28, No. 6, 2002, pp. 448–451.

Spectroscopic Components in the Multiple Systems ADS 10683 and ADS 11791

M. G. Smekhov*

Sternberg Astronomical Institute, Universitetskiĭ pr. 13, Moscow, 119992 Russia

Received January 16, 2002

Abstract—We presents the results of our study of new spectroscopic components in the visual binaries ADS 10683 (HD 160 239 = BD − 154 635 = HIP 86412; G6/G8V; $V = 9\overset{m}{.}08$; $B-V = 0\overset{m}{.}76$; 2000: $17^h39^m24^s$, $-15°46'$) and ADS 11791 (HD 175039 = BD − 054 798 = HIP 92726; G5; $V = 8\overset{m}{.}78$; $B-V = 0\overset{m}{.}72$; 2000: $18^h53^m42^s$, $-05°33'$). ADS 10683B and ADS 11791A are single-lined spectroscopic binaries; their orbital periods are $6\overset{d}{.}9171 \pm 0\overset{d}{.}0002$ and $50\overset{d}{.}514 \pm 0\overset{d}{.}004$, respectively. We constructed their radial velocity curves and computed their spectroscopic orbital elements. © *2002 MAIK "Nauka/Interperiodica".*

Key words: *stars —double and multiple*

INTRODUCTION

We have surveyed the radial velocities of visual binaries with known orbits since 1993. The prime objective of the survey is to search for and investigate multiple systems. The program included about 300 objects selected mostly from the catalog of orbits of visual binaries (Worley and Heintz 1983). The following criteria were used to select the objects: accessibility to observation at our latitudes, a spectral type later than F5 (due to instrumental limitations), and the absence of known spectroscopic subsystems. At present, our systematic measurements are complete. We continue to observe long-period spectroscopic systems and objects suspected of radial-velocity variations. New spectroscopic components were discovered in the systems ADS 12040 (Smekhov 1994), ADS 363 and ADS 3248 (Smekhov 1995), ADS 4200 and ADS 12656 (Smekhov 1999). In this paper, we present the results of our study of the visual binaries ADS 10683 and ADS 11791. Our radial velocity measurements were carried out with a correlation radial-velocity meter (RVM) (Tokovinin 1987) attached to Zeiss-1000, Zeiss-600 (Simeiz International Observatory) and AZT-2 (Moscow, Sternberg Astronomical Institute) telescopes.

ADS 10683

The orbit of the visual binary system ADS 10683 (HD 160239 = BD − 154635 = HIP 86412; G6/G8V; $V = 9\overset{m}{.}08$; $B-V = 0\overset{m}{.}76$; 2000: $17^h39^m24^s$, $-15°46'$) was computed by Newburg (1966). Its visual orbital elements are given in Table 1.

The system spectrum exhibits lines of the two components. The velocity of component A is constant, -53.78 ± 0.16 km s^{-1}; the velocity of component B varies between -105 and $+2$ km s^{-1}. Thus, component B is a single-lined spectroscopic binary. Our radial-velocity measurements are given in Table 2. At $\Delta V > 20$ km s^{-1}, the spectral lines are clearly resolved and the velocity of each component can be measured separately. In Table 2, such measurements are designated as A and Ba. At $\Delta V <$ 20 km s^{-1}, the lines are blended and only the total velocity of the components can be measured. Such measurements are designated in Table 2 as A + Ba. We did not use the A + Ba measurements to compute the orbit of the spectroscopic subsystem.

The orbit of the spectroscopic subsystem Ba is given in Table 1. For a circular orbit, the initial epoch T corresponds to the component passage through the ascending node, i.e., to the radial-velocity maximum. For 14 observations, the measure of residuals is $\chi^2 = 18.373$ and the unweighted rms deviation is 1.16 km s^{-1}. The radial-velocity curve is shown in Fig. 1.

Equivalent widths of the correlation dip for the two components are given in Table 3. Using the relation between the equivalent width of the RVM correlation dip and color (Tokovinin 1990), the system total color index, and the color–absolute magnitude relation for normal stars, we can construct a model

*E-mail: misha@sai.msu.ru

Table 1. Orbital elements for ADS 10 683

Orbital element	Visual orbit of AB (Newburg 1966)	Spectroscopic orbit of Ba
P	144.4 yr	6.9171 ± 0.0001 days
T	1930.07	50363.05 ± 0.02
e	0.76	0.0
a''	0.513	–
Ω_B, deg	19.8	–
ω_A, deg	–	0.0
ω_B, deg	238.2	–
i, deg	73.70	–
K_A, km s^{-1}	–	54.11 ± 0.49
γ, km s^{-1}	–	-49.12 ± 0.35
$f(m)$, $M_\odot$	–	0.1132 ± 0.0033

for the system, i.e., choose a magnitude difference for which the expected ratio of the line equivalent widths matches its observed value. All our estimates are given in Table 3. Since the lines of component B are weak, the reliability of determining the equivalent width of the correlation dip is moderately high. Our estimate of the magnitude difference slightly exceeds $\Delta m = 0.41$ (Hipparcos 1997), but it confirms that we correctly identified the visual and spectroscopic components; i.e., the visual component B is actually a spectroscopic binary, while component A is a single star.

If the masses of the stars in the system are assumed to be equal to those of normal dwarfs of the corresponding spectral types, then the system dynamical parallax can be determined. According to Allen (1973), the mass of a normal G6-type dwarf is $0.93M_\odot$. The mass function yields a minimum mass for the third component $M_{Bb} > 0.65\ M_\odot$. Thus, taking the masses of components A, Ba, and Bb to be 0.93, 0.93, and 0.65 $M_\odot$, respectively, we obtain a dynamical parallax of $0.0137''$. This parallax estimate does not match the trigonometric parallax of $0.00621'' \pm 0.00338''$ (Hipparcos 1997). The discrepancy appears to be attributable to inaccurate visual orbital elements, because the dynamical parallax depends weakly on the assumed masses but depends mainly on the period and semimajor axis of the orbit.

ADS 11791

The orbit of the visual binary system ADS 11791AB (HD 175039 = BD – 054798 = HIP 92726; G5; $V = 8\overset{m}{.}78$; $B-V = 0\overset{m}{.}72$; 2000: $18^h53^m42^s$, $-05°33'$)

Table 2. Radial-velocity measurements for ADS 10683

JDH 2400000+	V_r	σ	$O-C$	Component
	km s^{-1}			
50287.403	0.52	0.79	−0.19	Ba
50292.335	−48.54	1.29		A+Ba
50293.338	−0.04	1.93	1.38	Ba
50295.349	−51.29	0.98		A+Ba
50296.342	−82.99	0.76	−0.43	Ba
50297.335	−102.97	1.10	0.26	Ba
50298.351	−83.45	1.00	−1.56	Ba
50977.368	−27.21	0.78	1.75	Ba
50981.374	−90.51	0.85	0.28	Ba
50982.391	−103.06	1.30	−1.28	Ba
51008.355	−59.59	0.61		A+Ba
51067.225	−54.75	0.44		A+Ba
51071.210	−86.18	0.89	1.75	Ba
51706.418	−54.99	0.54		A+Ba
51707.403	−81.26	0.46	−0.17	Ba
51708.384	−105.31	1.11	−2.14	Ba
51710.464	−53.56	0.84		A+Ba
51711.371	−1.90	0.66	−0.88	Ba
51719.392	−2.41	1.34	−0.06	Ba
51720.363	−51.24	0.28		A+Ba
51722.336	−102.26	0.70	0.87	Ba
50293.338	−52.26	0.44		A
50296.342	−54.44	0.51		A
50297.335	−53.78	0.52		A
50298.351	−54.08	0.86		A
50301.327	−53.35	0.43		A
50977.368	−53.98	0.43		A
50981.374	−54.52	0.45		A
50982.391	−55.35	0.52		A
51069.211	−54.99	0.45		A
51071.210	−53.85	0.39		A
51707.385	−53.08	0.42		A
51711.357	−52.65	0.70		A
51719.403	−52.64	0.58		A

Table 3. ADS 10683. Line equivalent widths and the system model

Parameter	A	B
EW, km s^{-1}	1.49 ± 0.06	0.98 ± 0.08
Model		
ΔV	0.59	
$B-V$	0.73	0.82
M_V	5.07	5.66
EW, km s^{-1}	1.89	1.23

Table 4. Orbital elements for ADS 11791

Orbital element	Visual orbit of AB (Heintz 1998)	Spectroscopic orbit of Aa
P	258.00 yr	50.514 ± 0.004 days
T	1906.00	50011.5 ± 0.1
e	0.530	0.5921 ± 0.0051
a''	0.630	–
Ω_B, deg	178.7	–
ω_A, deg	–	135.6 ± 0.8
ω_B, deg	165.0	–
i, deg	41.0	–
K_A, km s^{-1}	–	21.96 ± 0.17
γ, km s^{-1}	–	-17.47 ± 0.11
f, $M_\odot$	–	0.0289 ± 0.0007

was computed by Heintz (1998). Its visual orbital elements are given in Table 4.

The systems spectrum clearly shows lines of only one component (for definiteness, we call it Aa). The velocity varies between -48 and -4 km s^{-1}. We were able to record a very weak secondary system of lines several times under good observing conditions. We cannot determine to which component these lines belong from our measurements. The radial velocities are listed in Table 5.

The orbit of the spectroscopic subsystem Aa is given in Table 4. For 28 observations, the measure of residuals is $\chi^2 = 30.71$ and the unweighted rms deviation is 0.476 km s^{-1}. The radial-velocity curve is shown in Fig. 2.

Let us estimate the system dynamical parallax. The mass of a normal G5-type dwarf is $0.93M_\odot$ (Allen 1973). According to the mass function, the mass of the secondary component of the spectroscopic subsystem is $M_{Ab} > 0.36M_\odot$. Since we failed to clearly observe lines of the secondary visual component, we may assume its mass to be no larger than $0.5M_\odot$. Under these conditions, we obtain a dynamical parallax of $0.0125''$. Our estimate matches the system trigonometric parallax of $0.01259'' \pm 0.00221''$ (Hipparcos 1997).

Table 5. Radial-velocity measurements for ADS 11791

JDH 2400000+	V_r	σ	$O-C$
	km s^{-1}		
50290.367	−10.20	0.17	0.24
50294.405	−8.13	0.50	0.13
50296.393	−7.63	0.34	−0.31
50297.355	−6.57	0.26	0.32
50326.360	−21.95	0.29	1.10
50327.264	−22.37	0.27	−0.52
50713.243	−6.99	0.30	0.10
50726.278	−31.03	0.38	−0.57
50730.219	−22.68	0.46	0.73
50981.448	−25.91	0.28	−0.45
51066.274	−6.16	0.24	0.19
51072.255	−42.28	0.36	−0.07
51075.292	−45.20	0.23	−0.51
51078.250	−34.02	0.41	0.57
51705.459	−10.91	0.46	−0.87
51708.461	−8.57	0.24	−0.14
51718.404	−4.79	0.31	0.05
51719.449	−5.51	0.27	−0.72
51720.452	−4.59	0.35	0.31
51725.468	−12.19	0.27	−0.01
51726.480	−17.32	0.34	0.33
51728.484	−37.97	0.28	−0.48
51729.453	−45.58	0.34	0.63
51730.495	−48.44	0.33	0.22
51734.486	−36.24	0.60	−0.35
51737.439	−27.98	0.48	0.60
51740.412	−23.93	0.39	−0.40
51741.411	−21.92	0.41	0.24

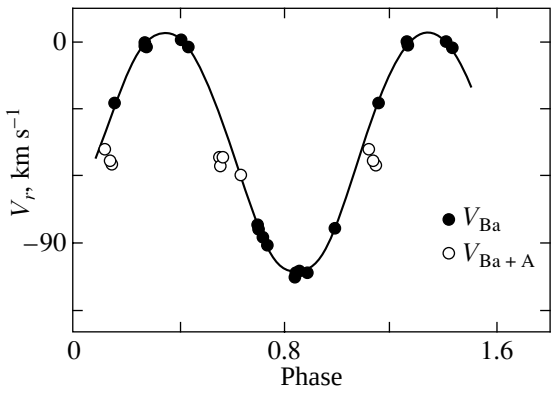

Fig. 1. The radial-velocity curve for ADS 10683Ba.

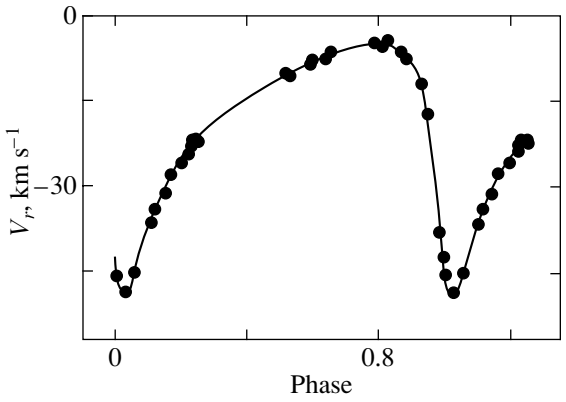

Fig. 2. The radial-velocity curve for ADS 11791.

CONCLUSIONS

We have investigated two new spectroscopic components in the visual binaries ADS 10683 and ADS 11791. We computed their spectroscopic orbital elements and constructed their radial-velocity curves.

ACKNOWLEDGMENTS

I am grateful to N.A. Gorynya, A.A. Tokovinin, and A.S. Rastorguev for help in obtaining the observational data.

REFERENCES

1. C. W. Allen, *Astrophysical Quantities* (Athlone Press, London, 1973; Mir, Moscow, 1977).
2. W. D. Heintz, Astrophys. J., Suppl. Ser. **117**, 587 (1998).
3. J. L. Newburg, Repub. Obs. Circ. **7**, 120 (1966).
4. M. G. Smekhov, Pis'ma Astron. Zh. **20**, 407 (1994) [Astron. Lett. **20**, 343 (1994)].
5. M. G. Smekhov, Pis'ma Astron. Zh. **21**, 445 (1995) [Astron. Lett. **21**, 396 (1995)].
6. M. G. Smekhov, Pis'ma Astron. Zh. **25**, 622 (1999) [Astron. Lett. **25**, 536 (1999)].
7. *The Hipparcos and Tycho Catalogues* (European Space Agence, 1997).
8. A. A. Tokovinin, Astron. Zh. **64**, 196 (1987) [Sov. Astron. **31**, 98 (1987)].
9. A. A. Tokovinin, Pis'ma Astron. Zh. **16**, 58 (1990) [Sov. Astron. Lett. **16**, 24 (1990)].
10. C. E. Worley and W. D. Heintz, Publ. Naval Obs. Second Ser. **24**, part 7, 1 (1983).

Translated by N. Samus'

Astronomy Letters, Vol. 28, No. 6, 2002, pp. 397–400. Translated from Pis'ma v Astronomicheskiĭ Zhurnal, Vol. 28, No. 6, 2002, pp. 452–456.

Observation of Quasi-Periodic Pulsations in the Solar Flare SF 900610

O. V. Terekhov[1*], A. V. Shevchenko[1], A. G. Kuz'min[1], S. Yu. Sazonov[1], R. A. Sunyaev[1], and N. Lund[2]

[1] *Space Research Institute, Russian Academy of Sciences, ul. Profsoyuznaya 84/32, Moscow, 117810 Russia*

[2] *Danish Space Research Institute, Copenhagen, Denmark*

Received January 24, 2002

Abstract—A quasi-periodic component was found at the maximum of the X-ray light curve for the June 10, 1990 solar flare detected by the Granat observatory. The pulsation period was 143.2 ± 0.8 s. The intensity of the pulsing component is not constant; the maximum amplitude of the pulsations is $\sim 5\%$ of the total flare intensity. An analysis of the data showed the characteristic size of the magnetic loop responsible for these pulsations to be $\sim (1-3) \times 10^{10}$ cm. © *2002 MAIK "Nauka/Interperiodica"*.

Key words: *solar flares, quasi-periodic pulsations, magnetic loops*

INTRODUCTION

The time history of the X-ray flux from the solar flare of June 10, 1990, recorded in two energy channels on the GOES-6 satellite with a time resolution of 1 min is shown in Fig. 1 (Solar Geophysical Data 1990). The X-ray class of this solar flare is M1.7.

The event SF900610 is one of the longest flares observed with the WATCH instrument on the Granat observatory. Its duration is about 2 h. According to WATCH data, the X-ray (8–20 keV) flare began at 21:39 (UT), reached a maximum at 22:10, and ended at 23:20.

The WATCH instrument, the idea of which was published by Schnopper *et al.* (1968), was devised at the Danish Space Research Institute (Lund 1981) and installed on the Granat observatory to detect transient X-ray sources (Brandt *et al.* 1994; Castro-Tirado 1994; Lapshov *et al.* 1994) and cosmic gamma-ray bursts (Sazonov *et al.* 1998). It was also used to investigate solar flares in the deca-keV range (Crosby *et al.* 1998). The WATCH instrument includes four detectors with $\sim 60^\circ$ fields of view directed along the tetrahedron axes and is an all-sky monitor capable of detecting radiation in the energy ranges 8–20 and 20–60 keV. Each detector can simultaneously localize several sufficiently bright X-ray sources within its field of view and determine their intensity. The WATCH/Granat detectors were installed in such a way that the Sun was always in the field of view of one of the detectors.

The Granat observatory came into operation (December 1989) when the solar cycle was at a maximum. In this period (1990–1991), several bright, high-energy solar flares were detected by the Granat instruments (Terekhov *et al.* 1996).

OBSERVATION OF QUASI-HARMONIOUS PULSATIONS IN THE LIGHT CURVE OF THE JULY 10, 1990 FLARE

This solar flare was detected by the WATCH instrument. Its WATCH light curve in the energy range 8–20 keV with a time resolution of 6.71 s is shown in Fig. 2a. In the energy range 20–60 keV, the WATCH detector recorded no significant excess in the count rate above the background level. This implies that the energy spectrum of the solar flare in the range 8–20 keV is very soft with a photon index of no more than 6. Assuming the Planck spectral shape, we find that the temperature of the radiating plasma cannot be >2 keV.

The WATCH high time resolution and the stable background due to the Granat high-apogee orbit make it possible to analyze in detail the light curves of detected events. It is of interest to search for quasi-harmonic signals in solar flares.

The spectrogram method, which consists in obtaining consecutive power spectra of the flare time history, was used to search for quasi-harmonic signals in the flare. Since the low-frequency radiation excess typical of X-ray transients was observed in the power spectrum, we used a low-frequency filtration of the time profile by the Savitzky–Golay method (Press *et al.* 1992a) with a 0.05 smoothing band, which corresponds to a 3.7 mHz spectral filter band.

[*] E-mail: tern@hea.iki.rssi.ru

1063-7737/02/2806-0397$22.00

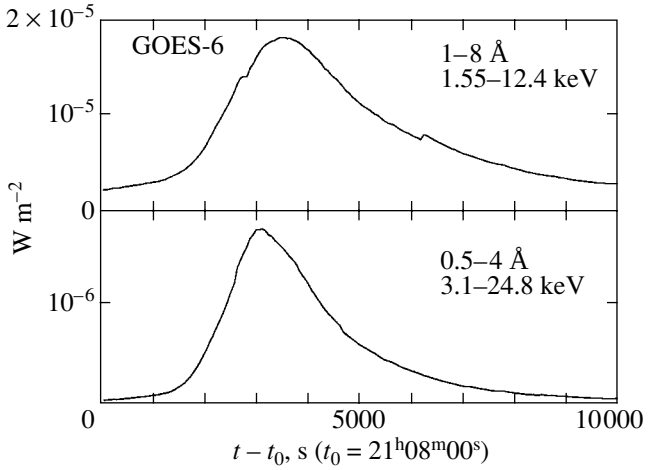

Fig. 1. Time history of the X-ray flux in two energy channels on the GOES-6 satellite (Solar Geophysical Data 1990).

The smoothing function was calculated by using quadratic polynomials and a biquadratic weighting function and then subtracted from the initial data. The data were normalized to the variance according to the formula

$$N_{\rm norm}(t_i) = N_{\rm data}(t_i)/(N_{\rm smooth}(t_i))^{1/2}, \qquad (1)$$

where $N_{\rm data}$ are the initial data in the counts integrated over the measurement interval and $N_{\rm smooth}$ are the smoothed data. The distribution of the normalized data is well fitted by a Gaussian law with a mean variance of 1.5. Note that in the absence of a signal and for a Poisson noise distribution, the variance would be equal to unity.

The power spectra were obtained by the Fast Fourier Transform (FFT) method at 215-s steps. The interval of each FFT sample was 256 bins or 1718 s to achieve a maximum signal-to-noise ratio. It corresponds to a frequency resolution of 0.58 mHz. Note that the spectral power noise distribution in the normalization under consideration corresponds to the χ^2 law with two degrees of freedom and with the mean and variance equal to unity. As follows from the spectrogram in Fig. 2b, a quasi-harmonic component with a frequency of $\sim$7 mHz shows up in the flare spectrum. It corresponds to a period of $\sim$143 s. The scale of gray in the figure is logarithmic. Note that, as we see from Fig. 2b, pulsations of lower intensity with other periods are present in the flare spectrum. At frequencies above 18.5 mHz, there is no appreciable excess above the background level determined by a unit variance. A detailed description of the algorithm will be published in Shevchenko *et al.* (2002).

The quasi-harmonic-signal parameters can be improved because of the high signal-to-noise ratio. We used the Levenberg–Marquardt nonlinear regression method (Press *et al.* 1992b) to fit the smoothed data with the function

$$F = A_0 + A\sin(2\pi t_i/T + \varphi_0)/(1 + ((t_i - t_0)/\Delta t)^2), \qquad (2)$$

which is a product of the sine and the Lorentz function. Here, A_0 is a constant intensity, A is the amplitude of the quasi-harmonic signal, t_i is the time, T is the period of the quasi-harmonic signal, φ_0 is the initial phase, t_0 is the time of the intensity maximum, and Δt is the width of the Lorentz profile. Using a Gaussian function yields similar results. The best fit to the data is shown in Fig. 3, where the vertical bars correspond to rms measurement errors of $\pm\sigma$. In this case, the coefficient of determination, which characterizes the model fit to the experimental data, is 0.89. The statistical significance (p-level) is less than 0.0001, i.e., the probability that the dependence found is coincidental is $<0.01\%$. The measured period of the quasi-periodic pulsations is 143.2 ± 0.8 s. Six intensity peaks with this period are observed at the maximum of the light curve. The intensity of the pulsing component is not constant and its maximum corresponds to the flare intensity maximum. The maximum pulse fraction is $\sim 5\%$ of the total flare intensity.

DISCUSSION

Millimeter observations of solar flares reveal quasi-periodic pulsations in their time profiles. The periods of the observed pulsations range from several seconds to several minutes. Zaitsev *et al.* (2001) analyzed low-frequency fluctuations in the intensity of microwave radiation from solar flares at frequencies of 22 and 37 GHz. Quasi-harmonic pulsations were also observed in the hard X-ray range. Bogovalov

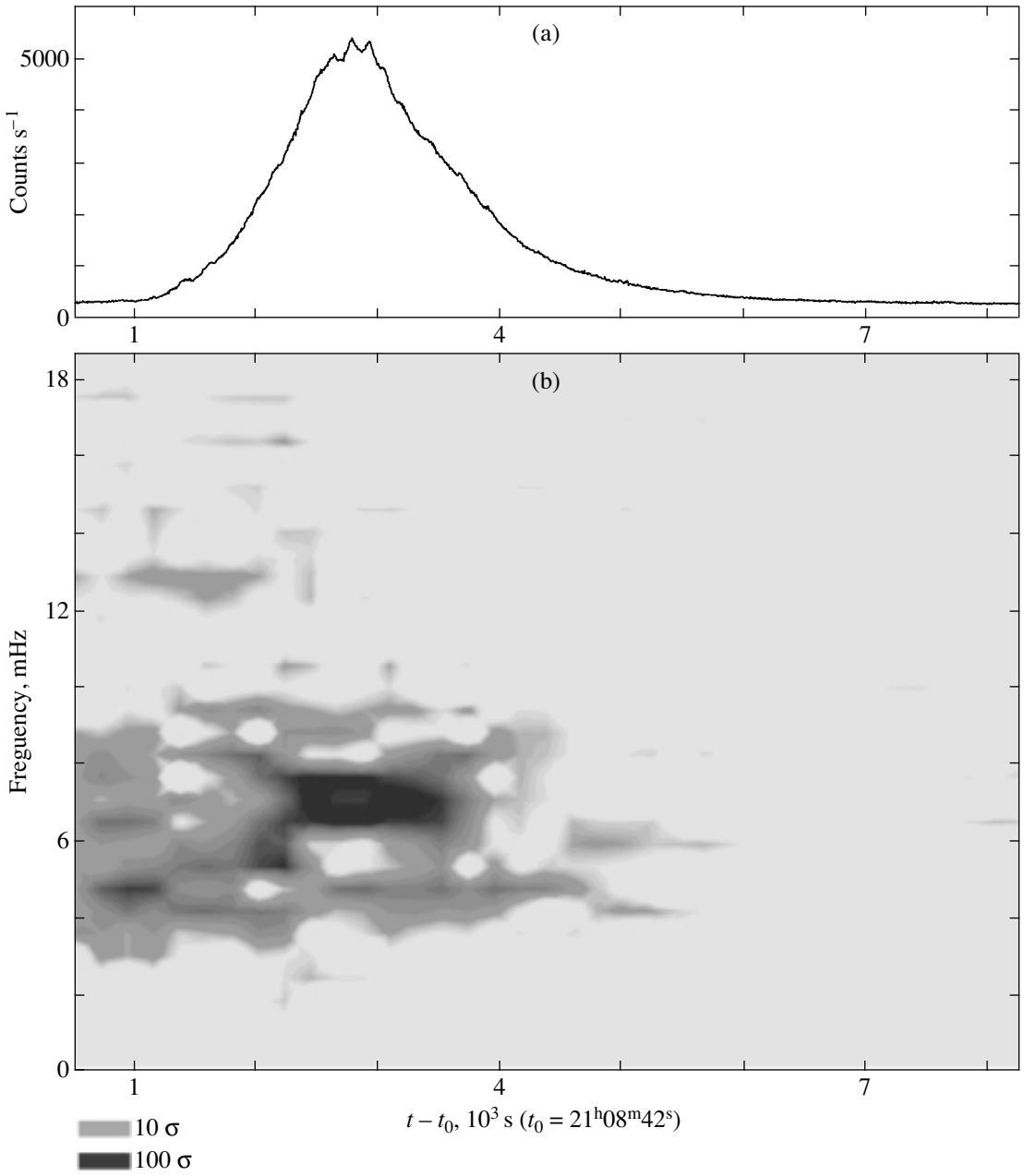

Fig. 2. Evolution of the spectral power for SF900610. The scale of gray in the figure is logarithmic, in units of standard deviations.

et al. (1983) reported the observation of quasi-periodic oscillations with periods of 1–2 s. Terekhov *et al.* (1995) considered the observations of quasi-periodic pulsations with periods of ~10 s from two bright solar flares at energies >100 keV. In this paper, we analyze the pulsations with a period of 143.2 s in the 8–20-keV light curve of the flare.

Zaitsev and Stepanov (1989) presented a model of quasi-periodic pulsations in solar flares. They suggested that centrifugal forces emerge because of the upward vertical motion of the evaporated plasma along curved magnetic field lines, which, in turn, generate Alfvén oscillations in the flare loop with typical periods from several seconds to several tens of seconds. In this case, the hard X-ray emission is assumed to originate from the loop footpoints. The measured parameters of the Alfvén oscillations provide information on the temperature and density of the evaporated plasma and on the magnetic field in the flare loop (Stepanov *et al.* 1992).

The period of the Alfvén oscillations depends on the loop length and the Alfvén velocity. The Alfvén

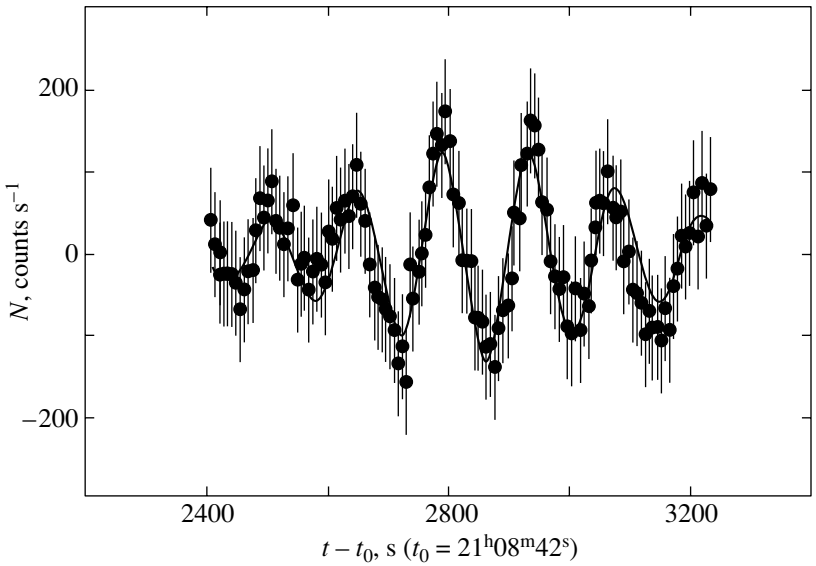

Fig. 3. The best fit to the pulsing-component data at the flare maximum.

velocity for coronal loops is of the order of $(1-2) \times 10^8$ cm s^{-1}. We may conclude that for SF900610, oscillations with a period of 143.2 s could arise in a loop with a length larger than 1×10^{10} cm.

Another estimate of the loop length can be obtained from the model by Stepanov *et al.* (1992). In this model, the temperature of the flare plasma in the loop is proportional to the depth of the X-ray pulsation modulation and to the square of the Alfvén velocity. Having a constraint on the flare plasma temperature (2 keV) and taking the modulation depth to be $\sim 5\%$, we can obtain a lower limit on the Alfvén velocity, $\sim 1.8 \times 10^8$ cm s^{-1}. For the observed pulsation period, this gives an upper limit on the loop length of $\sim 2.6 \times 10^{10}$ cm.

ACKNOWLEDGMENTS

This study was supported by the Russian Foundation for Basic Research (project no. 00-02-17251), the Program "Astronomy: Nonstationary Astrophysical Objects" of the Russian Academy of Sciences, the sixth Examination Competition in 1999, and the Science Support Foundation Grant for Talented Young Researchers. We are grateful to V.V. Zaĭtsev for valuable remarks.

REFERENCES

1. S. V. Bogovalov, A. F. Yudin, Yu. D. Kotov, *et al.*, Pis'ma Astron. Zh. **9**, 307 (1983) [Sov. Astron. Lett. **9**, 163 (1983)].
2. S. Brandt, N. Lund, and A. J. Castro-Tirado, AIP Conf. Proc. **307**, 13 (1994).
3. A. Castro-Tirado, S. Brandt, N. Lund, *et al.*, Astrophys. J., Suppl. Ser. **92**, 469 (1994).
4. N. Crosby, N. Vilmer, N. Lund, and R. Sunyaev, Astron. Astrophys. **334**, 299 (1998).
5. I. Yu. Lapshov, S. Yu. Sazonov, R. A. Sunyaev, *et al.*, Pis'ma Astron. Zh. **20**, 250 (1994) [Astron. Lett. **20**, 205 (1994)].
6. N. Lund, Astrophys. Space Sci. **75**, 145 (1981).
7. W. H. Press, S. A. Teukolsky, W. T. Vetterling, and B. P. Flannery, *Numerical Recipes in C. The Art of Scientific Computing* (Cambridge Univ. Press, Cambridge, 1992a), p. 650.
8. W. H. Press, S. A. Teukolsky, W. T. Vetterling, and B. P. Flannery, *Numerical Recipes in C. The Art of Scientific Computing* (Cambridge Univ. Press, Cambridge, 1992b), p. 681.
9. S. Y. Sazonov, R. A. Sunyaev, O. V. Terekhov, *et al.*, Astron. Astrophys. **129**, 1 (1998).
10. H. W. Schnopper, R. I. Thompson, and S. Watt, Space Sci. Rev. **8**, 534 (1968).
11. Shevchenko *et al.* (2002) (in press).
12. Solar Geophysical Data, http://rsd.gsfc.nasa.gov/goes/ (1990).
13. A. V. Stepanov, S. Urpo, and V. V. Zaitzev, Sol. Phys. **140**, 139 (1992).
14. O. Terekhov, R. A. Sunyaev, D. Denisenko, *et al.*, Lect. Notes Phys. **454**, 353 (1995).
15. O. V. Terekhov, A. G. Kuz'min, R. A. Sunyaev, *et al.*, Pis'ma Astron. Zh. **22**, 403 (1996) [Astron. Lett. **22**, 362 (1996)].
16. V. V. Zaĭtsev, A. G. Kislyakov, A. V. Stepanov, *et al.*, Radiofizika **44**, 38 (2001).
17. V. V. Zaĭtsev and A. V. Stepanov, Pis'ma Astron. Zh. **15**, 154 (1989) [Sov. Astron. Lett. **15**, 66 (1989)].

Translated by O. Terekhov

Astronomy Letters, Vol. 28, No. 6, 2002, pp. 401–410. Translated from Pis'ma v Astronomicheskiĭ Zhurnal, Vol. 28, No. 6, 2002, pp. 457–467.

Comprehensive Studies of Solar Activity on the CORONAS-F Satellite

V. N. Oraevsky[1]* and I. I. Sobelman[2]

[1] *Institute of Terrestrial Magnetism, Ionosphere, and Radio-Wave Propagation, Russian Academy of Sciences, Troitsk, Moscow oblast, 142090 Russia*

[2] *Lebedev Physical Institute, Russian Academy of Sciences, Leninskiĭ pr. 53, Moscow, 117924 Russia*

Received December 27, 2001

Abstract—The first results of comprehensive CORONAS-F observations of solar activity are presented. The CORONAS-F instrumentation and principal scientific objectives are briefly described and examples of the first results of data reduction are given. © *2002 MAIK "Nauka/Interperiodica".*

Key words: *Sun; astronomical observing techniques, equipment and instruments*

THE CORONAS PROGRAM AND THE CORONAS-F PROJECT

The CORONAS (Comprehensive Orbital Near-Earth Solar Activity Observations) International Program, as part of which the CORONAS-F near-Earth spaceborne solar observatory was launched, is intended for studies of the Sun at various phases of the 11-year solar cycle. On the previous CORONAS-I satellite (launched in 1994), the Sun was observed near the minimum of its activity. The CORONAS-F will study the solar activity near the maximum of the current cycle 23. On July 31, 2001, CORONAS-F was placed in an orbit with the following parameters: an orbital inclination of 82.49°, a minimum altitude of 500.9 km, a maximum altitude of 548.5 km, and a revolution period of 94.859 min. Such an orbit provides repetitive ~20 day-long periods of continuous solar observations, which is of particular importance in helioseismology and in patrolling solar flares. The actually achieved spacecraft attitude stabilization turned out to be a factor of 3 to 5 better than the projected one (a few arcseconds per second), which allows the spatial resolution of solar observations to be appreciably improved.

SCIENTIFIC OBJECTIVES OF THE CORONAS-F PROJECT

The principal scientific objectives of the CORONAS-F project are observations of global solar oscillations, investigation of the seismology of the solar interior and internal structure, comprehensive studies of powerful dynamical processes on the active Sun (active regions, flares, plasma ejections) over a wide wavelength range, from optical to gamma rays, including the radiation from solar cosmic-ray particles accelerated during active solar events, conditions for their escape, propagation in the interplanetary magnetic field, and impact on the Earth's magnetosphere.

SCIENTIFIC INSTRUMENTATION AND THE FIRST OBSERVATIONAL RESULTS

In accordance with the CORONAS-F objectives, the scientific instrumentation of the spacecraft includes four major groups of instruments: an instrument to detect global solar oscillations; X-ray instruments to image active regions on the Sun with a spatial resolution of ~2″–3″ instruments to measure the fluxes of electromagnetic radiation from active regions and flares; and instruments to study solar corpuscular fluxes. The wide range of measurements of the electromagnetic spectrum and solar cosmic-ray particle [both neutral (neutrons) and charged (electrons, protons, nuclei)] fluxes yields the fullest picture of the physical processes in active regions on the

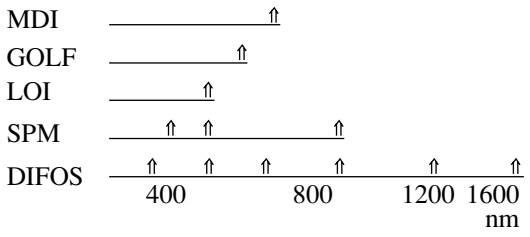

Fig. 1. Comparison of the DIFOS (CORONAS-F) channels with the SOHO instruments (MDI—Michelson Doppler Imaging of solar oscillations, GOLF—Global low-degree velocity, LOI—Luminosity Oscillation Imager, SPM—SunPhotoMeter).

*E-mail: oraevsky@izmiran.rssi.ru

1063-7737/02/2806-0401$22.00

Table 1. The CORONAS-F instruments

Instrument	Purpose	Designer	Principal investigators
	Helioseismology		
DIFOS spectrophotometer	Helioseismological monitoring	IZMIRAN	V.N. Oraevsky
	High-angular-resolution monochromatic imaging		
SRT-C X-ray telescope	Studying the spatial structure and dynamics of the upper solar atmosphere using narrow-band XUV images	FIAN	I.I. Sobelman I.A. Zhitnik
RES-C X-ray spectroheliograph	Diagnosing the hot solar atmospheric plasma using images in X and XUV spectral lines	FIAN	I.I. Sobelman I.A. Zhitnik
DIOGENESS spectrophotometer	Studying the X-ray radiation from solar active regions and flares	SRC PAS*	J. Silvestr
	Measuring the fluxes and polarization of electromagnetic radiation (from UV to γ rays)		
RESIK X-ray spectrometer	Studying the solar X-ray radiation with a high spectral resolution	SRC PAS*	J. Silvestr
SPR-N solar spectropolarimeter	Studying the polarization of X-ray radiation from solar flares	FIAN NIIYaF	I.I. Sobelman I.P. Tindo S.I. Svertilov
IRIS flare spectrometer	Studying the X-ray solar flare activity	FTI	G.E. Kocharov
GELIKON gamma-ray spectrometer	Studying the X-ray and gamma-ray solar flare activity	FTI	E.P. Masetz
RPS X-ray spectrometer	Studying the X-ray radiation from solar flares and their precursors	IKI RAS MIPhI	V.M. Pankov Yu.D. Kotov
ATS amplitude–time spectrometer	Studying the X-ray and gamma-ray radiation from solar flares	MIPhI	Yu.D. Kotov
SUVR-Sp-C solar ultraviolet radiometer	Studying the variations in total UV solar flux	IPG	T.V. Kazachevskaya
VUSS-L ultraviolet solar spectrophotometer	Studying the solar UV radiation near the L_α resonance line	IPG	A.A. Nusinov
	Studying solar corpuscular fluxes		
Instrumentation to study SCRs	Studying solar cosmic rays	NIIYaPh MGU	S.N. Kuznetsov
	Gathering and studying of scientific information		
Scientific Information Acquisition System (SSNI)	Controlling the scientific instrumentation and the modes of its operation	IZMIRAN	V.N. Ogaevsky A.I. Stepanov

* Space Research Center of the Polish Academy of Sciences.

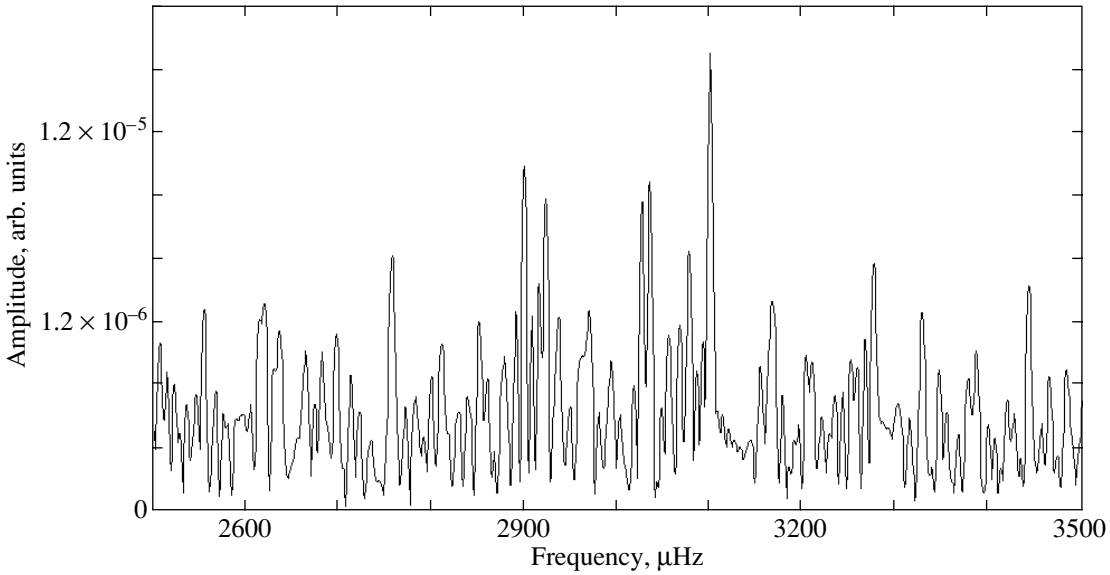

Fig. 2. The relative amplitudes of 5-min solar oscillation modes at a wavelength of 350 nm as inferred from the results of the DIFOS data reduction.

Sun. The CORONAS-F instruments and their main purpose are given in Table 1.

The main operational control of the scientific instrumentation is performed from the Flight Control Center located at the Cosmic Information Technology Center, Institute of Terrestrial Magnetism, Ionosphere, and Radio-Wave Propagation (IZMIRAN), Troitsk. Commands are sent to the spacecraft on a daily basis. Up to 24 kbytes of commands are sent simultaneously. Apart from controlling the modes of operation, the controllers of the scientific instruments are dynamically reprogrammed in flight, which allows their software to be customized for current observations. Requests for control through the Flight Control Center of the Cosmic Information Technology Center (IZMIRAN) are collected via E-mail with no less than 10 min before the control session, which ensures the required speed and flexibility in controlling the scientific instrumetation.

THE DIFOS SPECTROPHOTOMETER

The DIFOS spectrophotometer is designed to measure fluctuations in the intensity of solar optical radiation in an effort to obtain the spectrum of free oscillations. The intensity is simultaneously measured in six optical spectral bands: 350, 500, 650, 850, 1100, and 1500 nm with a band width equal to 10% of the central frequency. In comparison with the CORONAS-I project (Lebedev *et al.* 1995), the photometer was significantly upgraded: the detector sensitivity increased by more than an order of magnitude and the spectral range of observations was extended by almost a factor of 2; concurrently, the number of spectral channels increased from three to six. Global solar oscillations are being observed over a wide spectral range, including the most informative UV line. The intensity of the radiation from global solar oscillations in this line appreciably exceeds the radiation intensity in other lines (Oraevsky *et al.* 1999). Figure 1 compares the DIFOS channels with the SOHO instruments (1988).

Figure 2 shows the relative amplitudes of 5-min solar oscillation modes at a wavelength of 350 nm during November 28–30, 2001 as inferred from the results of the DIFOS data reduction. Similar results were obtained for the other channels. After averaging over the modes, the mean relative amplitudes were determined for each of the six channels and plotted against wavelength (see Fig. 3). All data points fall on a smooth curve fitted by a $\lambda^{-1.2}$ law (*1*). A

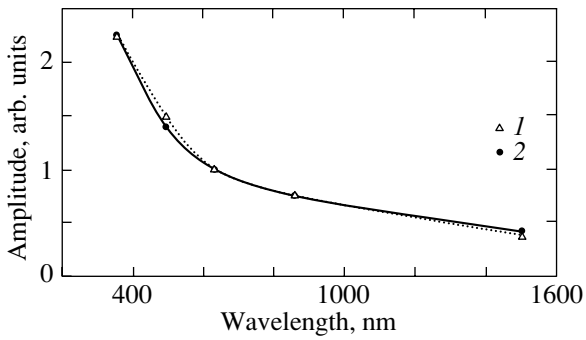

Fig. 3. The relative amplitude of free solar oscillations versus wavelength.

Table 2. Characteristics of the SRT-C telescope

Channel	Spectral range, Å	Ion lines	Field of view, arcmin	Angular scale per cell	Mode of operation
BP1	171	Fe IX–Fe X	42 × 48	2″.5	Full disk
	195	Fe XII			
	284	Fe XV			
	304	He II			
BP2	175	Fe IX–Fe XI	45 × 50	2″.6	Full disk, pointing at corona up to several solar radii
	304	HeII + SiXI	45 × 50	2″.6	
Optical sensors OS1 and OS2	4000–8000		Circular 11°	1′ × 2′	Stars $> 12^m$

similar result was established for another interval of observations, November 30–December 3, 2001 (*2*). A comparison of the DIFOS result with the results in the range of ground-based observations (Jimenez *et al.* 1998) gives close agreement. According to ground-based measurements, the amplitude ratio of global oscillations at wavelengths of 500 and 680 nm was 1.6, while for the DIFOS measurements, the amplitude ratio at 500 and 650 nm was 1.5. For a different pair of wavelengths, the amplitude ratio at 500 and 870 nm was 2.2 for ground-based observations, while the amplitude ratio at 500 and 850 nm for the DIFOS data was 2.

THE SPIRIT (SRT–RES–SPR) ASTROPHYSICAL COMPLEX TO STUDY THE SOLAR X-RAY RADIATION

The SPIRIT astrophysical complex consists of the SRT-C solar X-ray telescope, the RES-C X-ray spectroheliograph, and the SPR-N spectropolarimeter. It is designed to solve a wide variety of problems in solar physics based on XUV imaging spectroscopy of the Sun (soft X-ray and extreme UV solar spectroscopy). This method consists in obtaining simultaneously solar images and spectra with high angular and spectral resolutions in narrow portions of the XUV range that characterize the various temperature layers of solar plasma. It was applied in the CORONAS-I project, in which the TEREK-C multichannel telescope and the RES-C spectroheliometer in the wavelength range 0.18–30.4 nm designed at the Lebedev Physical Institute (Russian Academy of Science) were used (Sobelman *et al.* 1996; Zhitnik *et al.* 1998).

Observations with the SPIRIT astrophysical complex onboard the CORONAS-F satellite will allow the following processes to be investigated: the formation and development of solar flares from temporal variations and changes in the structure, spectra, and polarization of the flare regions; nonstationary phenomena in solar plasma (hot points, coronal mass ejections, and others)—the frequency of their occurrence, conditions for their emergence, dynamics of their development, and residual phenomena; and the helium distribution in the transition layer and in the near and far coronas. They also allow us to search for the possible sources of the solar wind, to study the processes of its generation, to elucidate the relationships of the observed solar-wind parameters to solar processes, and to diagnose the structural elements of active regions, areas of the quiet Sun, and coronal holes on time scales from 0.1 s to tens of days.

The SPIRIT complex is distinguished by a wide spectral range (0.04–100 keV) and by high spatial (up to 3″), spectral (up to 2×10^3), and temporal (0.01 s) resolutions intended for observations near maximum solar activity. The SRT-C telescope is a new instrument with significantly improved characteristics compared to the TEREK-C telescope that successfully operated on the CORONAS-I satellite. The working aperture of the optical channels increased from 30 to 100 mm with the simultaneous increase in actual angular resolution. The number of spectral subbands also increased. The RES-C-F spectroheliometer is a modification of the RES-C-I spectroheliometer that successfully operated on the CORONAS-I satellite with an extended spectral range and improved characteristics. In the SRT-C and RES-C-F instruments, the resolution and sensitivity of the imaging detectors were increased, their dynamical range was expanded, and a powerful high-performance computer with a large amount of random access memory was used in the electronic system. The new instruments provide an increase in temporal

Table 3. Characteristics of the RES-C X-ray spectroheliograph

Channel	Spectral range, Å	Ion lines	Spectral resolution, Å per cell	Angular scale per cell	Mode of operation
Fe XXV	1.85–1.87	Fe XXIV, FeXXV	1.5×10^{-4}	1′	Image and spectrum from the entire disk
Mg XII (two crossed subchannels)	8.41–8.43	Mg XII doublet	3×10^{-3}	4.1″	Same
XUV (two crossed subchannels)	176–205	Fe VIII, X, XI XII, XIII, XXIV, O VI S IX	0.03	6″ (perpendicular to dispersion)	Spectral images of the disk in all lines
	285–335	He II, Si XI			

resolution and sensitivity by up to a factor of 10 compared to the TEREK and RES instruments on the CORONAS-I satellite and by a factor of 3 compared to the EIT/SOHO telescope.

The SRT-C Solar X-ray Telescope

The SRT-C solar X-ray telescope is designed for X-ray imaging of the Sun with a high spatial resolution. It includes XUV channels, BP1 and BP2, and two optical sensors for the telescope attitude control using stars. The telescope characteristics are listed in Table 2.

X-ray mirrors with multilayer Mo–Si coating are used for imaging in the X-ray channels of the instrument: in channel BP1, a Ritchey–Chretien objective with a diameter of 120 mm and a focal length of 1660 mm that has four sectors with coverages at wavelengths of 171, 195, 284, and 304 Å (an analog of the EIT/SOHO telescope objective); and in channel BP2, off-axis paraboloids with a diameter of 100 mm and a focal length of 1500 mm.

The imaging detectors in all channels are CCD arrays; image intensifiers, which also act as electronic shutters, are used in the X-ray channels. The brightness dynamic range in the X-ray channels is of the order of 10^5. The exposure times can vary between 0.01 and 600 s.

The mirrors of channel BP2 are equipped with angular alignment and focusing systems to correct for possible changes in alignment when placing the satellite in orbit. In addition, the channel is supplied with artificial moons blocked by commands and with additional optical windows, which in combination with mirror deflection makes it possible to observe portions of the X-ray corona within several solar radii.

The RES-C X-ray Spectroheliograph

The RES-C spectroheliograph is designed to image the Sun in spectral lines of highly ionized atoms of abundant elements (helium, magnesium, iron, silicon) with a high spatial resolution and to measure the linear polarization in spectral lines. The instrument includes three XUV channels: Fe, Mg, and XUV. The RES-C characteristics are listed in Table 3.

X-ray optics is used in the RES-C instrument: in the Fe XXV channel, a ring Bragg mirror made of crystalline quartz with a sphere radius of 196.6 mm operating at a Bragg angle of 52°; in the Mg XII channel, two spherical Bragg mirrors made of crystalline quartz with a sphere radius of 1286 mm operating at angle 81.7°; in the XUV channels, two holographic diffraction gratings with a period of 3600 lines per mm whose spectra are focused on the detectors using multilayer Mo–Si-coated mirrors with a radius of 1600 mm were used: spherical and parabolic ones for the wavelength ranges 180–205 Å and 285–335 Å, respectively.

The imaging detectors in the XUV channels, just as those in the SRT-C instrument, are CCD arrays in combination with image intensifiers. The dynamic range is of the order of 10^5 and the exposure time ranges from 0.01 to 600 s. In the Mg XII and Fe XXV channels, X-ray radiation is recorded by the open CCD arrays.

The SPR-N Solar Spectropolarimeter

The SPR-N solar X-ray spectropolarimeter measures the polarization of continuum X-ray radiation from solar flares in the spectral range 20–100 keV (nonthermal radiation from the accelerated electrons generated in flares). The instrument has the following characteristics:

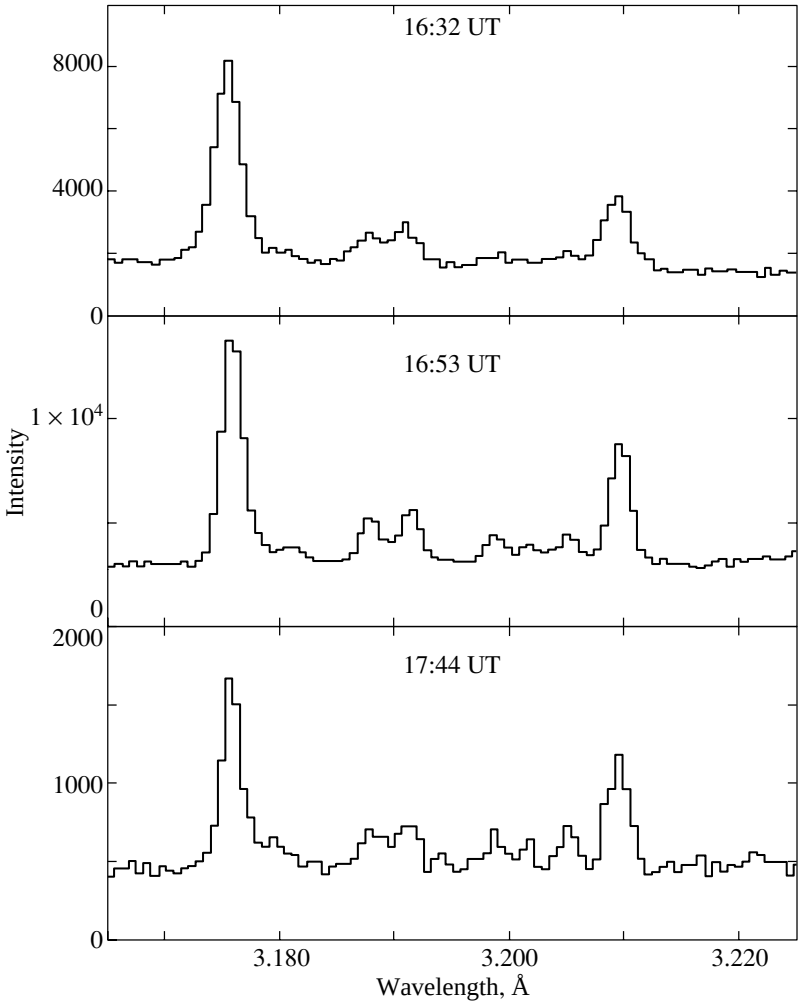

Fig. 6. Ca XIX line spectra with a high spatial resolution ($\sim 5''$) at the growth phase, intermediate phase, and the decay phase of the strongest flare in the current solar cycle (August 25, 2001).

Spectral range	20–100 keV
Subbands	20–40 keV
	40–60 keV
	60–100 keV
Polarization detection sensitivity	~5% at flux 10^{-6} erg cm^{-2} s^{-1}
Temporal resolution	4–16 s

The SPR-N instrument has two detection channels: a polarization detector and a patrol detector. The polarization detector contains an X-ray radiation scatterer (a hexahedral Be prism) and a system of three pairs of scintillation detectors (SSD), which measure the intensity of the scattered radiation. CsI(Na) crystal scintillators with photomultipliers are used to record X-ray radiation. To eliminate the systematic errors during polarization measurements attributable to the possible sensitivity drift in individual channels, the polarization detector was mounted on a turning drive. For typical solar flares of importance I, II, and III, the expected sensitivity of polarization measurement is ~5% at a flux of $\sim 10^6$ phot. cm^{-2} s^{-1} ($E = 20$–100 keV) and an integration time of ~8 s. The patrol detector is designed to measure the total intensity of the X-ray radiation from solar flares at energies 20–100 keV. It consists of a CsI(Na) crystal placed behind an anticoincidence shield and a photomultiplier.

Apart from the general scientific program of the CORONAS-F project, the programs of joint observations with instruments on other spacecraft that will operate simultaneously with CORONAS-F, primarily with instruments on the SOHO international spaceborne observatory, the TRACE telescope, YOHKOH, and others, are envisaged. It is planned that the CORONAS-F observations will be coordinated with

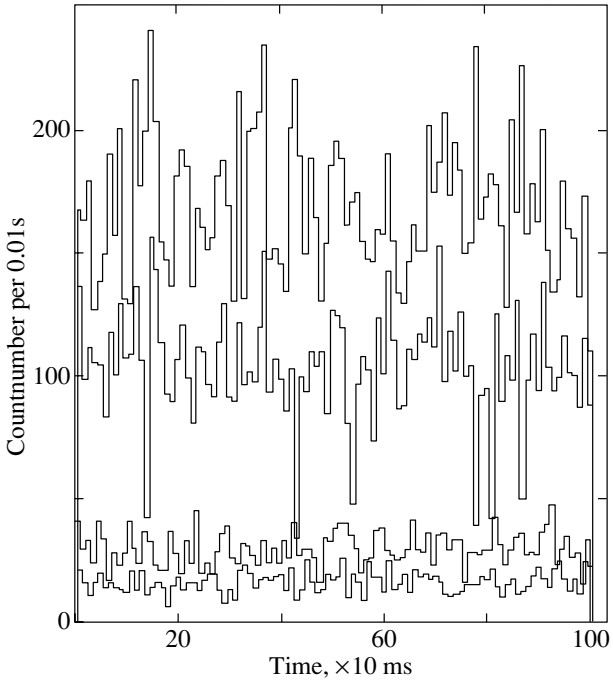

Fig. 7. An intensity record of hard X-ray radiation on September 27, 2001, 18:26 UT in the energy range 20–100 keV with a high temporal resolution in four energy channels (from top to bottom: 20–25, 25–35, 35–100, and 100–200 keV).

observations at ground-based observatories, in particular, with the Institute of Solar–Terrestrial Physics (Itkutsk), the Crimean Astrophysical Observatory, and other ground-based observatories that carry out solar observations.

Test experiments and preliminary scientific results obtained during the first three months of observations show that the entire instrumentation of the SRT–RES–SPR operates normally. Figure 4 shows the solar images at 171, 195, 284, and 304 Å obtained in channel BP1 of the SRT-C instrument. Figure 5 shows the spectroheliogram in the range 285–335 Å taken in the XUV channel of the RES-C instrument.

THE DIOGENESS SPECTROPHOTOMETER AND THE RESIK X-RAY SPECTROMETER

The RESIK and DIOGENESS instruments measure the solar spectra in the wavelength range 3–7 Å. They are designed to investigate the X-ray radiation from active regions and flares with a high spectral resolution. Their solar X-ray spectra are comparable in spectral and temporal resolution to the best observations performed to date. Because of the CORONAS-F polar orbit and the complete coverage of a wide spectral range, they are a valuable complement to the Yohkoh spectra. Since the detectors of the RESIK instrument and the Yohkoh spectrometers are saturated at high X-ray fluxes, the DIOGENESS instrument is currently the world's only operating spectrometer that takes the spectra of intense flares of importance above M2 (as exemplified by the X5.3 flare on August 25, 2001).

Figure 6 shows Ca XIX line spectra with a high spatial resolution ($\sim 5''$) at the growth phase, intermediate phase, and the decay phase of the strongest flare in the current solar cycle (August 25, 2001). The temperature of the emitting plasma decreases from 2.5×10^6 K at the growth phase to 1.2×10^6 K at the decay phase. The spectra exhibit changes in the line width, which points to the role of plasma turbulence during the flare evolution. A detailed analysis of the relative intensities will allow one to study the energy balance in flares and the role of non-Maxwellian and nonequilibrium processes in the flare energy release region. In the spectral range in question (3–7 Å), such spectra for an X flare were obtained with such a high spatial resolution for the first time. They provide information on the many emission lines produced by the collisional excitation of atoms, the excitation of inner atomic shells, and dielecton recombination.

THE IRIS FLARE SPECTROMETER

The instrument is designed to investigate the solar flare activity in the X-ray spectral range 2–200 keV. It has 12 energy channels with a temporal resolution of 2.5 s in patrol mode and 64 energy channels with a temporal resolution of 1 s and four channels with a 10 ms resolution in burst mode. As yet no

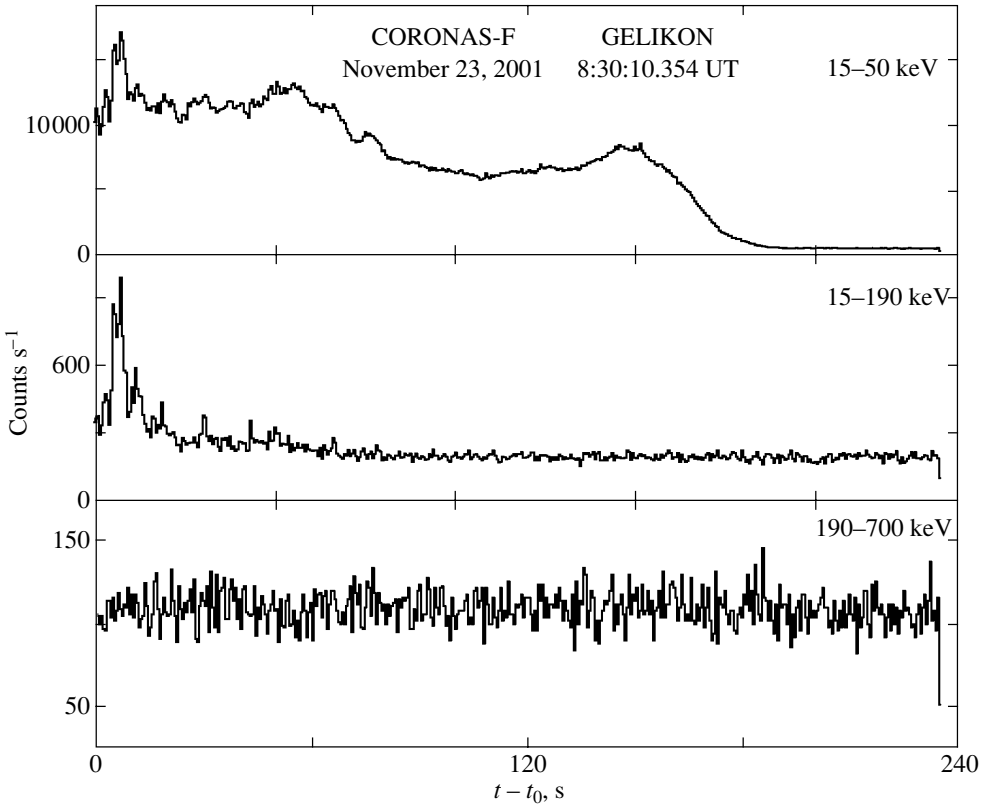

Fig. 8. The time profile for the intense solar flare of November 23, 2001, in three energy bands with a high temporal resolution, from 2 to 256 ms.

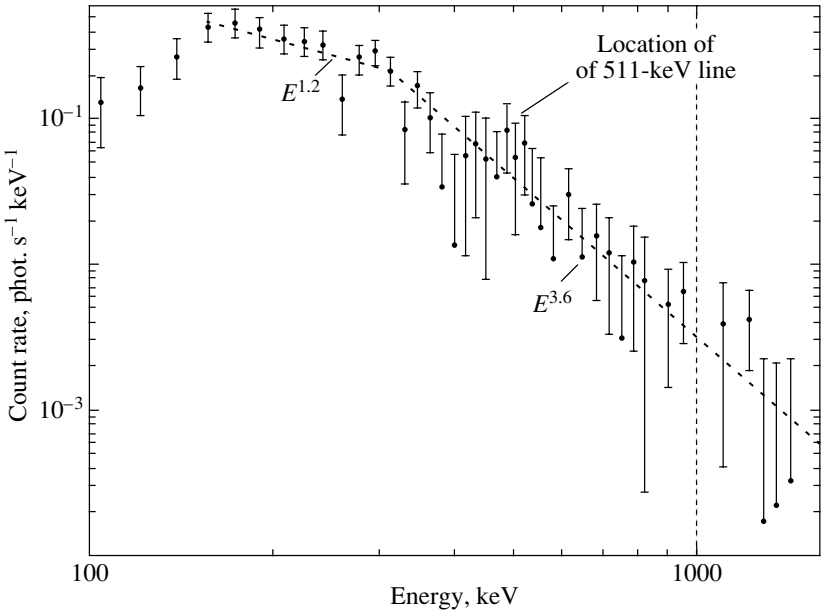

Fig. 9. The differential energy spectrum for the September 18, 2001 event.

spectral measurements have been carried out with such a temporal resolution in any experiment aimed at investigating the solar X-ray radiation. Observations of the fine temporal structure in hard X-ray fluxes will provide direct information on the development of the energy release at the explosive phase of flares. Figure 7 shows an intensity record of hard X-ray radiation in four energy channels in the range 20–100 keV with a high temporal resolution for the event of September 27, 2001, 18:26 UT.

THE GELIKON GAMMA-RAY SPECTROMETER

The instrument measures the temporal and spectral characteristics of the hard electromagnetic radiation from solar flares over a wide energy range, from X-rays to gamma-rays (10 keV–10 MeV). It is used to monitor the radiation conditions and soft solar flares and to detect and record in detail hard ($E\gamma > 50$ keV) flares and gamma-ray bursts. Over the observing period from November 14 through December 14, 2001, the temporal profiles and spectra were measured for 134 solar flares. Most of them had soft spectra and were recorded in background mode with a temporal resolution of 1 s in eight adjacent energy bands from 15 to 200 keV. Figure 8 shows the temporal profile for the intense solar flare of November 23, 2001, detected in trigger mode in three energy bands with a high temporal resolution from 2 to 256 ms.

THE RPS-1 X-RAY SPECTROMETER

The instrument is designed to investigate solar flares and their precursors in the X-ray range 3–30 keV. Over the period of measurements, the instrument calibration parameters were refined, the background conditions were mapped, and the experimental data statistics was accumulated. No SOHO measurements are carried out in this energy range, while the SXS/Yohkoh results have not yet been published.

THE ATS AMPLITUDE–TIME SPECTROMETER

The instrument is designed to study the X-ray and gamma-ray radiation from solar flares, in particular, to analyze solar-flare or gamma-ray burst events in the energy bands 3–30 keV, 0.1–8.0 MeV, and 2.0–80.0 MeV. Over the observing period, several tens of candidates for solar-flare or gamma-ray burst events were recorded and their energy spectra were obtained for various phases of the event (before, during, and after the event). The duration of the candidate events ranges from 16 s to 3–5 min. In Fig. 9, the differential energy spectrum for the event of September 18, 2001, was reconstructed from measurements. It exhibits a kink near energy 300 keV and a possible spectral feature that can be identified with the 511-keV annihilation line.

THE SUVR-Sp-C SOLAR ULTRAVIOLET RADIOMETER

The SUVR-Sp-C instrument measures the fluxes from the Sun as a star in several spectral bands, from 1 to 130 nm. In contrast to SOHO, it has a *wider* spectral range. Apart from the scientific objectives, the radiometer monitors one of the most important elements of cosmic *weather*—the geoeffective solar radiation. the SUVR obtained data on the intense X5.3B flare of August 25 at 16:23 UT at X-ray wavelengths $\lambda < 12$ nm.

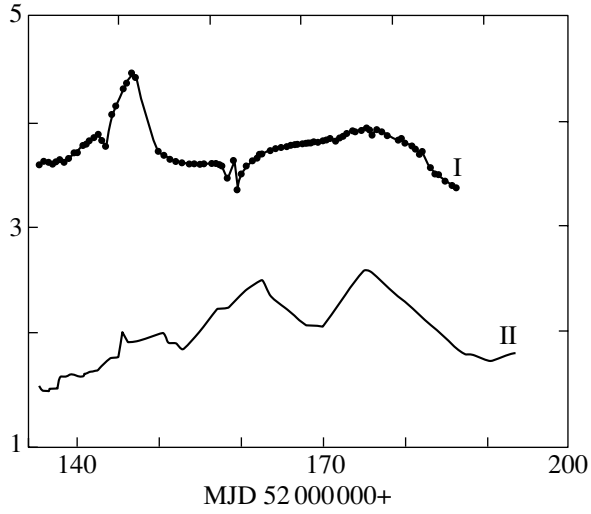

Fig. 10. The VUSS-L temporal record of a signal proportional to the solar UV flux (I) and the solar radio flux at a wavelength of 10.7 cm (II).

THE VUSS-L ULTRAVIOLET SOLAR SPECTROPHOTOMETER

The VUSS-L instrument carries out measurements in a band near 120 nm and is designed to investigate the solar ultraviolet radiation near the L_α resonance line. The measurements yield numerous data on the UV flux and intensity in the L_α line, which was tentatively estimated to be $\sim$10 erg cm^{-2} s^{-1}. The VUSS-L temporal record of the UV flux is shown in Fig. 10.

THE SCR INSTRUMENTATION TO STUDY SOLAR COSMIC RAYS

The SCR scientific instrumentation consists of three instruments: SONG (gamma-ray and neutron spectrometer, principal investigator S.P. Ryumin), CRM (cosmic-ray monitor, principal investigator S.N. Kuznetsov), and CRS-3 (cosmic-radiation spectrometer, principal investigator A.F. Podorol'skii). It is designed for comprehensive studies of solar cosmic rays. The SONG instrument records X-ray and gamma-ray spectra in the energy range 0.03–100 MeV, detailed gamma-ray line spectra in the range 0.3–20 MeV, neutrons with energies >20 MeV, and fluxes of charged cosmic-ray particles — protons with energies >70 MeV and electrons with energies

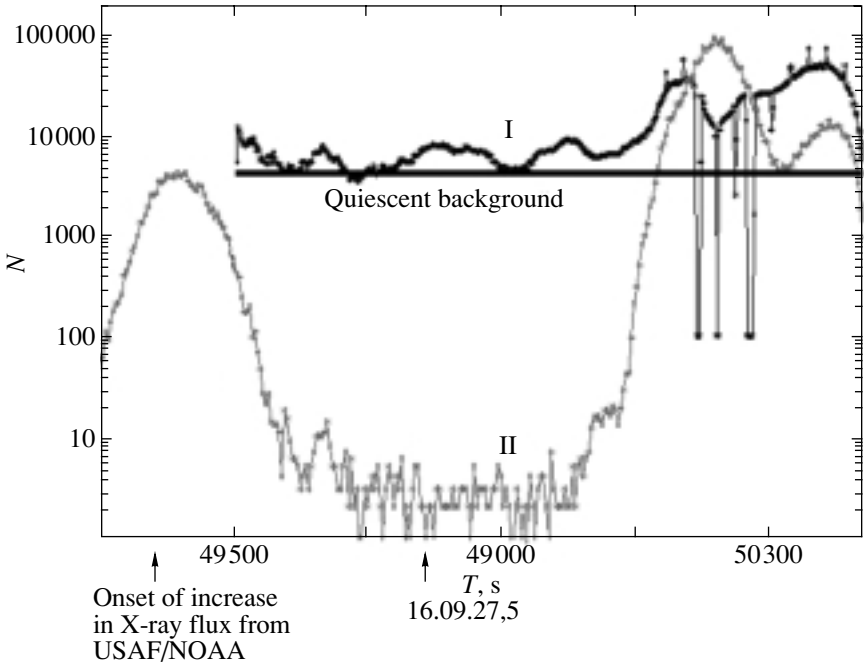

Fig. 11. The recording of gamma rays with energy 60–150 keV (I) and electrons with energy 0.3–0.6 MeV (II) by the SCR complex in the November 4, 2001 event.

>50 MeV. The SRM instrument measures the fluxes and spectra of protons with energies 1–200 MeV and electrons with energies 0.5–12 MeV. The CRS-3 measures the chemical composition and spectra of ions in the range $Z = 1$–10 and in the energy range 1.5–20 MeV per nucleon for He and 4–40 MeV per nucleon for Ne. In comparison with the SOHO and Yohkoh instruments, the SONG spectrometer is capable of recording energetic (with energies up to 100 MeV) gamma-rays, which, in turn, makes it possible to observe gamma-rays from the decay of the π^0 mesons produced in interactions of high-energy protons. The CORONAS-F measurements show that the SONG background for recording solar neutrons is at least a factor of 5 to 7 lower than that of GRS (SMM) — the only instrument that recorded solar neutrons in the same energy range. Figure 11 shows the SONG recording of gamma-rays with energy 60–150 keV (I) and electrons with energy 0.3–0.6 MeV (II). The first increase in gamma-ray flux correlates with the electron flux and can be explained in part as electron bremsstrahlung. The two remaining increases represent solar flare radiation. Since the flare occurred in the western hemisphere, the recorded increase in relativistic particle flux began almost immediately.

ACKNOWLEDGMENTS

V.D. Kuznetsov and I.A. Zhitnik played a major role in designing the CORONAS-F complex. They also helped in writing this paper, for which we thank them. We are also grateful to T.V. Kazachevskaya, Yu.D. Kotov, G.E. Kocharov, S.N. Kuznetsov, N.I. Lebedev, E.P. Masetz, A.A. Nusinov, V.M. Pankov, A.F. Podorol'skii, S.P. Ryumin, and J. Silvestr, who provided the reduced data from the CORONAS-F satellite.

REFERENCES

1. A. Jiménez, P. L. Palle, T. Roca Cortes, and V. Domingo, Astron. Astrophys. **193**, 298 (1988).
2. N. I. Lebedev, V. E. Oraevsky, Y. D. Zhugzda, *et al.*, Astron. Astrophys. **296**, L25 (1995).
3. V. N. Oraevsky, N. I. Lebedev, I. M. Kopaev, *et al.*, oral communication (1999).
4. I. I. Sobelman, I. A. Zhitnik, and A. P. Ignat'ev, Pis'ma Astron. Zh. **22**, 604 (1996) [Astron. Lett. **22**, 539 (1996)].
5. *The SOHO Mission: Scientific and Technical Aspects of the Instruments* (ESA, Paris, 1988), ESA SP-1104.
6. I. Zhitnik, A. Ignatiev, V. Korneev, *et al.*, Proc. SPIE **3406**, 1 (1998).

Translated by V. Astakhov

Astronomy Letters, Vol. 28, No. 6, 2002, pp. 411–418. Translated from Pis'ma v Astronomicheskiĭ Zhurnal, Vol. 28, No. 6, 2002, pp. 468–476.

Acoustic Power Mapping for Active Regions from MDI, HLH, and TON Data

O. V. Ladenkov[1,2*], F. Hill[2], Sh. A. Egamberdiev[1], and D. Y. Chou[3]

[1] *Astronomical Institute, Academy of Sciences of Uzbekistan, Astronomicheskaya ul. 33, Tashkent, 700052 Uzbekistan*

[2] *National Solar Observatory, National Optical Astronomical Observatories, Tuson, Arizona, USA*

[3] *Tsing Hua University, Hsin-chu, Taiwan*

Received March 28, 2001; in final form, January 17, 2002

Abstract—Based on the HLH and TON ground-based helioseismological projects and the SOHO/MDI spaceborne project, we obtained acoustic power maps of active regions averaged over 1 mHz intervals. These maps allowed the spatial and frequency distributions of acoustic power in an active region and its surroundings to be studied. The time step of the HLH data is 42 s, which makes it possible to investigate the acoustic power up to 11.9 mHz. Data in the Ca II K and Ni I lines, which originate in the middle chromosphere and the photosphere, respectively, give an idea of the height distribution of acoustic oscillation energy in the solar atmosphere. The acoustic halo produced by excess acoustic power around sunspots clearly shows up on acoustic maps in the Ca II K line and, to a lesser degree, in the Doppler Ni I line shifts. Ground-based observations also reveal a large enhancement of acoustic power inside sunspots. Our tests show that this effect results from the combination of a high intensity gradient in the data and atmospheric seeing. The latter was reduced by referencing each image to the sunspot. The spatial distribution of power inside the sunspot due to atmospheric seeing was found to depend on the exposure time of the data used. Excluding the nonsolar effects, a common property of all acoustic maps is the suppression of the solar-oscillation acoustic power in active regions. © *2002 MAIK "Nauka/Interperiodica"*.

Key words: *Sun, solar oscillations*

INTRODUCTION

The solar acoustic oscillations are stochastically generated by turbulent convection. They propagate in the solar interior, showing up on the visible solar surface as amplitude fluctuations in intensity and Doppler shifts. High-order oscillations, the so-called local solar modes, allow the parameters of the solar matter localized in small areas of the solar surface to be investigated. Thus, for example, the strong magnetic fields of active regions and the temperature inhomogeneities around sunspots tangibly affect the acoustic waves interacting with them. In particular, the magnetic fields of active regions were found to absorb 30–50% of the incident power (Braun *et al.* 1987). In addition, the acoustic power maps constructed from a Ca II K filtergram exhibit an enhancement of power around sunspots (halo) (Braun *et al.* 1992; Toner and LaBonte 1993). A slightly more patchy structure of enhanced acoustic power was also detected by Brown *et al.* (1992) using the velocities measured in the Fe I λ5576 Å line and MDI data for the Doppler velocities in the Ni I λ6768 Å line (Hidman and Brown 1998). However, the latter authors found no evidence of a halo for the MDI intensity data. It should be noted that the above lines originate from different levels of the solar atmosphere. The Ni I λ6768 Å and Fe I λ5576 Å lines span a small height range near the photosphere and the temperature minimum, whereas the Ca II K line originates in an extended region in the middle chromosphere. In previous studies with ground-based observations, insufficient attention was given to the influence of the Earth's atmosphere, which produces image tremor for short-exposure data. The latter causes an enhancement of power on acoustic maps, particularly for the combination of seeing with a high intensity gradient in sunspots and facular plages. We also consider unstable image focusing, which is of particular interest in data with a long exposure that causes the sunspot profile to change. Such a power enhancement on acoustic maps produced by nonsolar effects can occasionally be erroneously interpreted as a manifestation of the solar nature, leading to an incorrect understanding of some phenomena.

*E-mail: oleg@astrin.uzsci.net

1063-7737/02/2806-0411$22.00

OBSERVATIONS AND DATA ANALYSIS

The data used to construct acoustic power maps are daily series from several instruments, which include the following: intensity and Doppler-shift images in the Ni I λ6768 Å line obtained with the MDI (Michelson Doppler Imager) instrument (Scherrer *et al.* 1995) operated onboard the SOHO (Solar and Heliospheric Observatory) spacecraft and HLH (High-l Helioseismometer) filtergrams in the Ca II K line taken at the Kitt Peak Observatory (USA, Arizona). The two series were obtained on May 14, 1997, and have the same spatial resolution of $\sim 2''$. For our analysis, we took the unipolar active region NOAA 8038 located near the solar limb. In the MDI images, it consists of one leading sunspot and a group of small sunspots without penumbrae. In contrast, only the leading sunspot shows up in the HLH images, while the small sunspots are hidden by facular plages. To compare the acoustic power maps in the same spectral line but with different instruments, we used the TON data obtained in Tashkent on August 2, 1996. Their exposure time is 0.8 s, in contrast to 42 s for the HLH instrument. For the TON data, the active region NOAA 7981 was used for acoustic mapping. The MDI (Michelson Doppler Imager) is a modified Fourier tachometer tuned to the Ni 676.8 nm line. The detector is a 1024×1024 CCD array with two modes of operation: low-resolution (2 arcsec/pixel) and high-resolution (0.6 arcsec/pixel) modes. The observations yielded Dopplerograms, continuum and Ni-line intensities, and solar magnetograms.

The HLH instrument obtains 1024×1024 images in the Ca II K line with a spatial resolution of $2''$. The exposure time and the time step are 42 s.

The TON (Taiwan Oscillation Network) data are Ca II K line filtergrams with a spatial resolution of $\sim 1.8''$ and an exposure time of 0.8 s. A more complete description of the project and the instrument can be found in Chou *et al.* (1995). The table gives the data used here. The shorter HLH data series ($\sim$ 2 h) corresponds to part of the more complete series (1010 images) but with a relatively stable seeing. The series dimension made up of three numbers is the spatial dimension in pixels (128×128) and the series length equal to the number of images.

The general procedure for preliminary data reduction and acoustic power mapping can be described by the following steps:

(1) Data selection.

(2) Flat fielding and dark-current subtraction.

(3) Isolating a 128×128 pixel field by allowing for the differential rotation with respect to the field center followed by its remapping onto the plane with a spatial step of 0.1 heliographic degrees, where limb darkening is taken into account for each cutout field.

(4) Two-point temporal filtering for each pixel to remove the long-period variations caused by nonoscillatory processes. The two-point filtering involves subtracting each image from the succeeding one. In this case, such low-frequency processes as granulation are suppressed and the high-frequency acoustic signals are preserved.

(5) Spatial referencing of each image obtained in the ground-based HLH and TON experiments to the fixed position of the central sunspot by cubic interpolation.

(6) Performing a Fourier transform in temporal dimension for each individual pixel for the frequency representation of the power distribution and obtaining a power spectrum for each of these time series.

(7) Integrating the spectrum over 1 mHz frequency intervals and acoustic power mapping.

RESULTS AND DISCUSSION

We summed our acoustic power spectra in different spectral lines over 1 mHz frequency intervals, while in previous studies, the summation was performed over wider frequency ranges. This makes it possible to detect subtler variations in power over frequencies. To be sure that we investigate the power of precisely acoustic oscillations, we constructed the power spectra in time averaged over all pixels. The spectral profile with a power enhancement at 3 mHz, a rise in the noise level at high frequencies, and the suppression of power at low frequencies because of the two-point filtering is characteristic of the solar acoustic spectrum. Figure 1 shows acoustic power maps for the MDI intensity and Doppler-shift data. In all frequency ranges, a decrease in acoustic energy is observed in the regions corresponding to the locations of sunspots and, to a lesser degree, facular plages. The region under consideration lies near the solar limb, which is of greater interest from the viewpoint of the effect that was previously noted by Hidman and Brown (1998). These authors pointed out that the acoustic power estimates for the MDI Doppler-shift and intensity data differ, because they assumed that when the magnetic areas are located near the disk center, the velocity fluctuations are most pronounced along magnetic field lines, causing an enhanced power compared to the intensity data. Nevertheless, as in Hidman and Brown (1998), we may note a slight enhancement of acoustic power around sunspots, the so-called halo, in the frequency range 5–7 mHz only for the velocity measurements. The bright ring on the map for the range 0–1 mHz resulted from the evolution of the active region and the sunspot proper motion. Figure 2 shows power maps for the HLH data for the complete series of 1010 images. We see from Fig. 2 that there is a sharp

Table

Data	Spectral line	Series dimension	Resolution, arcsec	Exposure	Time step	Filling factor, %
				s		
MDI	Ni I	128 × 128 × 1024	1.97	1.0	60	85
HLH	Ca II K	128 × 128 × 1010	2.0	42	42	100
HLH	Ca II K	128 × 128 × 158	2.0	42	42	100
TON	Ca II K	128 × 128 × 322	1.8	0.8	60	100

enhancement of power in the central region that corresponds to the sunspot location, which is in conflict with the MDI results. During our work, we noted that the sunspot location was moderately stable, which may result from an inaccurate determination of the image center and the disk radius during our preliminary data reduction. To eliminate these effects, which change the sunspot location, we computed the sunspot geometrical center in each image and referenced each image to the derived location. Thus, the power at the sunspot center was reduced, but the excess in power still remained. Analysis of the sunspot profile revealed that it was very unstable (Fig. 3), particularly in the central part, which gives rise to an extra power. The acoustic power maps constructed from the MDI data for the same time interval and the same sunspot (Fig. 1) provide evidence that the sunspot itself underwent no changes. Consequently, the change in the sunspot profile may be assumed to be caused by atmospheric seeing conditions. To make sure that this is the case, we separately analyzed a ~2-h-long series of morning data with a relatively stable seeing, when the atmospheric transparency at Kitt Peak is believed to be best. One of such power maps in the frequency range 3–4 mHz is shown in Fig. 2 (pos. B). We see no power enhancement in the sunspot central region. Of course, this series is clearly too short to detect subtle halo-like effects, but the above example clearly points to the cause of the appearance of power enhancement in acoustic power maps. However, what causes the sunspot profile to change is still an open question. We offer the following explanation. Our data series were analyzed for image quality or sharpness. Clearly, small fluctuations and features are seen on sharp images, while small features on blurred images are washed out or smoothed out. Since the sunspot in the HLH data has a small angular size, image blurring must also affect the sunspot profile, causing the profile to be smoothed out and, hence, increasing the minimum intensity in the sunspot. We chose the total power of the spatial Fourier spectrum as the image quality criterion. The presence of small-scale fluctuations gives rise to an extra power in the Fourier spectrum. As a result, sharp images have a higher total fluctuation power than blurred images. This assumption was tested visually and modeled with a set of sine waves that simulated solar-surface fluctuations. It should be noted that before determining the power of the spatial Fourier spectrum, we zeroed the intensities in the sunspot region to eliminate the effect of different sunspot profiles. Thus, we obtained two series of results: data on the total fluctuation power for each image and data on the minimum intensity in the sunspot. These series were analyzed for a correlation, which proved to be fairly high (~ -0.75). These series strongly anticorrelate and, hence, there is a direct correlation between the sunspot profile and image quality. This, in turn, explains the appearance of an excess power in the sunspot region on acoustic power maps as resulting from seeing fluctuations.

Whereas atmospheric seeing for short-exposure data causes the images to shift, these shifts for data with a long exposure (42 s for the HLH data) are accumulated, causing image blurring or defocusing. To be confident of this conclusion, we simulated the exposure effect by accumulating random shifts of the sunspot profile. The left and right panels in Fig. 3 show, respectively, two observed sunspot profiles and two sunspot profiles with an artificial exposure. The sunspot profile is unstable, causing an enhancement of power in the sunspot. We applied an artificial exposure to one observed sunspot profile and produced profile shifts by generating 100 random numbers in a limited randomly generated range and averaged them. The length of the simulated series was 512 profiles. Because of the randomness of the numbers in the summation, we obtained different profiles, both strongly smoothed ones and those similar to the original observed sunspot profile. The power profiles for all fluctuations of the observed series and the series with a simulated exposure are shown below in Fig. 3. In both cases, we see an enhancement of power at the sunspot center. A comparison of the observed sunspot profiles and the artificial-exposure profiles, as well as the fluctuation power profiles, indicates that the proposed mechanism accounts for the power

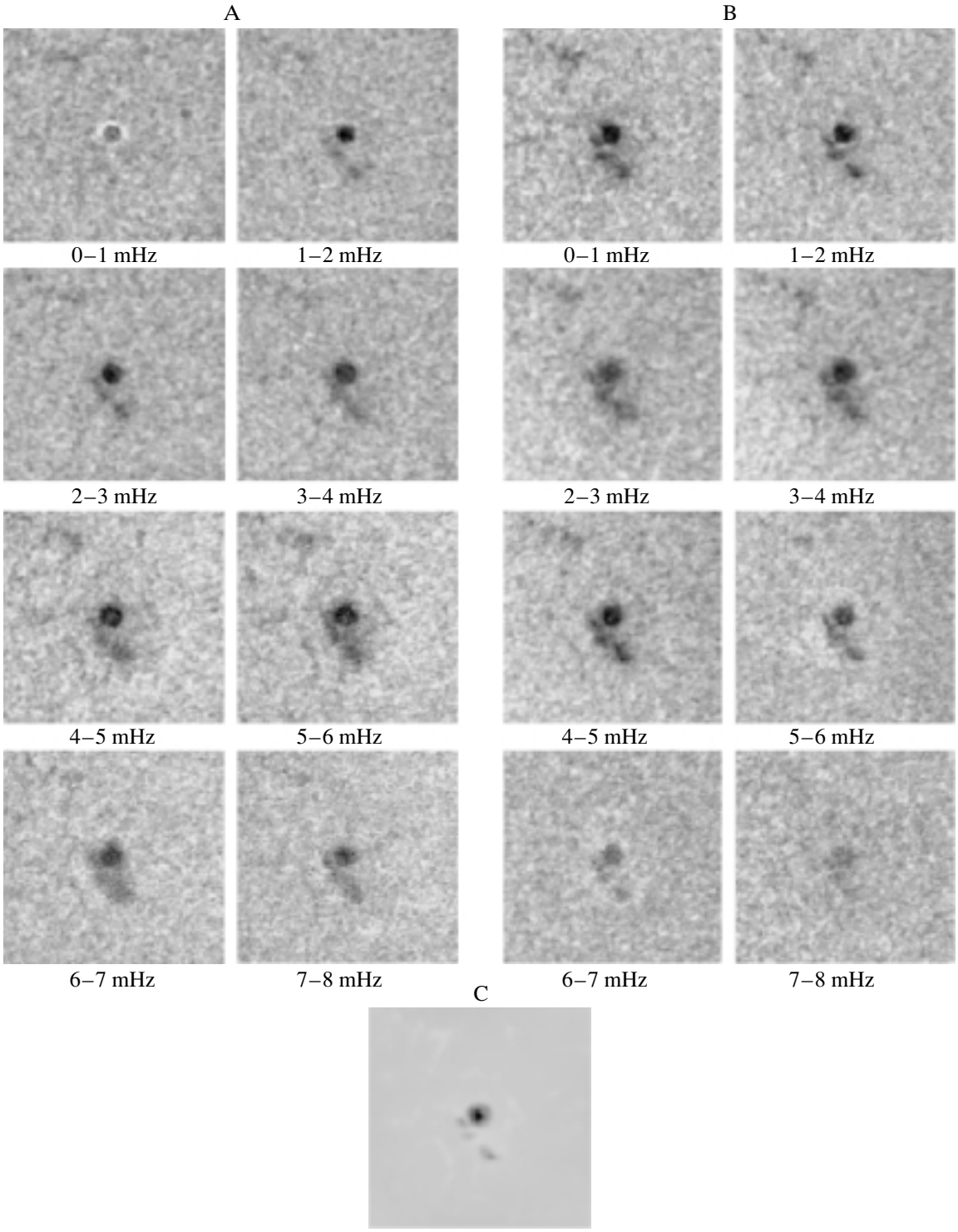

Fig. 1. MDI power maps: A— from intensity observations, B—from Doppler-shift observations; and C—an average intensity image.

enhancement at the sunspot center for data with a long exposure and unstable seeing.

Although we can isolate the acoustic signal at the sunspot center, the HLH acoustic power maps allowed us to study the power distribution outside the sunspot, which also arouses great interest. A power deficit is observed around the sunspot in the frequency range 3–6 mHz, which does not always correspond to the locations of the facular plages seen on the average image. A decrease in power due to faculae is

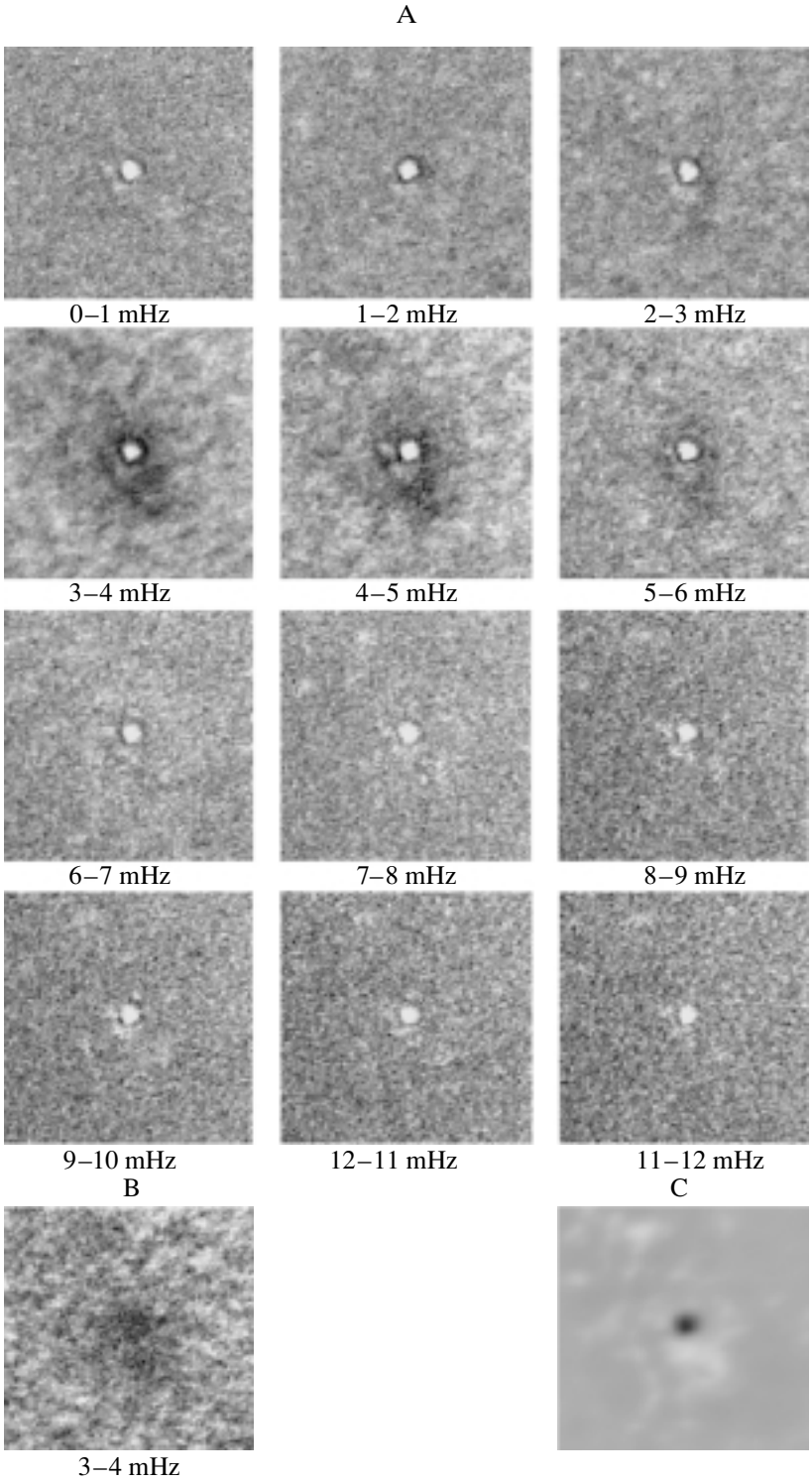

Fig. 2. A—HLH power maps; B—an acoustic power map for a short series with good seeing; C—an average image of the corresponding area.

illustrated by the bright plage in its upper left corner. A modest enhancement of power around the sunspot, the so-called halo, which surrounds the spot almost uniformly, can be seen in the frequency range 6–8 mHz. Clearly, this effect did not result from the change in the facular plages due to seeing, because the halo does not always directly coincide spatially with the locations of faculae. In contrast to the facu-

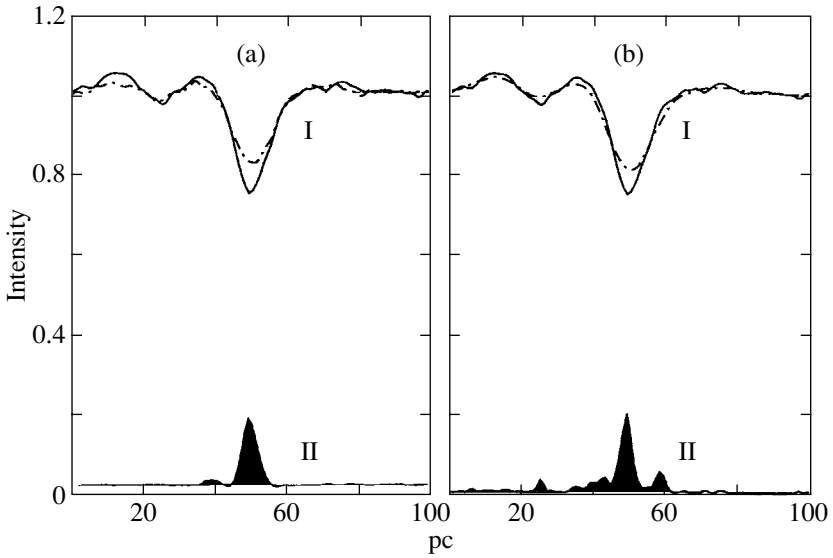

Fig. 3. I—Examples of various sunspot profiles for (a) the HLH data and (b) the simulated-exposure data. II—the total power for the observed (a) and simulated (b) series.

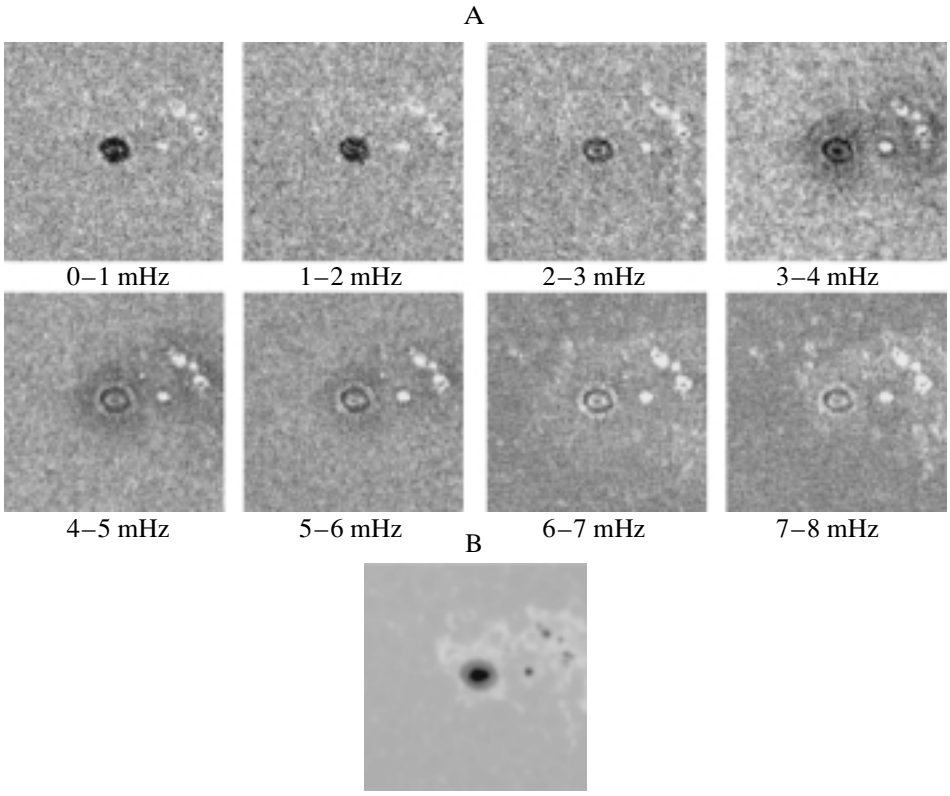

Fig. 4. TON power maps (A); (B)—the average image.

lae, it is located more or less uniformly. The frequency range of the power spectrum above 8.3 mHz and below the Nyquist frequency of 11.9 mHz is poorly studied in this spectral line. In this range, it was found that the spatial fluctuation scale decreases with increasing frequency, while the seeing effect shows up most clearly.

Another set of acoustic power maps was obtained for the short TON data series in the same spectral line as the HLH data. Figure 4 shows acoustic maps

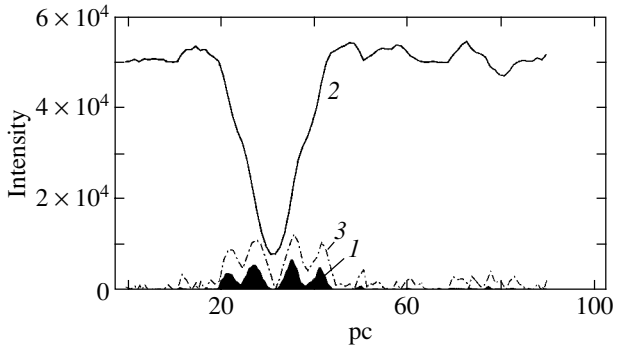

Fig. 5. The power (*1*) attributable to the combination of a high intensity gradient in the observed sunspot profile in the TON data (*2*) and the simulated seeing; (*3*) the intensity gradient profile.

in the frequency range 0–8 mHz and the average TON image (below). A preliminary mapping revealed a strong noisiness due to seeing, which we were able to considerably reduce by centering on the sunspot. However, this method proved to be acceptable only for the sunspot on which the centering was performed. Because of the short exposure (0.8 s), the inferred seeing in the sunspot region did not correspond to this parameter for more distant points of the area, which led to an enhancement of power at locations with a large gradient at the edges of the leading sunspot and neighboring spots. Nevertheless, such characteristic features as the reduction in power near the sunspot in the range 4–6 mHz and the power enhancement in the range 6–7 mHz clearly show up, which is in agreement with the results obtained by analyzing the HLH data.

The effect of seeing in combination with a high intensity gradient can be illustrated by using the observed sunspot profile obtained from the TON image and by simulating the seeing using random shifts in the position of the entire profile within a specified standard deviation relative to the initial profile position. Figure 5 shows the observed sunspot profile in an arbitrary direction. To simulate the observational time series, we performed the preceding step several hundred times with independent spatial shifts. The standard deviation relative to the initial profile position was taken to be 0.3 pixel. The total spectral power for the time series obtained at each spatial position of our model is shown in the figure below the sunspot profile. As we see from the figure, the sunspot profile has a central minimum with a high intensity gradient on both sides corresponding to the umbra and a flatter minimum corresponding to the penumbra. Both zones of high intensity gradients within the sunspot give rise to an excess in total power. Also shown in the figure is the intensity gradient profile that directly corresponds to the power profile.

CONCLUSIONS

In contrast to the power maps that were usually constructed for full-disk images, whose spatial resolution is too low to adequately investigate the structure of the power distribution in active regions, we have concretized the problem by considering high-spatial-resolution data in various spectral lines using data from several projects. Based on our studies, we can infer general properties that manifest themselves to one degree or another in different data:

(1) The suppression of acoustic energy in sunspots and, to a lesser degree, in facular plages. This effect shows up at all frequencies. However, the influence of atmospheric seeing on ground-based intensity data gives rise to an excess power attributable to nonsolar effects.

(2) A power deficit in the regions surrounding sunspots, which extends far beyond the sunspots themselves and their surrounding facular plages, can be interpreted as the shielding of the acoustically more active surface by faculae or as absorption of the modes passing through the sunspot. This effect is barely noticeable for the MDI data, showing up only slightly in a blurring of the region surrounding the sunspot.

(3) A modest excess in power compared to the field surrounding sunspots in the frequency range 5–7 mHz for the MDI Doppler-shift data and in the frequency range 6–8 mHz for the HLH and TON data. The halo is more pronounced in the Ca II K line for the HLH and TON data, suggesting a height dependence of this phenomenon, because the Ca II K line forms above the Ni I line. This phenomenon can be explained as follows: the oscillation modes interact with magnetic field lines at the photospheric level, perturb their oscillation, which propagates along field lines while increasing its amplitude as the pressure and density decrease with height, which generates oscillations at the chromospheric level during the interaction with the ambient medium.

Analysis of the seeing effect on our results reveals a significant power excess in the acoustic maps, which is difficult to separate from the actual acoustic power of solar oscillations. Nevertheless, as the short series of HLH observations with insignificant seeing shows, ground-based observations allow this effect to be eliminated when the data are of high quality (Fig. 2, pos. B). Our results indicate that a long exposure time (e.g., 42 s for the HLH data) leads to an averaging of the seeing for all pixels of the area and, hence, to a smoothing of the spatial fluctuations or defocusing. In this case, the sunspot profile undergoes the largest changes because of the high intensity gradient in the spot, changing from one image to another. The latter gives rise to an excess power at the sunspot center.

In contrast, for the TON data with a short exposure (0.8 s), the behavior of the atmospheric seeing projected onto each pixel is independent of the behavior for other pixels, which makes it difficult to remove its effect for all spatial array pixels. The effect of seeing on helioseismic data has already been investigated, but it cannot yet be eliminated. The power attributable to atmospheric seeing effects cannot be removed from the three-dimensional power spectrum of acoustic solar oscillations, because this effect is not localized in the spectrum but is smeared over the entire spectrum.

Despite some drawbacks, this method is widely used to investigate the observed power of the solar oscillations near sunspots, where the intensity gradient is small and where interesting phenomena, such as a halo, were found. The existence of a halo was also confirmed by other methods of analyzing seeing-free solar oscillations, for example, by the acoustic imaging technique (Chou *et al.* 2000). In the latter technique, the time series of oscillations after the passage of the wave packets in the solar interior and their return to the surface are reconstructed. Studies of the oscillation power inside active regions by acoustic power mapping are of greater interest in spaceborne experiments and in ground-based Doppler-shift observations, while intensity data should be selected more carefully with regard to atmospheric seeing.

ACKNOWLEDGMENTS

This study was supported by the REU (Research Experiences for Undergraduates) Program for 1999 carried out in Tucson and financed by the National Science Foundation of the USA (NSF). The work was supported in part by the INTAS grant no. 97-31198. We wish to thank the participants of the TON project for the data.

REFERENCES

1. D. C. Braun, T. L. Jr. Duvall, and B. J. Labonte, Astrophys. J. Lett. **319**, L27 (1987).
2. D. C. Braun, C. Lindsey, Y. Fan, and S. M. Jefferies, Astrophys. J. **392**, 739 (1992).
3. T. M. Brown, T. J. Bogdan, B. W. Lites, and J. H. Thomas, Astrophys. J. Lett. **394**, L65 (1992).
4. D.-Y. Chou, M.-T. Sun, and H.-K. Chang, Astrophys. J. **532**, 622 (2000).
5. D.-Y. Chou, M.-T. Sun, T.-Y. Huang, *et al.*, Sol. Phys. **160**, 237 (1995).
6. Sh. Egamberdiev, O. Ladenkov, Sh. Kholikov, *et al.*, in *Proceedings of the X IRIS/TON Workshop, Parkent, Uzbekistan, 1998,* Ed. by Sh. Ehamberdiev, p. 66.
7. B. W. Hidman and T. M. Brown, Astrophys. J. **504**, 1029 (1998).
8. P. H. Scherrer, R. S. Bogart, R. I. Bush, *et al.*, Sol. Phys. **162**, 129 (1995).
9. S. G. Toner and B. J. LaBonte, Astrophys. J. **415**, 847 (1993).

Translated by V. Astakhov

Astronomy Letters, Vol. 28, No. 6, 2002, pp. 419–422. Translated from Pis'ma v Astronomicheskiĭ Zhurnal, Vol. 28, No. 6, 2002, pp. 477–480.

On the Hill Stability in the General Problem of Three Finite Bodies

L. G. Luk'yanov and G. I. Shirmin*

Sternberg Astronomical Institute, Universitetskiĭ pr. 13, Moscow, 119992 Russia

Received January 15, 2002

Abstract—We construct zero-kinetic-energy surfaces and determine the regions where motion is possible. We show that for bodies with finite sizes, there are bounded regions of space within which a three-body system never breaks up. The Hill stability criterion is established. © *2002 MAIK "Nauka/Interperiodica".*

Key words: *celestial mechanics, three-body problem, zero-velocity surface, zero kinetic energy surface, Hill stability*

The surface of zero kinetic energy in a three-body problem generalizes the concept of zero-relative-velocity surface in a restricted circular three-body problem introduced by Hill (1905). These surfaces are the boundaries of the regions where the motion of bodies is possible.

Previously (Luk'yanov and Shirmin 2001), we studied zero-kinetic-energy surfaces and the regions where motion is possible in the problem of three bodies that were assumed to be mass points. We showed that the regions where motion is possible in the space of three mutual distances have the shape of a tripod whose vertex lies at the coordinate origin and whose infinitely long legs touch the coordinate planes along their bisectors. The principal result of our previous study is that we proved the absence of finite regions where motion is possible in the problem of three point bodies. Thus, the system can always break up (i.e., one of the mass points can move to an infinite distance). It follows from this result that all motions of mass points in the classical three-body problem may be considered to be unstable according to Hill.

In this paper, we use the same method to investigate the surfaces of zero kinetic energy but for the problem of three absolutely rigid bodies in the shape of spheres with a spherical mass distribution.

We assume bodies M_1, M_2, and M_3 to be spheres of radii a_1, a_2, and a_3 and masses m_1, m_2, and m_3, respectively. The mass densities of the bodies may be constant or depend on distance to the center of the corresponding sphere, i.e., the bodies have a spherical density distribution. Such bodies are mutually attracted as mass points (Duboshin 1975).

*E-mail: pant@sai.msu.ru

Without loss of generality, we assume that the following inequalities hold:

$$m_1 \geq m_2 \geq m_3. \tag{1}$$

At equal or sufficiently close densities, more massive bodies have larger sizes:

$$a_1 \geq a_2 \geq a_3. \tag{2}$$

In this case, the mass-to-radius ratios for the bodies satisfy the inequalities

$$m_1/a_1 \geq m_2/a_2 \geq m_3/a_3. \tag{3}$$

However, if the densities of the bodies differ significantly, then inequalities (2) and (3) are not necessarily satisfied.

Denoting the distance between the centers of bodies M_i and M_j by r_{ij} $(i, j = 1, 2, 3; i \neq j)$, we introduce a rectangular coordinate system $Or_{12}r_{31}r_{23}$ with the x axis r_{12}, y axis r_{31}, and z axis r_{23}.

Any mechanical motion in the three-body problem is represented in the space of mutual distances $Or_{12}r_{31}r_{23}$ by some continuous curve located within the domain of allowed values. Therefore, it is legitimate to analyze the regions where motions are possible in the space of mutual distances.

The domain of allowed mutual distances is determined by the triangle inequalities and contact conditions

$$r_{12} + r_{23} \geq r_{31}, \quad r_{31} + r_{12} \geq r_{23},$$
$$r_{23} + r_{31} \geq r_{12}, \tag{4a}$$
$$r_{12} \geq a_1 + a_2, \quad r_{31} \geq a_3 + a_1,$$
$$r_{23} \geq a_2 + a_3. \tag{4b}$$

Domain (4) is the common part (intersection) of two infinite regular triangular pyramids. One pyramid P has its vertex at the coordinate origin O and its edges coincide with the bisectors of the coordinate

1063-7737/02/2806-0419$22.00

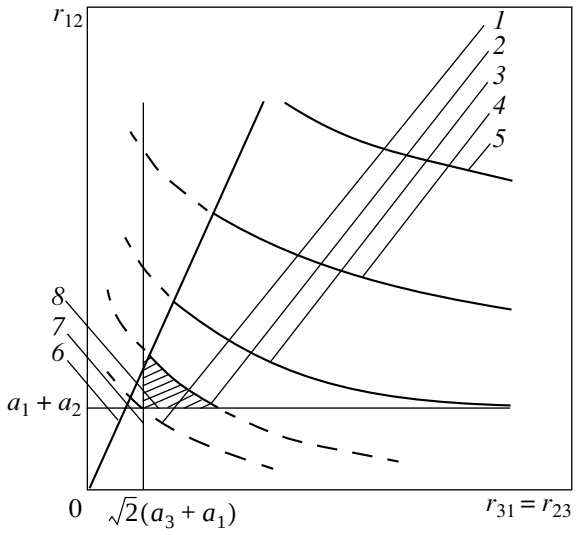

The section of the region where motion is possible by the $r_{31} = r_{23}$ plane. Curves (*1–5*) indicate hyperbolas (8) for: $C = C_{\max}$ (*1*), $C^{(3)} < C < C_{\max}$ (*2*), $C = C^{(3)}$ (*3*), $C < C^{(3)}$ (*4*), and $C \to 0$ (*5*). The intersection of the $r_{31} = r_{23}$ plane with the face $r_{12} = r_{31} + r_{23}$ of pyramid P (*6*), the face $r_{31} = a_3 + a_1$ of pyramid P' (*7*), and the face $r_{12} = a_1 + a_2$ of pyramid P' (*8*). The dashed lines indicate the parts of the hyperbolas that have no mechanical meaning. The section of the bounded region where motion is possible with stability according to Hill is hatched.

plane. The pyramid is defined by inequalities (4a). The second pyramid P' has its vertex at point $O'(a_1 + a_2,\ a_3 + a_1,\ a_2 + a_3)$ and this vertex is always located inside pyramid P. The edges are parallel to the coordinate axes. Pyramid P' is defined by inequalities (4b).

Thus, the domain of allowed values (4) defines in space $Or_{12}r_{31}r_{23}$ a body with six faces. The faces $r_{12} + r_{23} = r_{31},\ r_{31} + r_{12} = r_{23},\ r_{23} + r_{31} = r_{12}$ of pyramid P correspond to the arrangement of the bodies in the following order: M_1, M_2, M_3; M_3, M_1, M_2; M_2, M_3, M_1. On the faces $r_{12} = a_1 + a_2,\ r_{31} = a_3 + a_1,\ r_{23} = a_2 + a_3$ of pyramid P', there are pair contacts of bodies M_1 and M_2, M_3 and M_1, and M_2 and M_3, respectively. Point O' indicates a triple contact of the bodies.

The energy integral in the problem of three bodies with a spherical density distribution has the same form as for mass points:

$$T - U = h, \tag{5}$$

where T is the kinetic energy, U is the force function, and h is the energy constant.

The regions where motion is possible are determined by the inequality

$$U \geq -h, \tag{6}$$

where

$$U = f\left(\frac{m_1m_2}{r_{12}} + \frac{m_3m_1}{r_{31}} + \frac{m_2m_3}{r_{23}}\right),$$

and f is the universal gravitational constant.

Below, we restrict our analysis to $h < 0$. Only for negative energy constants does inequality (6) define a region where motions are possible that differs from the entire space. The boundary of this region is the surface of zero kinetic energy:

$$f\left(\frac{m_1m_2}{r_{12}} + \frac{m_3m_1}{r_{31}} + \frac{m_2m_3}{r_{23}}\right) = C, \tag{7}$$

where $C = -h,\quad 0 \leq C \leq C_{\max},\quad C_{\max} = C^{(1)} + C^{(2)} + C^{(3)},\quad C^{(1)} = fm_2m_3/(a_2 + a_3),\quad C^{(2)} = fm_3m_1/(a_3 + a_1),\quad C^{(3)} = fm_1m_2/(a_1 + a_2)$.

The regions where motion is possible for three finite-size bodies differ from similar regions for three mass points only by inequalities in (4b), where the collisions of the mass points were replaced with the contacts of the body spheres. Therefore, the previously obtained tripod (Luk'yanov and Shirmin 2001) with the vertex at the coordinate origin and with infinitely long legs along the edges of pyramid P should be corrected. According to inequalities (4b), the tripod is truncated by pyramid P'.

It is convenient to investigate the resulting region by using the sections by planes perpendicular to the coordinate planes and passing through the edges of pyramid P. Thus, the section by the $r_{31} = r_{23}$ plane has the form

$$fm_3(m_1 + m_2)r_{12} + fm_1m_2r_{31} = Cr_{31}r_{12}.$$

Using the transformation $r_{31} = r'_{31} + \alpha,\ r_{12} = r'_{12} + \beta$, where $\alpha = fm_3(m_1 + m_2)/C, \beta = fm_1m_2/C$, we can reduce this section to the form

$$r'_{31}r'_{12} = \alpha\beta. \tag{8}$$

Section (8) is a hyperbola with the asymptotes $r_{31} = \alpha,\ r_{12} = \beta$. The figure shows a family of hyperbolas (8) for various C. The other two similar sections can be derived from (8) by a circular permutation of the indices.

The regions where motion is possible can be obtained by cutting off part of the tripod legs adjacent to the edges of pyramid P by pyramid P'. Depending on C, the parts of the legs remained after the cutoff either can extend to infinity (in the figure, these are the hyperbolas for $C = C_4$ and $C = C_5$) or one, two, or three legs are completely cut off at a finite distance by the above planes ($C = C_2$ in the figure). For this reason, in contrast to point masses, for three finite-size bodies at sufficiently large C, the representing point lies within some finite region in the space of mutual distances and the three-body system does not

break up (hatched region). Let us consider this case in more detail.

If conditions (3) are satisfied, then $C^{(1)}$, $C^{(2)}$, and $C^{(3)}$ will satisfy the inequalities

$$C^{(3)} \geq C^{(2)} \geq C^{(1)}. \quad (9)$$

Then, as C decreases from $C_{\max}$ to zero, the regions where motion is possible will be modified as follows:

(1) At $C = C_{\max}$, there is a triple contact of the bodies, which may be considered as an equilibrium position. In the space of mutual distances, this is point O' that determines the entire region where motion is possible.

(2) Since all three legs of the tripod for $C^{(3)} < C < C_{\max}$ are completely cut off by pyramid P' at finite distances, the motion can take place inside the finite-size truncated tripod. The motion is restricted, because none the three bodies can move to a infinite distance. The three-body system never breaks up. For C close to $C_{\max}$, the region where motion is possible in the space of mutual distances has a small size and is adjacent to the vertex O' of pyramid P'. The section of this region by the $r_{23} = r_{31}$ plane is hatched in the figure. The size of this region increases with decreasing C, with the increase being most rapid toward the possible recession of body M_3. The maximum recession of body M_3 can be estimated from the intersection of hyperbola (8) with the face of pyramid P'. Simultaneously solving Eq. (8) with the equation of the straight line $r_{12} = a_1 + a_2$ yields the following estimate for the maximum recession of body M_3:

$$(r_{31})_{\max} \cong (r_{23})_{\max} \cong \frac{C^{(3)}}{C - C^{(3)}} \frac{fm_3(m_1 + m_2)}{C}.$$

The maximum recession of bodies M_2 and M_1 can also be estimated from this formula by a circular permutation of the indices.

(3) For $C^{(2)} < C \leq C^{(3)}$, the $r_{12} = a_1 + a_2$ plane does not completely cut off the leg that is closest to it but leaves an infinite slit through which body M_3 can move to an infinite distance. As a result, the three-body system breaks up into the receded body M_3 and the system of two bodies M_1 and M_2, which move relative to each other in elliptical orbits. For $r_{31} \to \infty$ and $r_{23} \to \infty$, relation (7) yields the region where motion is possible for the problem of two finite bodies M_1 and M_2. This region is confined between two concentric spheres in Euclidean space: $a_1 + a_2 \leq r_{12} \leq fm_1m_2/C$. Neither body M_1 nor body M_2 can recede to infinity, because the other two legs are completely cut off by pyramid P'.

(4) For $C^{(1)} < C \leq C^{(2)}$, only one tripod leg is completely cut off. Therefore, the system can also break up here. Either body M_3 or body M_2 can recede to infinity, but the binary system is always preserved.

(5) For $0 < C \leq C^{(1)}$, any of the three bodies can go to infinity. The remaining pair does not break up.

(6) For $C \leq 0$, the motion ceases to be elliptical and any of the bodies can leave the system. Moreover, the system can completely break up when all bodies fly apart to infinite distances.

The change of the zero-kinetic-energy surfaces and the regions where motion is possible will be different if the bodies have such densities and sizes that inequalities (3) are violated. However, all of the above results remain valid if we make an appropriate substitution of the indices. Thus, for

$$m_1/a_1 \geq m_3/a_3 \geq m_2/a_2, \quad (10)$$

inequalities (9) should be substituted with $C^{(2)} \geq C^{(3)} \geq C^{(1)}$ and all of the above results remain valid if we swap the indices 2 and 3. We can pass from inequalities (3) to inequalities (10), for example, by increasing the size of body M_2 (while keeping the sizes of the remaining bodies and the masses of all bodies unchanged) to values that satisfy inequalities (10). If conditions (10) are satisfied, then body M_2 is the first to get a chance of receding to infinity.

As C decreases, the body with the lowest m_i/a_i ratio rather than the body with the lowest mass or lowest density is always the first to get a chance of leaving the system. The last body to have such a chance is the body with the largest mass-to-radius ratio.

Degenerate cases are possible where one or both inequalities in (9) are transformed into equalities. If, for example, $C^{(3)} = C^{(2)} = C^{(1)} = C^{(0)}$, then the three-body system never breaks up at $C > C^{(0)}$ and any of the bodies can recede to infinity at $C \leq C^{(0)}$.

The most interesting and qualitatively new result is the existence of a finite region where motion is possible (see Section 2). It may therefore be asserted that, in contrast to the problem of three mass points, we have *stability according to Hill* in the problem of three finite bodies. For any densities and sizes of the bodies, the criterion for such stability is the satisfaction of the inequality

$$C > \sup\{C^{(3)}, C^{(2)}, C^{(1)}\}. \quad (11)$$

If condition (11) is satisfied, then the system of three finite bodies for $t \to \infty$ either exists eternally as a compact system or at some time t, one pair of bodies come into contact (collision) and the initial system ceases to exist.

For condition (11) to be satisfied, there must be at least one close pair characterized by some mutual

distance $r_{\min} = \inf\{r_{12}, r_{31}, r_{23}\}$. Assuming that inequalities (9) hold, we obtain the following from condition (11):

$$\frac{fm_1m_2}{r_{12}} + \frac{fm_3m_1}{r_{31}} + \frac{fm_2m_3}{r_{23}} > C^{(3)}. \qquad (12)$$

If we assume that $r_{12} = r_{31} = r_{23} = r_{\min}$ and take into account inequalities (1), then we derive an upper limit for $r_{\min}$ from (12): $r_{\min} < 3(a_1 + a_2)$.

Therefore, criterion (11) can be used only if there is a close approach of two (or all three) bodies to distances smaller than thrice the sum of the body radii. If, however, the distances between the bodies significantly exceed their sizes, then $C < \inf\{C^{(3)}, C^{(2)}, C^{(1)}\}$, and the regions where motion is possible do not differ qualitatively from similar regions in the problem of three mass points, for which there is no stability according to Hill.

Our results can be of considerable interest in studying the evolution of close stellar systems.

REFERENCES

1. G. N. Duboshin, *Celestial Mechanics: Basic Problems and Methods* (Nauka, Moscow, 1975).
2. G. W. Hill, Am. J. Math. **1**, 284 (1905).
3. L. G. Luk'yanov and G. I. Shirmin, Pis'ma Astron. Zh. **27**, 948 (2001) [Astron. Lett. **27**, 816 (2001)].

Translated by A. Dambis